UNIVERSITÀ DEGLI STUDI DI PADOVA

Laurea Magistrale in
ELECTRONIC ENGINEERING

Tesi di Laurea

Physics-Based Compact Model for p-GaN/AlGaN/GaN

Application: Understanding of Degradation after γ-Ray Irradiation

SUPERVISOR:
Matteo Meneghini

CO-SUPERVISOR:
Gaudenzio Meneghesso
Tian-Li Wu

AUTHOR:
Nicola Modolo

MATRICOLA:
1152960

ACADEMIC YEAR 2018/2019
8 JULY 2019

Physics-Based Compact Model for p-GaN/AlGaN/GaN HEMTs

Application: Understanding of Degradation After γ-Ray Irradiation

Abstract

Gallium Nitride (GaN)-based high electron mobility transistors (HEMTs) are rapidly emerging as front-runners in high-power mm-wave circuit applications. Despite the recent commercial success of GaN-based devices, internal physical mechanisms are often not completely understood. This thesis explores the nature of gallium nitride devices from the point of view of compact modeling paying particular attention to power electronic applications. To model the behaviour of such devices, the physics of the typical AlGaN/GaN Schottky HEMT is studied by solving the Schrödinger's and Poisson's equations in order to have a unified and accurate definition of the Fermi level and 2DEG charge.

The physical-based model is used to help our understanding of the effects of γ-irradiation on GaN-based devices. Thanks to this approach we demonstrate that we are able to point the leading factor in the induced degradation. Furthermore, we propose a novel approach to model the p-GaN/AlGaN/GaN structure by implementing the p-GaN layer in the developed AlGaN/GaN model. The simulation results are then compared with the experimental data obtained by four devices showing excellent agreement. Finally, inspired by the method used to include the p-GaN layer under the gate, and aware of the results that ferroelectric materials are showing in the rising NCFET technology, we studied the physics of such material following the phenomenological approach described by the Landau-Khalatnikov equations. The ferroelectric material is implemented in the AlGaN/GaN model. The simulations result is consistent with the studies conducted on the NCFET where the MFMIS structure shows higher ON-current, and transconductance.

Contents

Introduction **14**

1 Gallium Nitride **16**
1.1 HEMT working principle 16
1.2 GaN - Unique Material Properties 18
1.3 GaN - Impact 22

2 Modeling of D-Mode GaN HEMT **24**
2.1 GaN compact models: Overview 24
2.2 Core Model 26
2.2.1 Surface Potential 27
2.2.2 Intrinsic Charge 32
2.2.3 Drain Current 37
2.3 Real Device Effects 38
2.3.1 Mobility Degradation 39
2.3.2 Short Channel Effects 39
2.3.3 Access Region Resistance 40
2.4 Conclusion 42

3 Understanding of γ-Ray Degradation in Schottky HEMT **44**
3.1 Radiation Defects in GaN 44
3.1.1 Displacement Damage 44
3.2 γ-Ray Degradation in MIS-HEMT 48
3.2.1 Experiment Details 49
3.2.2 Experiment Results and Discussion 49
3.3 γ-Ray Degradation in Schottky HEMT 53
3.3.1 Device Fabrication and Experimental Results 53
3.3.2 Parameter Extraction Strategy 55
3.3.3 Understanding of γ-Ray Degradation using GaN Model 58
3.4 Conclusion 58

4 Modeling of E-Mode GaN HEMT **60**
4.1 Working Principle 60
4.2 Modeling the p-GaN HEMT 61
4.2.1 Voltage Drop in the p-GaN Layer 64
4.2.2 Fully Depleted p-GaN 68
4.3 Results 69
4.3.1 Gate Capacitance 70
4.3.2 Depletion Region 71

4.3.3 Vertical Potential Drop 75
4.3.4 I_D-V_G 76
4.4 Conclusion 77

5 Negative Capacitance in GaN HEMT 78
5.1 Concept and Reasons 78
5.2 Ferroelectric Dynamics 80
5.2.1 Landau-Khalatnikov Model 81
5.2.2 Temperature Dependence 85
5.3 Device Implementation 88
5.3.1 Modeling NC-GaN HEMT 88
5.4 Conclusion 93

Conclusion and Future Work 94

List of Figures

1 Basic Structure of a Field Effect Transistor. The physical principle behind the FET involves the use of a gate to alter the charge in a channel. 14

1.1 Band profile of a AlGaN/GaN HEMT showing band bending leading to a triangular quantum well at the AlGaN/GaN interface. 17

1.2 Direct vs indirect band gap recombination. In case of the direct recombination, the energy is released in the form of photons, while in case of indirect recombination it is released in the form of phonons (until the electron and hole have the same momentum) and eventually photons. 19

1.3 Bandgap diagram of III nitrides with overlaid visible light colors versus their corresponding lattice parameters. 20

1.4 Typical AlGaN/GaN heterostructure used in polar HFET technology, along with the charge distribution and the band diagram. 21

1.5 Expected impact in the market of GaN technology from the market research firm Yole Déveleppement. The power supply has been identified as the key application leading the economic growth of gallium nitride devices. 23

2.1 Cross Section of the AlGaN/GaN HEMT discussed in this chapter. Inside the red square there is the core module which delimits the intrinsic region and defines the surface potential $\psi_s(x)$, the intrinsic charge in each terminal Q_{gi},Q_{si},Q_{di} and the drain current I_D. 25

2.2 Matlab simulation of the gate vertical voltage drop, defined in equation 2.3, in an AlGaN/GaN structure with threshold $V_{TH} = -4$ V, where the AlGaN layer has 20% Aluminum and thickness $t_{AlGaN} = 16$ nm. 31

2.3 Matlab simulation of the charge density used to evaluate the vertical voltage drop of the AlGaN/GaN structure in figure 2.2. 32

2.4 Matlab simulation of the surface potential, in source (ψ_S) and drain (ψ_D) side, for different V_D in AlGaN/GaN structure with gate length $L = 5 \times 10^{-4}$ cm, threshold $V_{TH} = -4$ V, electron mobility $\mu_s = 1500$ cm$^2/Vs$, velocity saturation $v_S = 1 \times 10^7$ cm/s, where the AlGaN layer has 20% Aluminum and thickness $t_{AlGaN} = 16$ nm. 33

2.5 Simulation vs experimental data on a Schottky HEMT with a diameter of 120 nm, where the AlGaN layer has thickness 20 nm and 24% of Al. The Figure shows excellent agreement in the result, also for the first order derivative. The simulation is performed implementing the Verilog-A code in ADS. 37

2.6 The Figure shows the contribution of surface and AlGaN capacitance used to calculate the gate capacitance using equation 2.35. The experimental data comes from the same device of figure 2.5. The simulation is performed implementing the Verilog-A code in ADS. 38

2.7 Cross Section of the AlGaN/GaN HEMT from figure 2.1, highlighting the effect of the access region resistances in the calculation of the ON resistance. 40

2.8 I_D-V_G simulation vs experimental data of Schottky HEMT with threshold voltage V_{TH} −4.9 V, length gate length $L = 5$ μm and width $W = 10$ μm. The simulation is performed implementing the Verilog-A code in the electronic design automation software Advanced Design System (ADS) by Keysight EEsof EDA. 42

2.9 I_D-V_D simulation vs experimental data of Schottky HEMT with threshold voltage V_{TH} −4.9 V, length gate length $L = 5$ μm and width $W = 10$ μm. The simulation is performed implementing the Verilog-A code in ADS. 43

3.1 Empirical relationship between mean displacement energy E_d and inverse lattice parameter for various semiconductors [43]. GaN excels. 45

3.2 The relative importance of the three major types of γ-ray interaction. The lines show the value of Z (number of protons) and $h\nu$ (energy of the incident photons) for which the two neighboring effects are just equal [42]. 46

3.3 Three major types of γ-ray interaction with the incident atom. 47

3.4 Keysight B1500A semiconductor device analyzer used to perform the measurement. 48

3.5 Measured I_D-V_G in all four samples after various γ-ray doses. 50

3.6 Measured I_G-V_G in Sample 2, 3, and 4 after various γ-ray doses. . . . 51

3.7 Device pad SEM image after 5 kGy γ-irradiation, showing the creation of small cavities. In the figure is highlighted with a yellow circle the inner cavity and orange the periphery. The table contains the atomic percentage of the elements characterized by EDAX analysis. . 52

3.8 Elemental distribution showing the formation of Aluminum oxide. (a) Shows the distribution of aluminum. The concentration decreases significantly in the periphery of the cavity. (b) Shows the distribution of Oxygen. The concentration is higher in the periphery of the cavity confirming the formation of AlO_x 52

3.9 Measured I_D-V_G characteristic subjected to cumulative γ-ray radiations. 54

3.10 Input output parameters in used to calibrate the model with the pristine case and with the experimental data coming from the Hall measurement and C-TLM. The saturation velocity under the gate region (v_S) and access region ($v_{S,acc}$) are supposed to be identical and equal to 1.05×10^7 cm/s. The same assumption is made for the mobility which is always the same along channel and access region and equal to the value determined experimentally by Hall measurement. 55

3.11 Step by step DC parameter extraction strategy tuning the simulation performed using ADS with the measured I_D-V_G and I_D-V_D. In the figures is shown how to extract the main parameters starting from threshold voltage identification from I_D-V_G. 56

3.12 I_D-V_G and I_D-V_D before radiation (pristine case) and for each radiation dose. The simulation shows excellent agreement with the experimental data. The GaN model can follow the change in the mobility and contact resistance due to the cumulative γ-irradiation. For this reason the GaN model can give us an insight of the contribution of each parameters in the increase of the drain current. 57

3.13 Fitted I_D-V_G and I_D-V_D characteristics tuning only the mobility and the contact resistance to identify which one is the leading factor in the origin of the instability. 58

4.1 p-GaN/AlGaN/GaN HEMT structure discussed in this chapter where the p-GaN material is deposited under the gate of a Schottky HEMT device. 61

4.2 (a) Detailed cross section of the p-GaN/AlGaN/GaN structure with relative voltages along with the simulated energy-band diagram at (b) zero bias and (c) V_G = 6 V. 62

4.3 Qualitative representation of the charge distribution when a positive bias is applied in the p-GaN/AlGaN/GaN structure. Regarding the PiN junction the 2DEG channel can be considered equivalent to an highly doped n-type semiconductor. 64

4.4 Modeling flow-chart used to simulate the p-GaN/AlGaN/GaN structure next to its equivalent circuit 69

4.5 Measured and simulated C-V characteristic. The simulation shows excellent agreement with the experimental data for all the samples. In case of Samples A, B, and C, with the increase of the gate voltage it follows the decrease of the capacitance due to the increase of the depletion region thickness, while in case of Sample D which has a fully depleted p-GaN it remains constant. 70

4.6 Contribution of each capacitance in the p-GaN/AlGaN/GaN structure for the calculation of the total capacitance C_G of Sample A. For $V_G > V_{TH}$, when the 2DEG is formed, the surface capacitance C_s becomes big enough to be considered negligible in the calculation of the total capacitance C_G. 71

4.7 Detail of the effect of the Schottky and the PiN junction lowering the total capacitance when the gate voltage increases for Samples A, B, and C. In case of Sample D the device is fully depleted so since the voltage drop is defined by the interpolation of equations 4.21 and 4.22, it becomes hard to distinguish the single effect of the Schottky junction and the PiN junction. For this reason only their total contribution is plotted. 72
4.8 Simulation result of Sample D setting the maximum extension of the depletion region equal to the thickness of the p-GaN layer and without taking into account the maximum extension of the depletion region. . 73
4.9 Depletion region in Sample A, B, and C next to the corresponding Electric field in the Schottky junction. 74
4.10 Qualitative representation of the charge distribution in the two series capacitance. To keep the charge balanced, the p-layer cannot be completely depleted. 74
4.11 Vertical voltage drop in the channel vs voltage drop in the p-GaN and AlGaN layers. The simulation is calibrated with the extracted parameters of Sample A. 75
4.12 Measured and simulated I_D-V_G characteristic. The simulation shows good agreement with the experimental data for all the samples. . . . 76

5.1 (a) Equivalent circuit for the division of the gate voltage between the insulator capacitance and the semiconductor capacitance in a standard FET structure. (b) Block diagram of a special capacitance with positive feedback to introduce the concept of negative capacitance. . . 79
5.2 Classification of ferroelectric within the group of (crystalline) dielectrics. Ferroelectric are a subgroup of pyroelectric, which themselves are a subgroup of piezoeletric. 80
5.3 Typical ferroelectric hysteresis loop in Metal-Ferroelectric-Metal (MFM) structure. Left: instantaneous distribution of charge in the electrodes (grey) and in the ferroelectric during polarization reversal. White and black arrows indicate the polarization direction and the direction of the electric field respectively. Right: correlation between these charge distributions and different point of the hysteresis loop in the polarization vs voltage (P-V) characteristic. 81
5.4 Calculated polarization dependence of free energy. If $\alpha_0 > 0$, the lowest free energy state is for zero polarization. If $\alpha_0 < 0$, there are two non-zero lowest free energy states that corresponds to the coercive polarization $\pm P_C$. 82
5.5 Polarization as a function of the electric field. If $\alpha_0 > 0$ the capacitance is always positive. The negative slopes of the S curve when $\alpha_0 < 0$ results in a negative capacitance. The scheme A-B-C-D represent the unstable hysteresis-free path. The conventionally observed includes in the scheme A-B-D-C, which includes the hysteresis. 83
5.6 dP/dt as a function of the polarization. The system is stable when $P = \pm P_R$ and unstable if $P = 0$. From figure 5.5 is possible to see that the instability occur when the ferroelectric is in the negative capacitance condition. 84

5.7 Polarization as a function of the electric field in a first-order transition with $P_R = 35\ \mu$C/cm^2, $P_C = 36\ \mu$C/cm^2, $\mathscr{E}_C = 1$ MV/cm compared with the relative second-order transition. The hysteresis loop is almost the same so they cannot be distinguished easily from the experimental data. 85
5.8 First-order phase transition with varying temperature. 86
5.9 Cross-section of the MFMIS structure discussed in this chapter where the ferroelectric material is deposited under the gate of a Schottky HEMT device. 88
5.10 Modeling flow-chart implemented in Verilog-A and used to simulate the NC-GaN HEMT. The GaN model is based on the experimental data of the non-irradiated Schottky HEMT studied in Chapter 3. 89
5.11 Impact of variation of the ferroelectric thickness on the voltage amplification of the internal node. 91
5.12 Impact of variation of the ferroelectric thickness on the DC performance of GaN HEMT. All the DC performances are significantly increased. In order are plotted: (a) I_D-V_G linear scale, (b) I_D-V_G log scale, (c) transconductance, (d) gate capacitance, (e) I_D-V_D and (f) drain conductance. 92
5.13 Impact of the variation of the temperature in the DC performance of NC-GaN HEMT. 93

List of Tables

1.1 Material properties related to the power performances at high frequencies for various materials. 17

2.1 Quantities to increase the Fermi level accuracy using Householder method 32

3.1 γ-ray dose regime for 4 identical samples. Note that each sample consists of 5 devices. 49
3.2 Comparison of I_D at V_G = 0 V and V_D = 20 V after each γ-ray dose. . . 50
3.3 Carrier concentration and mobility from Hall Measurement, contact resistance and sheet resistance from C-TLM 54
3.4 Output parameters based on the fitted curve in the fresh device. . . . 57

4.1 Summary of the important device parameters of Samples A,B,C, and D. 70
4.2 Summary of the extracted parameters for Samples A,B,C, and D. . . . 73
4.3 Summary of the extracted parameters for Samples A,B,C, and D. . . . 76

Introduction

Part of the semiconductor industry's formula for success is to make incremental changes, not drastic changes. The planar Metal-Oxide-Semiconductor Field-Effect Transistor (MOSFET) has served the electronic industry well for 40 years. Aggressive engineering has managed to reduce its size again and again without change to its basic structure [1]. The basic concept behind the Field-Effect Transistor (FET) is quite simple as illustrated in figure 1.

The device consist of an active channel through which electron (or holes) flow from the source to the drain. The source and drain contact are ohmic contacts. The conductivity of the channel is modulated by a potential applied to the gate. This results in the modulation of the channel so that no current flows into the gate. The gate isolation is done in a variety of ways, leading to a number of different devices. In the previously introduced MOSFET, the gate is isolated from the channel by an oxide. This is the basis of the silicon devices.

Another approach is the one purse in the Metal-Semiconducotr FET (MESFET) where the gate forms a Schottky barrier with the semiconductor keeping a small gate current in the useful range of gate voltages. Finally Heterojunction Field-Effect Transistor (HFETs) or Modulation-Doped FETs (MODFET) use a large bandgap semiconductor to isolate the gate from the active channel [2].

An emerging class of materials that has became primary choice for blue LEDs, blue LASER diodes and other optoelectronic devices is the (Al,Ga,In)N-based systems. These materials are fundamentally different from conventional cubic semiconductors in that they exist normally in the hexagonal (wurtzite) phase and exhibit strong polarization in the $< 0001 >$ direction [2].

The troubled history and the recent success of nitride semiconductor devices are both very much related to the unique material properties of GaN and its most

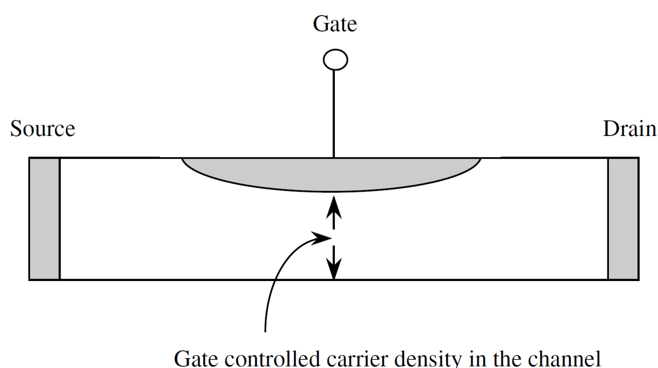

Figure 1: Basic Structure of a Field Effect Transistor. The physical principle behind the FET involves the use of a gate to alter the charge in a channel.

relevant alloys InGaN and AlGaN [3]. Depending on the alloy composition, the direct bandgap (the difference between conductance and valence energy in the material band diagram) varies from about 0.7 eV to 6.2 eV, covering a wide wavelength range from red through yellow and green to blue and ultraviolet. This leads to unique material properties, such as high break down voltage, high charge density, high thermal conductivity and high electron mobility.

Despite the recent commercial success of GaN-based devices, internal physical mechanisms are often not completely understood. Sophisticated theories and physic-based compact models have been developed for previous generations of semiconductor devices [3]. However, the unique properties of nitrides present a challenge. The aim of this study is to present a physic-based analytical model for AlGaN/GaN HEMT which is derived from consistent solution of Schrödinger's and Poisson's equations. In the following, the structure of the Thesis will be introduced through a series of capsule descriptions of the chapters.

Chapter 2: **Gallium Nitride**. This chapter gives a brief overview of the High Electron Mobility Transistor (HEMT) working principle. A particular attention will be paid on a specific material: the Gallium Nitride and its unique properties.

Chapter 3: **Modeling of D-Mode GaN HEMT.** Surface potential calculation, intrinsic charge calculation, drain current model, mobility degradation, drain induced barrier lowering, access region and parasitic resistance and finally parameter extraction strategy; in brief, the core model and the real physical effect that define the physic-based AlGaN/GaN compact model will be analytically described in this chapter.

Chapter 4: **Understanding of γ-Ray Degradation in Schottky HEMT.** In this chapter the concept of degradation in natural space radiation environment will be introduced. The described compact model will be than used to understand γ-ray degradation in AlGaN/GaN HEMTs identifying the main factor leading to the induced degradation.

Chapter 5: **Modeling of E-Mode GaN HEMT.** The concept and the working principle of normally-off HEMT will be presented giving particular attention to pGaN/AlGaN/GaN structure. The compact model will be then used to understand the effect of the pGaN layer under the gate in the measured gate capacitance.

Chapter 6: **Negative Capacitance in GaN HEMT.** In this chapter the concept of ferroelectricity will be introduced starting from the Landau-Khalatnikov description of Ferroelectric dynamics. After that a single domain crystal will be implemented under the gate of the GaN model to show how the DC performances can increase.

Chapter 7: **Conclusion.** Finally, summary of the obtained results and conclusions are presented. Further work that is needed in this area is also discussed.

Chapter 1

Gallium Nitride

1.1 HEMT working principle

In the MESFET the gate is insulated from the channel by a barrier created by either a Schottky barrier (or a p^+n junction). The charge in the channel is provided by dopants in the channel. The dopants, while providing charge, also cause increase of impurities and reduced mobility. Thus, a question arises: is it possible to have channel charge but avoid dopant scattering? This is possible in the Si MOSFET where the charge can be induced by inversion. However, the MOSFET charge has to contend with interface roughness scattering [4].

In advanced semiconductor devices, junctions between two different semiconductor materials can be formed to improve device performances. A *compound semiconductor* is obtained combining multiple chemical elements to constitute a crystal with the properties of a semiconductor. Creating compound semiconductors allow an increase in the degrees of freedom on the fundamental properties of the semiconductor such as the energy gap (E_g) or the crystal lattice constant (Å). Most compound semiconductors are from combinations of elements from Group III and Group V. A semiconductor deposited on another one with different composition through epitaxial growth is considered an *heterostructure*. The interface between two different layers is called *heterojunction* [5]. The most widely used heterostructure FET is the High Electron Mobility Transistor (HEMT). A typical modulation doped device structure is shown in figure 1.1.

The basic working principle of HEMT is given by the difference in bandgap (E_g) and electron affinity (X) between the AlGaN and the GaN layers. This difference create a conductance (and valence) band discontinuity that produce a quantum well in which the electrons are confined. The quantum well has a triangular form and the electrons are confined with high density in a very narrow region that have 2-dimensional properties. The term 2-Dimensional Electron Gas (2DEG) is used to describe the electron system [2]. It's important to note that the electrons confined in the quantum-well are located in the i-GaN that is not doped and consequently is almost free from impurities. The charge density in the channel n_s [cm^{-2}] is determined by the energy levels of the electrons and is described by the Schrödinger wave function. Many of the first generation HEMT devices belong to the AlGaAs/GaAs or InAlAs/InGaAs family [5].

Today, with the upsurge of wireless communication market, as well as the steady but continuous progress of traditional military applications, microwave transistors

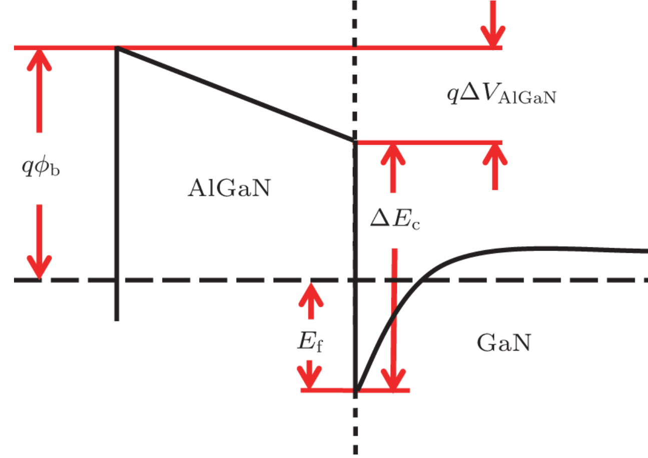

Figure 1.1: Band profile of a AlGaN/GaN HEMT showing band bending leading to a triangular quantum well at the AlGaN/GaN interface.

are playing a critical role in many aspects of human activities. The requirements for the performance of microwave transistor are becoming more and more demanding. Because of these needs, there has been a significant investment in the development of high performance transistors and amplifiers based on Si/SiGe, GaAs, SiC and GaN [6]. Table 1.1 lists the major parameters of these materials while the Johnson's figure of Merit (JM) is used to calculate and compare their power-frequency limits. The JM gives the power-frequency limit based solely on material properties and can be used to compare different materials for high frequency and high power applications [7].

The requirement for high power and high frequency is highly related to semiconductor material with both large breakdown voltage and high electron velocity. From this point of view, wide band gap materials, like GaN and SiC, with higher JM are preferable. Whether it be GaN or SiC, each has its own merits and obstacles to wide spread adoption. The wide band-gap result in higher breakdown voltages because the ultimate breakdown field is the field required for band-to-band impact ionization [6]. Moreover, both have high electron saturation velocities, which allow high frequency operation. The ability of GaN to form heterojunctions makes it su-

	Unit	Si	GaAs	4H-SiC	GaN	Diamond
E_g	[eV]	1.1	1.42	3.26	3.39	5.45
μ_n	[cm^2/Vs]	1350	8500	700	1500-2000	1900
v_{sat}	[10^7cm/s]	1.0	1.0	2.0	2.5	2.7
E_{BR}	[MV/cm]	0.3	0.4	3.0	3.3	5.6
ε_r	-	11.8	13.1	10.0	9.0	5.5
$JM = E_{BR} v_{sat}/2\pi$		1	2.7	20	27.5	50

Table 1.1: Material properties related to the power performances at high frequencies for various materials.

perior compared to SiC, in spite of having similar breakdown fields and saturation velocities. GaN can be used to fabricate HEMTs whereas SiC can only be used to fabricate MESFETs. The advantages of HEMT include high carrier concentration that combined with the high electron mobility results in a high current density and low channel resistance, which are especially important for high frequency operation and power switching applications [8]. From the amplifier point of view, GaN-based HEMT have many advantages over existing production technologies (e.g. GaAs) [6]. The high output power density allows the fabrication of much smaller size devices with the same output power. Higher impedance due to the smaller size allows for easier and lower loss matching in amplifier. The operation at high voltage due to its high breakdown electric field not only reduces the need for voltage conversion, but also provides the potential to obtain high efficiency, which is a critical parameter for amplifiers. The wide band-gap also enables it to operate at high temperatures. At the same time, the HEMT offer better noise performances than that of MESFET's [8]. These attractive features in amplifier applications enabled by superior semiconductor properties make the GaN-based HEMT a very promising candidate for microwave power applications [6]. In the next section, the main reasons that make Gallium Nitride a unique compound semiconductor will be discussed.

1.2 GaN - Unique Material Properties

The first Gallium Nitride (GaN) material has been produced by passing ammonia over hot gallium by Jusa and Hahn in 1939. However, to realize its true potential, it is necessary to wait until 1991 when Nakamura developed a suitable Metal-Organic Chemical Vapor Deposition (MOCVD) equipment for GaN [9]. By combining the buffer-layer technology developed by Akasaki and Amano [10] and Nakamura [9] with the idea of double heterostructure, the first bright blue Light-Emitting Diode (LED) was demonstrated using InGaN [11]. For their important contributions the researchers Akasaki, Amano and Nakamura were awarded the Nobel Prize in Physics in 2014 for "*the invention of efficient blue light-emitting diodes which has enabled bright and energy-saving white light sources*".

While enabling the white LED has been the most significant contribution GaN has made to society to date, due to significant energy saving compared to other white light sources [12], numerous other applications exist or are being developed. To understand the main reasons that make III-V nitrides an almost ideal class of material, is important to have an insight of its properties.

Energy gaps (E_g) for nitride semiconductors and their alloys span the wide range from 0.7 to 6.2 eV. In optical terms is important to take into account that there are two types of semiconductors: *direct band gap* (such as InAs, GaAs) and *indirect band gap* (such as Si, Ge). GaN is a direct band gap material.

To understand why this is a key material property, the concept of radiative recombination has to be introduced. Interactions among electrons, holes, photons, phonons and other particles are required to satisfy conservation of energy and crystal momentum. An important process that describe these interactions is called radiative recombination, where an electron in the conduction band annihilates a hole in the valence band, with the same momentum, releasing the excess energy as photon. As illustrated in figure 1.2, this is possible in a direct band gap semiconductor where, for the conservation of the energy, the energy of the emitted photon will be

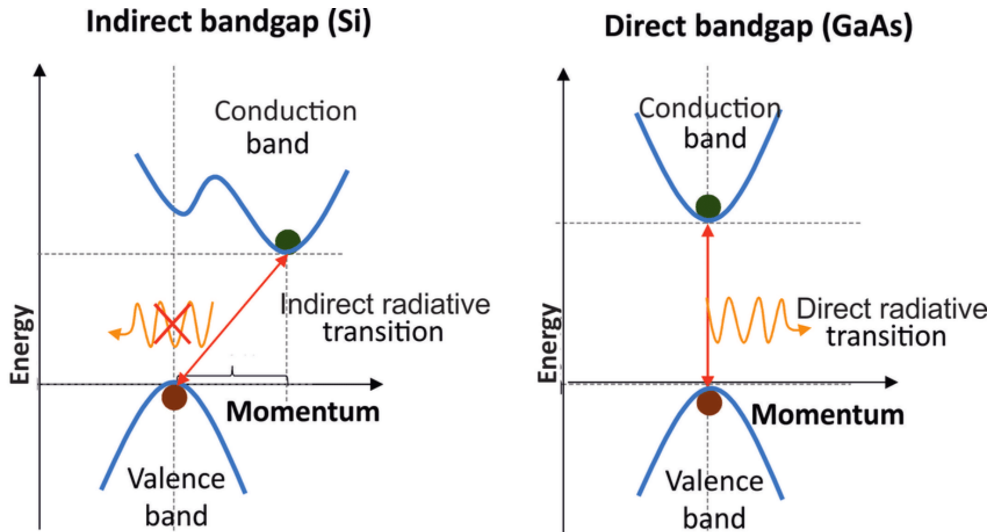

Figure 1.2: Direct vs indirect band gap recombination. In case of the direct recombination, the energy is released in the form of photons, while in case of indirect recombination it is released in the form of phonons (until the electron and hole have the same momentum) and eventually photons.

equal to the energy lost by the electron to recombine with the hole.

For an indirect band gap material, the process must also involve the absorption or emission of energy in form of crystal lattice vibration (phonons) until electron and hole have the same momentum [13]. The involvement of the phonon makes this process less likely to occur in a given span of time, which is why radiative recombination is far slower in indirect band gap material than direct band gap ones. Optoelectronic is the transformation of a bias current (electrons) in emitting light (emission of photons) with high efficiency. That's why LEDs and LASERs use direct band gap materials. Equation 1.1, where h is the Planck constant, shows that the frequency of the emitted photon v is proportional to its energy.

$$E_g \simeq E_{ph} = hv \tag{1.1}$$

Since, as mentioned above, in nitride semiconductors and their alloys the energy gap ranges from 0.7 to 6.2 eV, this means that using the appropriate combination, it is possible to span the entire ultraviolet (UV) visible light spectrum (figure 1.3).

Spontaneous polarization is an other unique material property that is absent in other well-known semiconductors used in optoelectronic devices such as GaAs and ZnSe but that is shown by this class of materials. This property has great importance in applications because is part of the technological development of electronic devices like AlGaN/GaN High Electron-Mobility Transistors (HEMTs) [3]. In nature there exist two class of materials carring the polarization charge: the *ferroelectrics* and the *pyroelectrics*. In the ferroelectrics (whose principle will be introduced in Chapter 5 with the concept of negative capacitance), the polarization charge can be inverted by applying a suitably strong electric field. In pyroelectrics, the polarization charge cannot be directly measured because its direction and orientation cannot be altered and is always parallel to the *pyroelectric axis*. Luckily, just after GaN became a target of technological applications, a big step forward in the theory of solids, called Modern Theory of Polarization (MTP) [14], provided

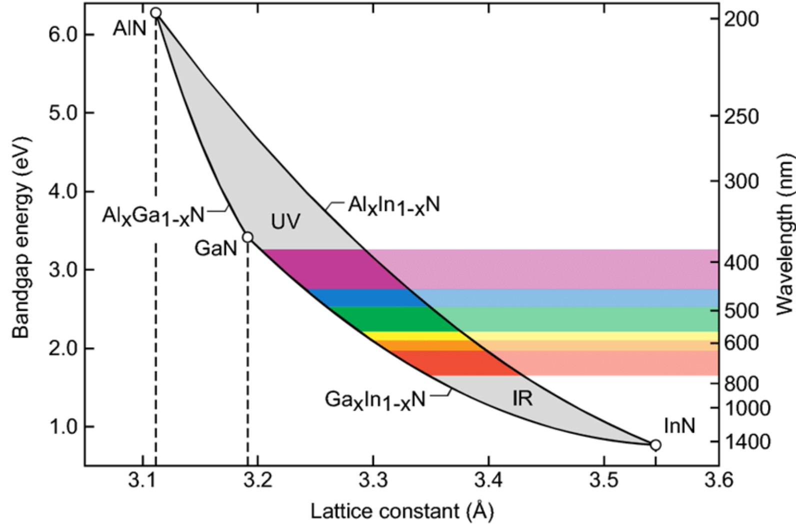

Figure 1.3: Bandgap diagram of III nitrides with overlaid visible light colors versus their corresponding lattice parameters.

an easy and accurate way to compute the polarization charge using first-principles computational tools. Understanding the effects that these polarization fields have on the electric property of the material is important for a proper comprehension of the physics of AlGaN/GaN HEMTs. Using a less rigorous but more intuitive approach, the presence of *spontaneous polarization* charge (Q_{SP}) in the junction can be explained by the intrinsic asymmetry of the bonding in the equilibrium wurtzite crystal structure. In addition, mechanical stress also results in polarization, which is then called *piezoelectric polarization*, where Q_{PZ} is the corresponding charge. The piezoelectric polarization is negative for tensile and positive for compressive strained AlGaN layers. Therefore, the orientation of the spontaneous and piezoelectric polarization is parallel in case of tensile strain and antiparallel in case of compressive strain. Unstrained GaN has a lattice constant $a_{GaN} = 3.189$ Åwhile for AlN it is $a_{Al} = 3.11$ Å[5]. AlGaN lattice constant can be calculated from the Vegard's law [15] which states:

$$a_{AlGaN} = x \cdot a_{Al} + (1-x) \cdot a_{GaN} \tag{1.2}$$

where x is the percentage of aluminum in the alloy. The tensile strain then can be expressed as:

$$\varepsilon_{ret} = \frac{a_{GaN} - a_{AlGaN}}{a_{AlGaN}} \tag{1.3}$$

where the AlGaN layer is grown on GaN buffer. Since in AlGaN/GaN HEMTs this is always the case, equations 1.2 and 1.3 show that the interface is always under tensile strain (parallel to the spontaneous polarization).

Now that the distribution of the charge in pyroelectrics materials has been explained, the working principle to generate 2DEG in a polar heterostructure will be presented. Consider the AlGaN/GaN structure along with the charge density and the band diagram illustrated in figure 1.4. For the previous considerations, the lattice mismatch between AlGaN and GaN sets the AlGaN cap under tensile strain, hence spontaneous and piezoelectric polarization are parallel.

At the metal/AlGaN interface, the negative polarization charge $-Q_\pi$(AlGaN) is the sum of Q_{SP} and Q_{PZ} contributions, while the positive charge at the surface

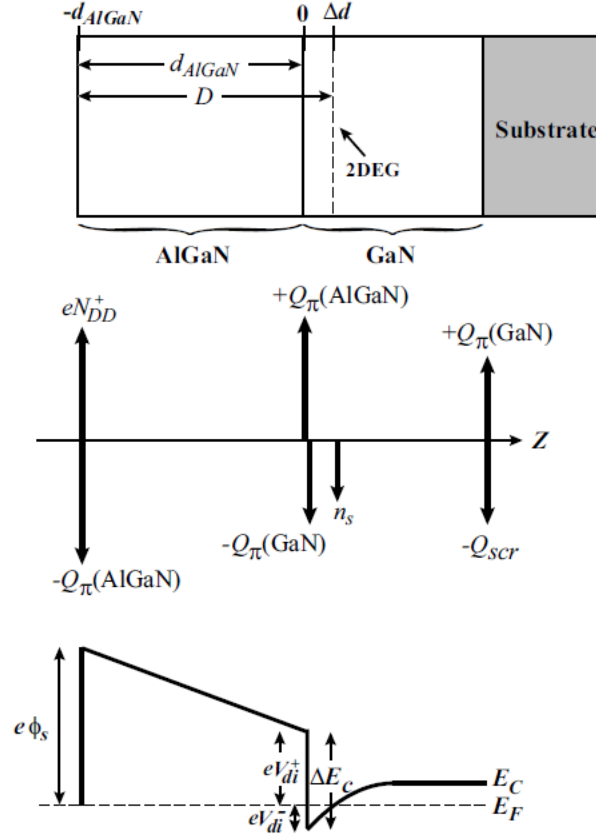

Figure 1.4: Typical AlGaN/GaN heterostructure used in polar HFET technology, along with the charge distribution and the band diagram.

${N_{DD}}^+$ results from the ionized surface donors [2]. At the AlGaN/GaN interface, the sum of the polarization contributions from the AlGaN and GaN will be called net polarization charge Q_π(net):

$$Q_\pi(\text{net}) = Q_\pi(\text{AlGaN}) - Q_\pi(\text{GaN})$$

where $Q_\pi(net)$ is a positive number because of the higher polarization in the AlGaN relative to GaN. The band diagram, shows that the conduction band discontinuity forms one side of the quantum well which, as mentioned in the previous section, is triangular. The 2DEG is in the GaN layer at a distance Δd from the heterointerface, where Δd is the centroid of the charge distribution. To find out the 2DEG carrier density n_s, the analysis starts from the continuity equation at zero bias:

$$\Phi_s - V_1 - \frac{\Delta E_c}{q} + {V_{di}}^- = 0 \tag{1.4}$$

where from [2]

$${V_{di}}^- = \frac{qn_s}{\varepsilon} \cdot \Delta d$$

and

$$V_1 = (Q_\pi(\text{net}) - qn_s) \cdot \frac{d_{AlGaN}}{\varepsilon} = V_b + V_{AlGaN}$$

Substituting these values into equation 1.4 gives:

$$n_s = \frac{\varepsilon(V_b + \Delta E_c/q - \Phi_s)}{q(d_{AlGaN} + \Delta d)}$$

The physical difference between conventional and polar HEMTs is simply in the origin of the electrons in the 2DEG. In the conventional HFETs, the channel electrons are provided by donor sheet, while in GaN-based HFETs, they come from ionized surface donor states. If a gate metal is placed on top of the AlGaN layer and a positive gate voltage is applied, the potential barrier barrier at the metal/AlGaN interface is given by:

$$\Phi_s = \Phi_b - V_G$$

where V_G is the applied voltage and Φ_b is the metal semiconductor barrier height that is given by:

$$\Phi_b = \phi_s - \phi_m$$

and

$$\phi_s = X(\text{AlGaN}) + \frac{E_g(\text{AlGaN})}{2q}$$

Thus, for the AlGaN/GaN HEMT, the 2DEG sheet charge density as function of the gate voltage can be written as:

$$n_s = \frac{\varepsilon(V_b + \Delta E_c/q - \phi_b + V_G)}{q(d_{AlGaN} + \Delta d)} \tag{1.5}$$

The threshold voltage can be calculated from equation 1.5, placing $n_s = 0$ and $V_G = V_{TH}$:

$$V_{TH} = \Phi_b - \frac{\Delta E_c}{q} - V_b \tag{1.6}$$

A complete analysis of the 2DEG charge density starts from solving the Schrödinger's and Poisson's equations. In fact, the 2DEG concentration is related to the position of the Fermi level via Fermi-Dirac distribution by the following equation:

$$n_s = D_s \frac{k_B T}{q} \ln\left[1 + \exp\left(\frac{E_f - E_0}{k_B T}\right)\right]$$

where D_s is the 2DEG density of states and only the first sub-band energy E_0 has been assumed dominant. This approach will be explored later in Chapter 2, which is dedicated to the compact modeling of the AlGaN/GaN HEMT.

1.3 GaN - Impact

Over a long period, R&D institutes and laboratories acts as a pivot in pushing through GaN-based solutions while industrial companies followed from afar. But since then, the situation has changed. Today, it is crystal-clear that, from a theoretical point of view, GaN offers fantastic technical advantages over traditional Si MOSFETs. Even though the current GaN power market remains tiny compared to $32.8B silicon power market, GaN devices are confidently breaking through into different applications [16]. According to the last annual market research report 'Power GaN 2018: Epitaxy, Devices, Applications and Technology Trends' [17], the global gallium nitride semiconductor devices market is expected to reach $500M by 2023. Factors driving the growth of the market are: increasing demand for power efficient electronic devices, rapid advancements in technology and rising investments in R&D by major semiconductor manufacturing companies [18].

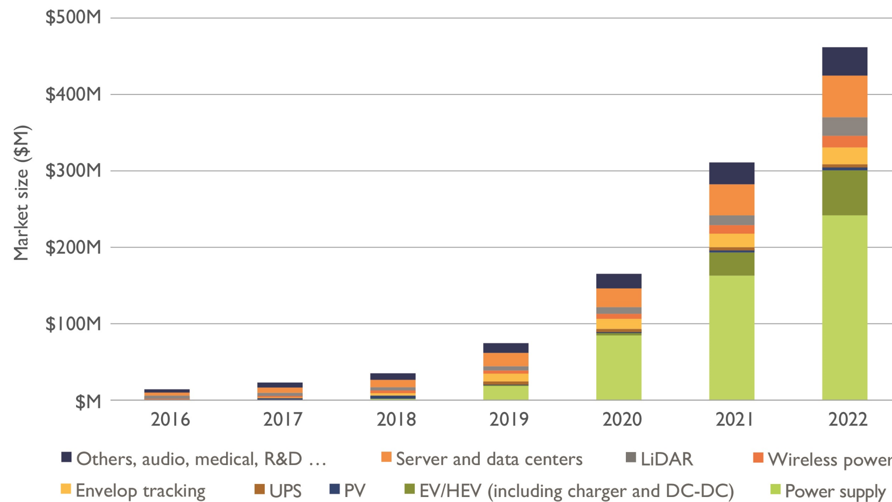

Figure 1.5: Expected impact in the market of GaN technology from the market research firm Yole Déveleppement. The power supply has been identified as the key application leading the economic growth of gallium nitride devices.

Moreover, the rapid adoption of automated devices and increasing usage of the wireless charging are further propelling the market growth. The potential usage of GaN in healthcare sector, in 5G infrastructures, and in aerospace & defence sector is also expected to propel the market growth over the forecast period [16]. However, high product cost of GaN devices may restrain the market growth to some extent.

On the basis of the product, the global gallium nitride semiconductor devices market was dominated by radio frequency semiconductor devices is 2017. To date, a large number of possible applications has been suggested [19]. As shown in figure 1.5, the power semiconductor segment is expected to grow with the highest Compound Annual Growth Rate (CAGR is a business and investing specific term equivalent to the more generic exponential growth rate with an interval of one year).

Many end-use industries are widely opting GaN technology. Key players operating in the global GaN semiconductor devices market include industrial giants like Infineon, ON Semiconductors, STMicroelectronics, Panasonic and Texas Instruments [17]. In particular, several developments in 2018 are highlighting this trend:

- Infineon announced it would start volume production for CoolGaN 400V and 600V e-mode HEMT products by the end of 2018,
- STMicroelectronics and CEA Leti announced their cooperation in developing GaN-onSi technologies for both diode and transistor, and expect to have a validated engineering sample in 2019.

For all the aforementioned reasons, in order to take part in this technological revolution it becomes necessary to understand the operating principle of gallium nitride devices. In the next chapter a physic-based compact model of AlGaN/GaN HEMT will be presented.

Chapter 2

Modeling of D-Mode GaN HEMT

2.1 GaN compact models: Overview

As GaN technology matures in terms of process and fabrication, the focus of GaN research is shifting to modeling and circuit design. Because of this, there is an increasing demand for accurate non-linear models. To create a model that can reproduce the behavior of a device, two approaches can be used:

1. **Empirical Model:** this type of model focus on the selection and combination of mathematical functions to numerically fit the behavior of the model to measured data [20]. Because of their nature, empirical models use a large number of fitting parameters, which have to be extracted by experimental data. The extraction of these parameters is difficult and often ambiguous due to their non-physical nature [21].

2. **Physical Model:** this approach analyzes the causes of the device behavior following the semiconductor physics such as material characteristics and carrier transport. The equations are physical, with a much smaller number of parameters than empirical models [20] and since they have a physical meaning the extraction is easier to facilitate. The physics-based models are the preferred solution because they give better prediction of the statistical variations in the device and follow well-defined geometrical and temperature scaling rules [21].

The SPICE model, which is also known as a compact model, is a set of long equations that combine physical and empirical methods to reproduce the very complex transistor characteristics with high speed and accuracy for SPICE simulations [1]. The model equations contain adjustable parameters that have to be extracted to accurately reproduce the current, capacitance and noise over many orders of magnitude for the entire operating range of terminal voltages, gate lengths and widths, and temperatures. The accuracy of the final result greatly depends on the model equations. BSIM stands for "Berkeley Short-channel Insulated-gate field effect transistor Model". BSIM has been the first industry standard model and continues to be the most popular compact model today. The genesis of BSIM may be traced back to BSIM1 published in 1984 [22], which was followed by BSIM2 in 1988 [23]. BSIM3 [24] was such an improvement over the previous models that the Compact Model Council (CMC), an industry standard organization formed in 1995 to choose,

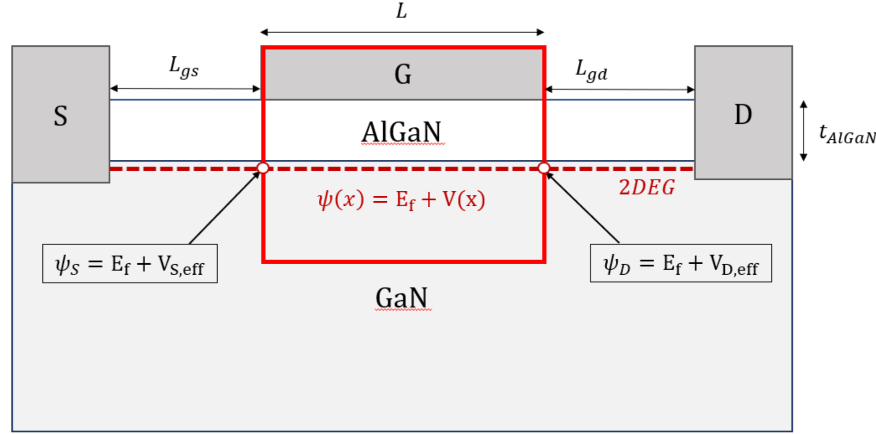

Figure 2.1: Cross Section of the AlGaN/GaN HEMT discussed in this chapter. Inside the red square there is the core module which delimits the intrinsic region and defines the surface potential $\psi_s(x)$, the intrinsic charge in each terminal Q_{gi},Q_{si},Q_{di} and the drain current I_D.

maintain and promote the use of standard semiconductor device models, selected BSIM3v3 as the world's first industry standard model.

A review of the device modeling literature reveals that much work has been done in the area of nonlinear modeling in the contest of GaN HEMT treatment [25]. Some of these models follow an empirical approach like the Angelov [26], EEHEMT [27] and DynaFET [28], while others like the Tsinghua-HKUST [29], MVSG [30] and the ASM GaN [21] follow a physical approach. In 2018, after almost seven years of research and development, the Advance SPICE Model for GaN (ASM GaN) passed all the steps of the CMC standardization process and has been selected as the first industry standard model for gallium nitride transistors [31, 32].

Since the development of a compact model is a long process that requires several years and many resources for testing and verification, the following chapter will not propose a new solution to model the AlGaN/GaN heterostructure but instead address the topic using as main reference the ASM GaN model since it has been recently chosen as new industry standard for GaN HEMT. It is important to note that the mathematical passages given below do not have a single source but are the result of the organic study of numerous papers released between 2011 and 2019. Some passages are intentionally made by the author of the thesis as they are not shown in the reference paper or in the manual. In light of this, this chapter can be considered as a valid tool to understand the physics of GaN devices in a compact and detailed way. The cross-sectional view of the AlGaN/GaN HEMT discussed here is shown in figure 2.1. For the reasons explained in Chapter 1, namely the band gap difference at the AlGaN/GaN interface, a triangular potential well confines the free electrons in the GaN buffer and forms the 2-Dimensional Electron Gas (2DEG). Since a GaN HEMT is such a complex system, in order to clearly organize and represent the physics concept behind it, it is necessary to divide the device model into two separate modules, the **core** module and the **real device effect** module. Each of them will then be divided into several partitions defined by their corresponding physics.

2.2 Core Model

The formation of the 2DEG is the core of the HEMT device operation and a physics-based analytical expression for n_s is a primary requirement in the development of a compact model for these devices. The main difficulty in modeling the 2DEG charge density arise from the complicated variation of the Fermi level E_f. A self-consistent solution of the Schrödinger's and Poisson's equations in the quantum well, assuming triangular profile potential, is expressed from the following system of equations [21]:

$$n_s = D_s \frac{k_B T}{q} \sum_{i=0}^{n} \ln\left[1 + \exp\left(\frac{E_f - E_i}{k_B T}\right)\right] \tag{2.1}$$

$$E_i = \left(\frac{\hbar}{2m^*}\right)^{\frac{1}{3}} \left[\frac{3}{2} q \pi \mathscr{E} \left(i + \frac{3}{4}\right)\right]^{\frac{2}{3}} \tag{2.2}$$

$$\begin{aligned} V_G &= V_{TH} + q n_s \cdot \frac{t_{AlGaN}}{\varepsilon_{AlGaN}} + \frac{E_f}{q} + V(x) \\ &= V_{TH} + V_{AlGaN} + \psi_s(x) \end{aligned} \tag{2.3}$$

where D_s is the 2DEG density of stated and from here on is assumed $D_s = 3.240 \times 10^{13}$ cm^{-2} [33], t_{AlGaN} is the thickness of the AlGaN layer, V_{TH} is the threshold voltage calculated in equation 1.6, E_i are the electron energy levels, $\hbar = h/2\pi$ is the Planck constant, m^* is the density of states effective mass and $V(x)$ represent the surface potential dependence at any point x in the channel. Assuming that the electric field $\mathscr{E}$ in equation 2.2 is generated by only the 2DEG then [2]:

$$\mathscr{E} = \frac{q n_s}{\varepsilon} \tag{2.4}$$

and substituting 2.4 in equation 2.2:

$$E_i \simeq \left(\frac{\hbar}{2m^*}\right)^{\frac{1}{3}} \left[\frac{3}{2} q \pi \left(i + \frac{3}{4}\right)\right]^{\frac{2}{3}} \left(\frac{q n_s}{\varepsilon}\right)^{\frac{2}{3}} = \gamma_i {n_s}^{2/3} \tag{2.5}$$

The coefficients γ_i, in equation 2.5, are explicitly related to the density of state effective mass m^* and therefore material dependent. The experimentally determined value of such parameters will determine the position of the energy level. In the AlGaN/GaN interface only the first and second energy level E_0 and E_1 need to be considered. From here on the value of these energy levels is:

$$\begin{cases} E_0 = 2.12 \times 10^{-12} \cdot {n_s}^{2/3} \\ E_1 = 3.73 \times 10^{-12} \cdot {n_s}^{2/3} \end{cases} \tag{2.6}$$

The next step is to find an accurate and smooth expression to define the surface potential by solving equation 2.1, and 2.6.

2.2.1 Surface Potential

The calculation of the Surface Potential (SP) poses a primary challenge since it starts from equations 2.1 and 2.6 where the solution is transcendental. To obtain n_s and E_f it is assumed that $V_D = V_S = V(x) = 0$. Consequently, the surface potential $\psi_s(x) = E_f/q + V(x)$ will be the same in any point x of the channel. Following the approach proposed by S. Khandelwal *et al.* [21, 34, 35], the variation of the Fermi level with V_G can be divided into three different regions:

1. **Sub-V$_{\mathbf{TH}}$ Region**: where the device is off $E_f^I \ll E_0 \simeq E_1$
2. **Moderate 2DEG Region**: where the device is on and $E_f^{II} < E_0 < E_1$
3. **Strong 2DEG Region**: where the device is on and $E_0 < E_f^{III} < E_1$

The next paragraphs will be dedicated finding the Fermi level and the charge density in each region. If the reader is not interested in the mathematical passages, equations 2.21 and 2.20 are respectively the final expressions of the unified Fermi level E_f^U and the charge density n_s^U valid in all the three working regions.

1. Sub-V$_{\mathbf{TH}}$ Region ($E_f^I \ll E_0 \simeq E_1$)

In this case from equation 2.3, for $n_s^I \simeq 0$, the Fermi level is:

$$E_f^I \simeq q(V_G - V_{TH}) = qV_{G0} \tag{2.7}$$

Since $|E_f^I| \gg E_{0,1}$ then:

$$E_f^I - E_{0,1} \simeq E_f^I$$

Substituting this result in equation 2.1 the value of the charge density can be calculated solving the following system of equations:

$$\begin{cases} n_s^I = \dfrac{C_{AlGaN}}{q} \cdot \left(V_{G0} - \dfrac{E_f^I}{q} \right) \\ n_s^I = 2D_s \dfrac{k_B T}{q} \exp\left(\dfrac{E_f^I}{k_B T} \right) \end{cases}$$

where the value of the gate capacitance is given by $C_{AlGaN} = \varepsilon_{AlGaN}/t_{AlGaN}$ and depends from the Aluminum percentage in the AlGaN layer and its thickness. After some simple calculations, the charge density is given by:

$$n_s^I = 2D_s \frac{k_B T}{q} \exp\left(\frac{q}{k_B T} \left(V_{G0} - \frac{q n_s^I}{C_{AlGaN}} \right) \right)$$

and since $n_s^I \simeq 0$ then the value of the charge density in the Sub-V_T Region is:

$$\boxed{n_s^I = 2D_s \frac{k_B T}{q} \exp\left(\frac{qV_{G0}}{k_B T} \right)} \tag{2.8}$$

and from equation 2.3 the Fermi level can be expressed as:

$$\boxed{E_f^I = qV_{G0} - 2D_s \frac{q k_B T}{C_{AlGaN}} \exp\left(\frac{qV_{G0}}{k_B T} \right)} \tag{2.9}$$

2. Moderate 2DEG Region ($E_f^{II} < E_0 < E_1$)

In this region the 2DEG is forming and since: $\exp(E_f^{II} - E_1) \ll \exp(E_f^{II} - E_0)$, then, the second energy level can be neglected. From the notable special limits:

$$\lim_{f(x)\to 0} \ln[1 + f(x)] = f(x)$$

Then, since $\exp(E_f^{II} - E_0) \simeq 0$:

$$\ln\left[1 + \exp\left(\frac{E_f^{II} - E_0}{k_B T}\right)\right] = \exp\left(\frac{E_f^{II} - E_0}{k_B T}\right) \tag{2.10}$$

and substituting equation 2.10 and equation 2.6 in equation 2.1:

$$n_s^{II} = D_s \frac{k_B T}{q} \exp\left(\frac{E_f^{II} - \gamma_0 (n_s^{II})^{2/3}}{k_B T}\right)$$

The value of the charge density can be calculated again solving the following system of equations:

$$\begin{cases} n_s^{II} = \dfrac{C_{AlGaN}}{q} \cdot \left(V_{G0} - \dfrac{E_f^{II}}{q}\right) \\ n_s^{II} = D_s \dfrac{k_B T}{q} \exp\left(\dfrac{E_f^{II} - \gamma_0 (n_s^{II})^{2/3}}{k_B T}\right) \end{cases}$$

The system can be solved explicating the Fermi level:

$$\Longrightarrow \begin{cases} n_s^{II} = \dfrac{C_{AlGaN}}{q} \cdot \left(V_{G0} - \dfrac{E_f^{II}}{q}\right) \\ E_f^{II} = \dfrac{k_B T}{q} \ln\left(\dfrac{q}{k_B T} \dfrac{n_s^{II}}{D_s}\right) + \gamma_0 (n_s^{II})^{2/3} \end{cases}$$

Then:

$$E_f^{II} = \frac{k_B T}{q} \ln\left[\frac{C_{AlGaN}}{D_s k_B T}(V_{G0} - E_F^{II})\right] + \gamma_0 \frac{C_{AlGaN}}{q}(V_{G0} - E_f^{II})^{2/3}$$

and finally [34]:

$$E_f^{II} = V_{G0} \cdot \frac{\ln(\beta V_{G0}) + \gamma_0 \left(\dfrac{C_{AlGaN} V_{G0}}{q}\right)^{2/3}}{V_{G0} + V_{th} + \dfrac{2}{3}\gamma_0 \left(\dfrac{C_{AlGaN} * V_{G0}}{q}\right)^{2/3}} \tag{2.11}$$

where

$$\beta = \frac{C_{AlGaN}}{D_s k_B T} \quad \text{and} \quad V_T = \frac{k_B T}{q} \tag{2.12}$$

and from equation 2.3 the charge density in Moderate 2DEG Region is:

$$n_s^{II} = \frac{C_{AlGaN} V_{G0}}{q} \cdot \frac{V_{G0} + V_T \cdot [1 - \ln(\beta V_{G0})] - \dfrac{1}{3}\gamma_0 \left(\dfrac{C_{AlGaN} V_{G0}}{q}\right)^{2/3}}{V_{G0} + V_T + \dfrac{2}{3}\gamma_0 \left(\dfrac{C_{AlGaN} V_{G0}}{q}\right)^{2/3}} \tag{2.13}$$

3. Strong 2DEG Region $(E_0 < E_f^{III} < E_1)$

In this region the 2DEG is formed and again since: $\exp(E_f^{III} - E_1) \ll \exp(E_f^{III} - E_0)$, then, the second energy level can be neglected. From the notable special limits:

$$\lim_{f(x)\to\infty} \ln[1 + f(x)] = \ln[f(x)]$$

Then, since $\exp(E_f^{III} - E_0) \gg 1$:

$$\ln\left[1 + \exp\left(\frac{E_f^{III} - E_0}{k_B T}\right)\right] = \ln\left[\exp\left(\frac{E_f^{III} - E_0}{k_B T}\right)\right] = \frac{E_f^{III} - E_0}{k_B T} \tag{2.14}$$

and substituting equation 2.14 and equation 2.6 in equation 2.1:

$$n_s^{III} = D_s \frac{k_B T}{q} \left(\frac{E_f^{III} - \gamma_0 (n_s^{III})^{2/3}}{k_B T}\right)$$

The value of the charge density can be calculated solving the following system of equations:

$$\begin{cases} n_s^{III} = \dfrac{C_{AlGaN}}{q} \cdot \left(V_{G0} - \dfrac{E_f^{III}}{q}\right) \\ n_s^{III} = \dfrac{D_s}{q} \left[E_f^{III} - \gamma_0 (n_s^{III})^{2/3}\right] \end{cases}$$

and explicating the Fermi level:

$$\Longrightarrow \begin{cases} n_s^{III} = \dfrac{C_{AlGaN}}{q} \cdot \left(V_{G0} - \dfrac{E_f^{III}}{q}\right) \\ E_f^{III} = \dfrac{n_s}{D_s} + \gamma_0 n_s^{2/3} \end{cases}$$

Then:

$$E_f^{III} = \frac{C_{AlGaN}}{q D_s} (V_{G0} - E_F^{III}) + \gamma_0 \frac{C_{AlGaN}}{q} (V_{G0} - E_f^{III})^{2/3}$$

and finally [34]:

$$E_f^{III} = V_{G0} \cdot \frac{V_T \beta V_{G0} + \gamma_0 \left(\dfrac{C_{AlGaN} V_{G0}}{q}\right)^{2/3}}{V_{G0}\left(1 + V_T \beta\right) + \dfrac{2}{3}\gamma_0 \left(\dfrac{C_{AlGaN} V_{G0}}{q}\right)^{2/3}} \tag{2.15}$$

and from equation 2.3 the charge density is Strong 2DEG Region is:

$$n_s^{III} = \frac{C_{AlGaN} V_{G0}}{q} \cdot \frac{V_{G0} - \dfrac{1}{3}\gamma_0 \left(\dfrac{C_{AlGaN} V_{G0}}{q}\right)^{2/3}}{V_{G0}\left(1 + V_T \beta\right) + \dfrac{2}{3}\gamma_0 \left(\dfrac{C_{AlGaN} V_{G0}}{q}\right)^{2/3}} \tag{2.16}$$

Unified Model for Charge Density and Fermi level

An important issue when implementing a compact model is the discontinuity between the working regions. A good compact model have to be defined by equations that are smooth and continuous for several orders of derivatives.

In order to find a unifying expression for E_f and n_s applicable for the full range of operation, it is useful to notice that equations 2.11, 2.13 and 2.15, 2.16 respectively, differ only by one term at the numerator and one term at the denominator, both with a factor given by the thermal voltage $V_T = k_B T/q$ defined in equation 2.12. An approximated unified expression for the above cut-off Region (II + III) can be obtained by removing all terms with the thermal voltage V_{th}. However, to improve accuracy, S. Khandelwal proposed a new algorithm to obtain a unified solution first for Region II + III [34]:

$$n_s^{(II+III)} = \frac{C_{AlGaN} V_{G0}}{q} \cdot H(V_{G0}) \tag{2.17}$$

$$E_f^{(II+III)} = V_{G0}(1 - H(V_{G0})) \tag{2.18}$$

where

$$H(V_{G0}) = \frac{V_{G0} + V_T[1 - \ln(\beta V_{G0n})] - \frac{1}{3}\gamma_0 \left(\frac{C_{AlGaN} V_{G0}}{q}\right)^{2/3}}{V_{G0}\left(1 + \frac{V_T}{V_{G0d}}\right) + \frac{2}{3}\gamma_0 \left(\frac{C_{AlGaN} V_{G0}}{q}\right)^{2/3}} \tag{2.19}$$

Here, V_{G0n} and V_{G0d} are functions of V_{G0} given in [21] by the interpolation expression:

$$V_{G0x} = \frac{V_{G0}\alpha_x}{\sqrt{V_{G0}^2 + \alpha_x^2}} \quad \text{where} \quad \alpha_n = \frac{e}{\beta} \quad \text{and} \quad \alpha_d = \frac{1}{\beta}$$

Then for the full range of gate voltages [21, 35], obtaining a single continuous unified expression for the charge density:

$$n_s^U = 2V_T C_{AlGaN} \cdot \frac{\ln\left[1 + \exp\left(\frac{V_{G0}}{2V_T}\right)\right]}{\frac{1}{H(V_{G0})} + \frac{C_{AlGaN}}{qD_s}\exp\left(-\frac{V_{G0}}{2V_T}\right)} \tag{2.20}$$

and the Fermi level:

$$E_f^U = V_{G0} - 2V_T \cdot \frac{\ln\left[1 + \exp\left(\frac{V_{G0}}{2V_T}\right)\right]}{\frac{1}{H(V_{G0})} + \frac{C_{AlGaN}}{qD_s}\exp\left(-\frac{V_{G0}}{2V_T}\right)} \tag{2.21}$$

From equation 2.20, is easy to observe that equation 2.17 is obtained for $V_G > V_{TH}$ while 2.8 is obtained for $V_G < V_{TH}$. In figure 2.2, the vertical voltage drop in each

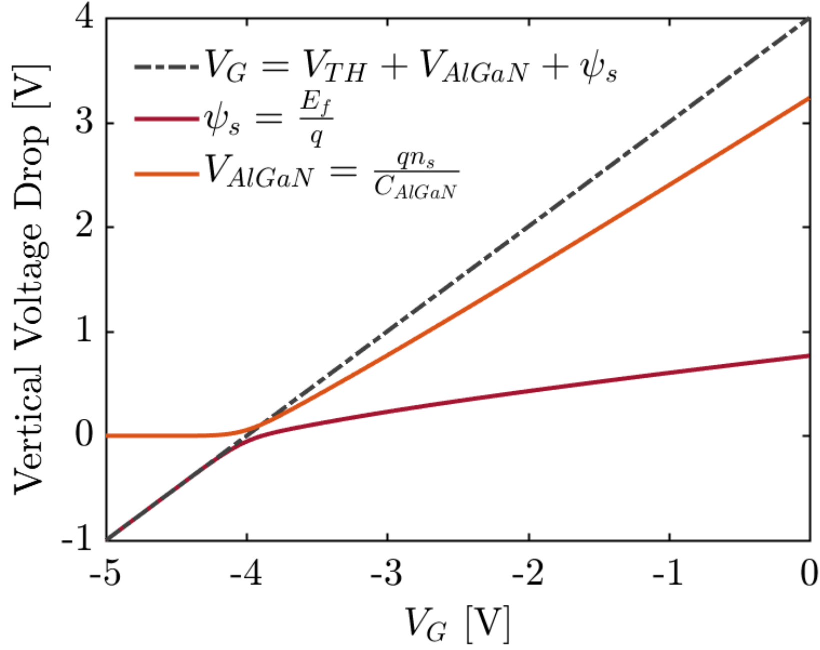

Figure 2.2: Matlab simulation of the gate vertical voltage drop, defined in equation 2.3, in an AlGaN/GaN structure with threshold $V_{TH} = -4$ V, where the AlGaN layer has 20% Aluminum and thickness $t_{AlGaN} = 16$ nm.

layer under the gate, is plotted using together the calculated unified Fermi level and equation 2.3. The charge density used to evaluate the voltage drop in the AlGaN layer V_{AlGaN} is plotted in figure 2.3. The obtained result has an accuracy in order of millivolts [21]. This is because in the calculation of Region II and III the energy level E_1 has been neglected. This can be a problem in particular during the transition between Region I and II where the energy levels E_0 and E_1 are very close to each other and they should both be considered to calculate E_f.

For a SP-compact model, accuracy better than nanovolts is desirable [35]. For this reason the solution given in equation 2.21 has to be improved including E_1. To do so the ASM GaN model follows the Householder's method for solving implicit functions [36]. The obtained solution is:

$$E_f^H = E_f^U - \frac{p}{q}\left(1 + \frac{pr}{2q^2}\right) \tag{2.22}$$

where the quantities $k_{0,1}$,$\mathscr{E}_{0,1}$,V_{Geff},p,q and r are defined in table 2.1. Using this method, the obtained accuracy is in the order of femtovolts. The unified E_f^H obtained in equation 2.22 can be used to calculate the surface potential at both ends of the channel, in fact:

$$\psi_s(x) = E_f^H + V(x) \tag{2.23}$$

Now that a continuous and smooth expression for the surface potential has been calculated, it can be used to evaluate the intrinsic charge in each terminal of the device Q_G, Q_S and Q_D in a very precise way.

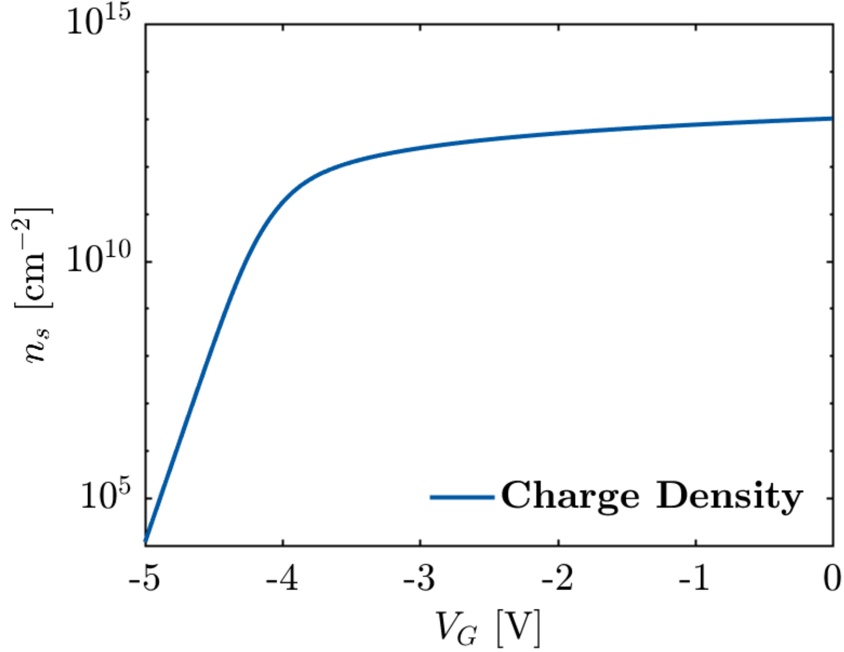

Figure 2.3: Matlab simulation of the charge density used to evaluate the vertical voltage drop of the AlGaN/GaN structure in figure 2.2.

Quantity	Expression	Quantity	Expression
$\mathscr{E}_{0,1}$	$\exp\left(\frac{E_f^U - k_{0,1} V_{Geff}^{2/3}}{k_B T}\right)$	p	$\frac{C_{AlGaN}}{q} V_{Geff} - \sum_{i=0}^{1} D_s V_T \ln(\mathscr{E}_i + 1)$
V_{Geff}	$V_G - V_{TH} - E_f^U$	q	$-\frac{C_{AlGaN}}{q} - \sum_{i=0}^{1} \frac{D_s}{1+\mathscr{E}_i^{-1}} \cdot \left(1 + \frac{2}{3} k_i V_{Geff}^{-2/3}\right)$
$k_{0,1}$	$\gamma_{0,1} \frac{C_{AlGaN}}{q}^{2/3}$	r	$\sum_{i=0}^{1} \frac{\frac{2}{9} D_s k_i (1+\mathscr{E}_i^{-1}) V_{Geff}^{-4/3} + \frac{D_s}{V_T}\left(1+\frac{2}{3} k_i V_{Geff}^{-1/3}\right)^2}{(1+\mathscr{E}_i^{-1})^2}$

Table 2.1: Quantities to increase the Fermi level accuracy using Householder method

2.2.2 Intrinsic Charge

Terminals Potential

Before starting the calculation of the intrinsic charge in each terminal is important to understand what is their corresponding potential. To do so, equation 2.23 has to be discussed since significant effects such as the saturation velocity and the mobility have to be taken into account when calculating the intrinsic potential in each terminal. On the source side:

$$\psi_S = E_f^H + V_{S,eff} \tag{2.24}$$

where, referring to the cross section of a general AlGaN/GaN Schottky HEMT in figure 2.1, $V_{S,eff} = V_{Si}$ that is the intrinsic source voltage. Regarding the drain side:

$$\psi_D = E_f^H + V_{D,eff} \tag{2.25}$$

In this case, the calculation of $V_{D,eff}$ can be done as follow:

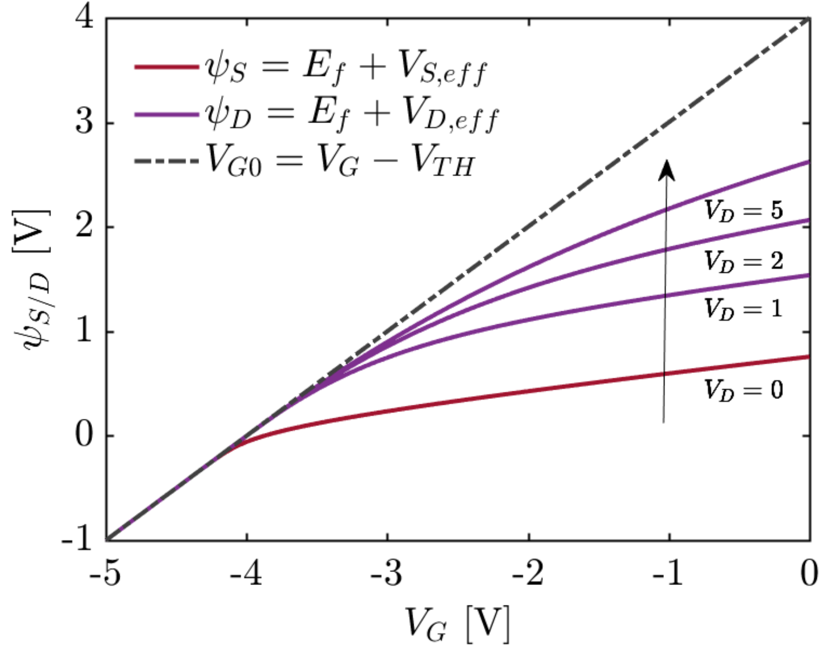

Figure 2.4: Matlab simulation of the surface potential, in source (ψ_S) and drain (ψ_D) side, for different V_D in AlGaN/GaN structure with gate length $L = 5 \times 10^{-4}$ cm, threshold $V_{TH} = -4$ V, electron mobility $\mu_s = 1500$ cm^2/Vs, velocity saturation $v_S = 1 \times 10^7$ cm/s, where the AlGaN layer has 20% Aluminum and thickness $t_{AlGaN} = 16$ nm.

$$V_{D,sat} = 2L \cdot \frac{v_S}{\mu} \cdot \frac{V_{G0}}{V_{G0} + 2L \cdot \frac{v_S}{\mu}}$$

and

$$V_{D,eff} = \frac{V_{Di}}{\sqrt{1 + \left(\frac{V_{Di}}{V_{D,sat}}\right)^2}} \tag{2.26}$$

where L (cm) is the gate length, μ (cm^2/Vs) is the electron mobility and v_S (cm/s) is the electron velocity saturation which are determined by the material properties. In figure 2.4, the ψ_S and ψ_D are plotted with $V_S = 0$ V and $V_D = [0, 1, 2, 5]$ V using Matlab. As expected, when $V_D = V_S = 0$ the potential is only determined by the Fermi level and $\psi_S = \psi_D$. To conclude this preamble concerning how the potential is calculated in the channel, from here on is useful to define the following quantities:

$$\begin{cases} \psi_m = \dfrac{\psi_D + \psi_S}{2} \\ \psi_{ds} = \psi_D - \psi_S \end{cases} \tag{2.27}$$

where ψ_m is the average surface potential and ψ_{ds} is the differential potential between the drain and source terminal.

Charge Calculation

The model of the intrinsic charge is normally done assigning drain charge and the source charge as $Q_{Di} = x_p \cdot Q_{ch}$ and $Q_{Si} = (1-x_p)\cdot Q_{ch}$ respectively, where Q_{ch} is the channel charge and x_p is the partitioning factor. To simplify the problem, is quite common to see standard compact models, such as BSIM4 [37], make use of simplified schemes like 60/40 and 50/50. A more rigorous and physical way is proposed in [35] defining:

$$\begin{cases} Q_{Di} = \int_0^L \frac{x}{L} \cdot Q_{ch}(V_G, V_x)\,dx \\ Q_{Si} = \int_0^L \frac{1-x}{L} \cdot Q_{ch}(V_G, V_x)\,dx \\ Q_{Gi} = -(Q_{Si} + Q_{Di}) \end{cases}$$

where the third equation is given by the conservation of the charge. Using these definitions, the total intrinsic charge Q_{Gi} can be written as:

$$\begin{cases} n_s = \frac{C_{AlGaN}}{q} \cdot \left(V_G - V_{TH} - \frac{E_f}{q} - V_x \right) \\ Q_{Gi} = \int_0^L qWn_s(V_G, V_x)\,dx \end{cases}$$

$$\Longrightarrow Q_{Gi} = \int_0^L WC_{AlGaN} \cdot (V_{G0} - \psi_s(x))\,dx \tag{2.28}$$

To perform the integration, in [32] is proposed to change the integration variable:

$$dx = \frac{L(V_{G0} - \psi + V_T)}{(V_{G0} - \psi_m + V_T)(\psi_D - \psi_S)} d\psi \tag{2.29}$$

where V_{G0}, V_T and ψ_m are defined in equations 2.7, 2.12 and 2.27 respectively. From this, equation 2.28 can be solved:

$$Q_{Gi} = \int_{\psi_S}^{\psi_D} LWC_{AlGaN} \cdot \frac{(V_{G0} - \psi)(V_{G0} - \psi + V_T)}{(V_{G0} - \psi_m + V_T)(\psi_D - \psi_S)} d\psi \tag{2.30}$$

$$
\begin{aligned}
Q_{Gi} &= \frac{WLC_{AlGaN}}{(V_{G0}-\psi_m+V_T)(\psi_D-\psi_S)} \cdot \int_{\psi_S}^{\psi_D} (V_{G0}-\psi)^2 + V_T(V_{G0}-\psi)\,d\psi \\
&= \frac{\Upsilon}{\psi_{ds}} \left(V_T V_{G0}\psi_{ds} + \int_{\psi_S}^{\psi_D} V_{G0}^2 - \psi(2V_{G0}+V_T) + \psi^2\,d\psi \right) \\
&= \frac{\Upsilon}{\psi_{ds}} \left(V_T V_{G0}\psi_{ds} + V_{G0}\psi_{ds} - (2V_{G0}+V_T)\cdot \frac{(\psi_D^2-\psi_S^2)}{2} + \frac{\psi_D^3-\psi_S^3}{3} \right) \\
&= \frac{\Upsilon}{\psi_{ds}} \left(V_{G0}(V_T+V_{G0})\psi_{ds} - (2V_{G0}+V_T)\psi_m\psi_{ds} + \frac{\psi_D^2+\psi_S^2+\psi_D\psi_S}{3}\cdot\psi_{ds} \right) \\
&= \Upsilon \left(V_{G0}(V_T+V_{G0}) - (2V_{G0}+V_T)\psi_m + \frac{\psi_D^2+\psi_S^2+\psi_D\psi_S}{3} \right)
\end{aligned}
$$

where

$$\Upsilon = \frac{WLC_{AlGaN}}{(V_{G0}-\psi_m+V_T)}$$

The final expression of the intrinsic gate charge is:

$$
\begin{aligned}
Q_{Gi} = \frac{WLC_{AlGaN}}{(V_{G0}-\psi_m+V_T)} \Big(& V_{G0}(V_{G0}+V_T-2\psi_m) \\
& - V_T\psi_m + \frac{\psi_D^2+\psi_S^2+\psi_D\psi_S}{3} \Big)
\end{aligned}
\tag{2.31}
$$

Now that the total charge in the channel has been calculated, the source and drain terminal charges are given by the following system of equations:

$$
\begin{cases}
Q_{Di} = \displaystyle\int_0^L \frac{x}{L}\cdot Q_{Gi}\,dx \\
Q_{Si} = -(Q_{Gi}+Q_{Di})
\end{cases}
$$

To calculate the total drain charge, equation 2.29 is integrated from the source to an arbitrary point x as follow:

$$\int_0^x dx = \int_{\psi_S}^{\psi(x)} \frac{L(V_{G0}-\psi+V_T)}{(V_{G0}-\psi_m+V_T)(\psi_D-\psi_S)} d\psi$$

resulting in:

$$x = \frac{L(\psi-\psi_S)}{(V_{G0}-\psi_m+V_T)\psi_{ds}} \left(V_{G0}+V_T-\frac{\psi+\psi_S}{2} \right)$$

From this, the drain charge can be expressed as:

$$Q_{Di} = \int_{\psi_S}^{\psi_D} \frac{L(\psi-\psi_S)}{(V_{G0}-\psi_m+V_T)\psi_{ds}} \left(V_{G0}+V_T-\frac{\psi+\psi_S}{2} \right) Q_{Gi}\,d\psi$$

The integral can be solved with the same methodology used to calculated the gate charge. The final expression of the intrinsic drain charge is given in [35]:

$$Q_{Di} = \frac{WLC_{AlGaN}}{120(V_{G0} - \psi_m + V_T)^2} \big[\psi_S^2 (16\psi_D - 5(V_T + 8V_{G0})) + 2\psi_S (12\psi_S^2 - 5\psi_D (5V_T + 8V_{G0}) + 10(V_T + V_{G0})(V_T + 4V_{G0})) + 15\psi_D^2 (3V_T + 4V_{G0}) - 60V_{G0}(V_T + V_{G0})^2 + 12\psi_D^3 + 8\psi_S^3 + 20\psi_D (V_T + V_{G0})(2V_T + 5V_{G0}) \big] \tag{2.32}$$

and the intrinsic source charge is:

$$Q_{Si} = -(Q_{Gi} + Q_{Di}) \tag{2.33}$$

From equation 2.31, 2.32 and 2.33 all the terminal capacitances can be calculated as follow:

$$\begin{cases} C_{Gi} = \dfrac{dQ_{Gi}}{dV_G} + \dfrac{dQ_{Gi}}{dV_S} + \dfrac{dQ_{Gi}}{dV_D} \\ C_{Di} = \dfrac{dQ_{Di}}{dV_G} + \dfrac{dQ_{Di}}{dV_S} + \dfrac{dQ_{Di}}{dV_D} \\ C_{Si} = \dfrac{dQ_{Si}}{dV_G} + \dfrac{dQ_{Si}}{dV_S} + \dfrac{dQ_{Si}}{dV_D} \end{cases} \tag{2.34}$$

In the simplified case where $V_D = V_S = 0$, the gate capacitance can be calculated from equation 2.3 and 2.31:

$$\begin{cases} \dfrac{1}{C_G} = \dfrac{dV_G}{dQ_G} \\ V_G = V_{TH} + V_{AlGaN} + \psi_s(x) \end{cases}$$

Then:

$$\begin{aligned} C_G &= \left(\frac{d(V_{TH} + V_{AlGAN} + \psi_s)}{dQ_G} \right)^{-1} \\ &= \left(\frac{dV_{AlGAN}}{dQ_G} + \frac{d\psi_s}{dQ_G} \right)^{-1} \\ &= \left(\frac{1}{C_{AlGaN}} + \frac{1}{C_s} \right)^{-1} \end{aligned} \tag{2.35}$$

From equation 2.35, the gate capacitance is given by the series of the AlGaN capacitance (that is constant $C_{AlGaN} = \varepsilon_{AlGaN}/t_{AlGaN}$ and defined by the geometries of the device) and the surface capacitance that will increase with the increase of the 2DEG charge.

In order to study the precision of the model, it has been implemented, using Verilog-A code, in the electronic design automation software Advanced Design System (ADS) by Keysight EEsof EDA. The simulation result has been compared with

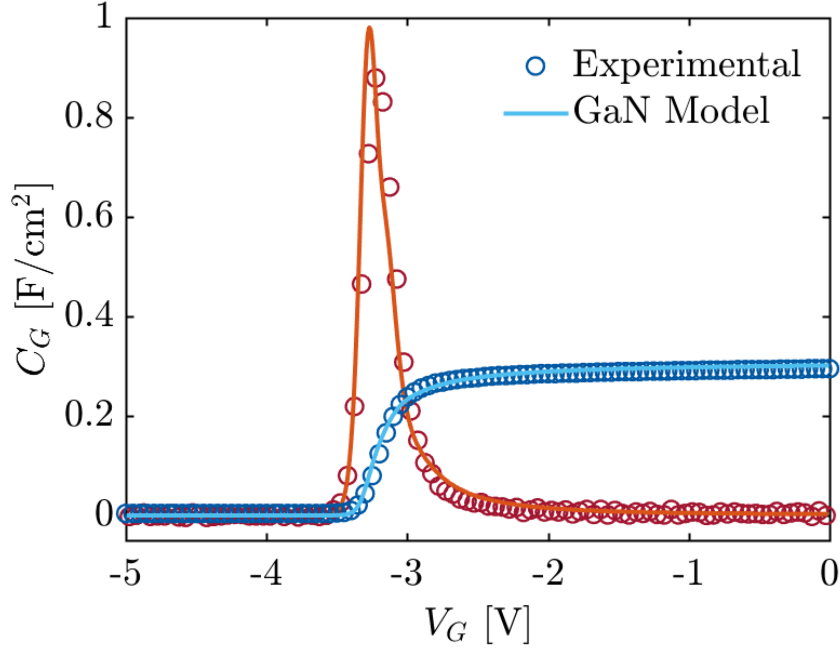

Figure 2.5: Simulation vs experimental data on a Schottky HEMT with a diameter of 120 nm, where the AlGaN layer has thickness 20 nm and 24% of Al. The Figure shows excellent agreement in the result, also for the first order derivative. The simulation is performed implementing the Verilog-A code in ADS.

real experimental data performed on a Schottky HEMT with a diameter of 120 nm, where the AlGaN layer has a thickness of 20 nm and 24% of Aluminum.

The real measurement of the gate capacitance is usually done in a dedicated structure with a 2 terminal AlGaN/GaN device (equivalent to the described model with $V_S = V_D = 0$). The experiment is performed probing the device with a sinusoidal gate voltage at different DC levels. Figure 2.5 shows excellent agreement between the proposed model and the experimental data (comparing also the first derivative), while figure 2.6 shows the contribution of each capacitance.

2.2.3 Drain Current

The calculation of the drain current at any point x along the channel, is done under the gradual channel approximation with drift diffusion model [38]. The ballistic conduction mechanism is not taken in to account because the channel length of GaN HEMT devices is big enough to neglect this effect. Under this conditions the drain current can be expressed as:

$$I_D = -\mu W Q_{ch} \frac{d\psi}{dx} + \mu W \frac{dQ_{ch}}{dx} V_T$$

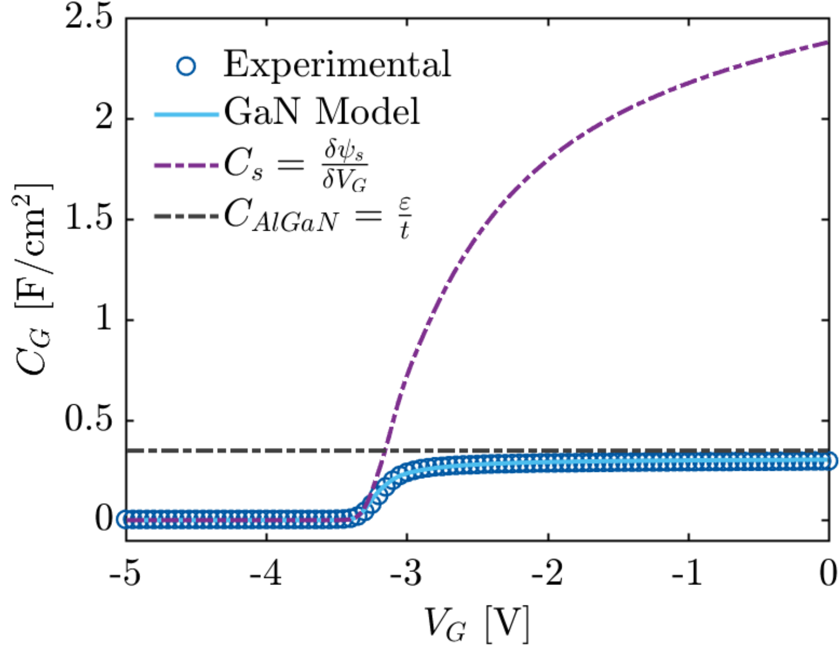

Figure 2.6: The Figure shows the contribution of surface and AlGaN capacitance used to calculate the gate capacitance using equation 2.35. The experimental data comes from the same device of figure 2.5. The simulation is performed implementing the Verilog-A code in ADS.

Then, using $Q_{ch} = qn_s = C_{AlGaN}(V_{G0} - \psi_s(x))$ from equation 2.3, taking dx to the left side and integrating it from 0 to L:

$$
\begin{aligned}
I_D &= -\mu \frac{W}{L} Q_{ch} \cdot d\psi + \mu W V_T \cdot dQ_{ch} \\
&= -\mu \frac{W}{L} C_{AlGaN}[(V_{G0} - \psi) \cdot d\psi - V_T \cdot d(V_{G0} - \psi)]
\end{aligned}
$$

The integration of the right term can be done as follow:

$$
\begin{aligned}
I_D &= -\mu \frac{W}{L} C_{AlGaN} \int_{\psi_D}^{\psi_S} V_{G0} - \psi + V_T \cdot d\psi \\
&= \mu \frac{W}{L} C_{AlGaN} \left(\psi V_{G0} + \psi V_T - \frac{\psi^2}{2} \right) \Big|_{\psi_S}^{\psi_D}
\end{aligned}
$$

The resulting drain current is given by:

$$
\boxed{I_D = \mu \frac{W}{L} C_{AlGaN}(V_{G0} - \psi_m + V_T) \cdot \psi_{ds}} \tag{2.36}
$$

2.3 Real Device Effects

The ASM GaN model includes different sub-modules to describe different real device physical effects. In the following section, the discussion will be focused exclusively to the effects that are taken into account in Chapter 3 and 4.

2.3.1 Mobility Degradation

The carrier mobility in the channel for HEMT devices is found to depend on the 2DEG charge density, which depends on the electrical electric field. In [39], the physical description of the mobility degradation due to the vertical electric field is modeled as:

$$\mu_{eff} = \frac{\mu_0}{1 + \mu_A \mathscr{E}_{y,eff} + \mu_B \mathscr{E}_{y,eff}^2} \tag{2.37}$$

where μ_0 is the low field mobility, μ_A and μ_B are model degradation parameters to be extracted from experimental data and $\mathscr{E}_{y,eff}$ is the effective vertical electric field calculated using the Gauss's law as:

$$\frac{d\mathscr{E}(x)}{dx} = \frac{\rho(x)}{\varepsilon_{AlGaN}} \Longrightarrow \mathscr{E}_{y,eff} = \frac{\overline{Q_{ch}}}{\varepsilon_{AlGaN}} = \frac{C_{AlGaN}}{\varepsilon_{AlGaN}}(V_{G0} - \psi_m)$$

where $\overline{Q_{ch}} = C_{AlGaN}(V_{G0} - \psi_m)$ is the average channel charge.

2.3.2 Short Channel Effects

Velocity Saturation

With the increase in the lateral electric field, the carriers gain sufficient energy to be scattered by optical phonons, resulting in a decrease in their mobility and ultimately saturation of the carrier velocity [38]. To account for this effect, equation 2.37 is modified as:

$$\mu_{eff,SAT} = \frac{\mu_{eff}}{\sqrt{1 + \left(\frac{\mu_{eff}}{v_S \cdot \mathscr{E}_x}\right)^2}} \tag{2.38}$$

where $\mathscr{E}_x = (\psi_d - \psi_S)/L = \psi_{ds}/L$ is the lateral electric field and v_S is the velocity saturation.

DIBL

The Drain Induced Barrier Lowering (DIBL) effect is a short-channel effect referring to a reduction of threshold voltage on the transistor at higher drain voltages [4]. The barrier lowering increases as channel length is reduced, To account this model, the threshold voltage is modified as:

$$\begin{aligned} V_{TH} &= V_{TH0} + \Delta V_{DIBL} \\ &= V_{TH0} - \eta_0 \cdot \frac{V_{DS}}{\sqrt{1 + \left(\frac{V_{DS}}{V_{D,scale}}\right)^2}} \end{aligned} \tag{2.39}$$

where η_0 and $V_{D,scale}$ are parameters that have to be extracted from experimental data.

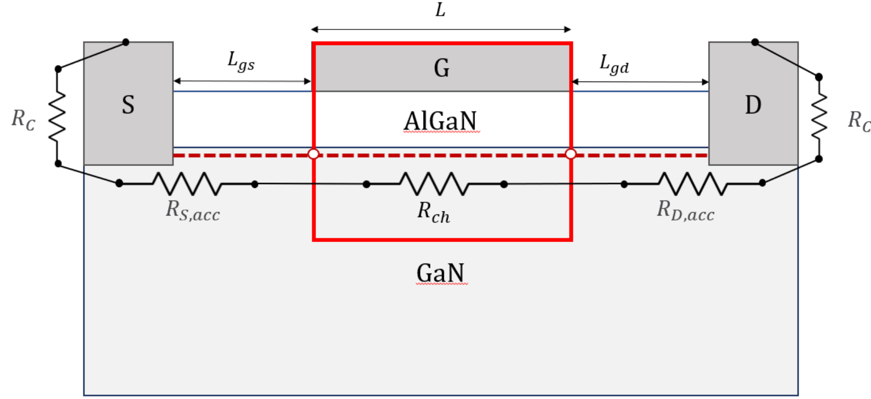

Figure 2.7: Cross Section of the AlGaN/GaN HEMT from figure 2.1, highlighting the effect of the access region resistances in the calculation of the ON resistance.

Channel Length Modulation

The Channel Length Modulation (CLM) effect, which occurs for drain voltages higher than the saturation voltage, is a decrease in the effective length of the channel as the saturation point starts to move toward the source [40]. The CLM on the drain current is modeled modifying equation 2.36 as follow:

$$I_{D,CLM} = I_D[1+\lambda(V_{DS}-V_{D,eff})] = I_D(1+\lambda V_{DSx}) \tag{2.40}$$

where $V_{D,eff}$ is defined in equation 2.26 and λ has to be extracted from experimental data. Using equations 2.37, 2.38 and 2.40, the drain current in equation 2.36 can be rewritten as:

$$I_D = \frac{\mu_{eff}\cdot C_{AlGaN}}{\sqrt{1+\left(\frac{\mu_{eff}}{v_S\cdot \mathscr{E}_x}\right)^2}}\frac{W}{L}(V_{G0}-\psi_m+V_T)(1+\lambda V_{DSx})\cdot\psi_{ds} \tag{2.41}$$

2.3.3 Access Region Resistance

Since the distance between gate edge and drain/source edges are large and usually in the order of few μm, gate-to-drain/source access region plays an important role in defining the drain current [41]. In figure 2.7 is highlighted the effect of the access resistance in the cross section of the AlGaN/GaN HEMT.

The total ON-Resistance consists of two bias independent contact resistance R_C, the intrinsic channel resistance R_{ch} and the access region resistance $R_{D/S,acc}$ which is not linear and depends on the amount of current flowing through this region. The current in the access region can be defines as:

$$I_{acc} = Wqn_{s,acc}\cdot v_{acc} = Q_{acc}\cdot v_{acc} \tag{2.42}$$

where $n_{s,acc}$ is the charge density in the accumulation region which, being far from the gate and the drain contacts, is supposed to be constant and v_{acc} is the electron

velocity [41]. As $n_{s,acc}$ does not increase significantly with increasing of V_D, to support the increasing current, v_{acc} should increase. Initially the electron velocity increase linearly, but then it saturates to the saturation carrier velocity $v_{S,acc}$.

$R_{D/S,acc}$ determines a voltage drop V_R between the drain contact and the intrinsic region across the access region. The transition between the linear and the saturated electron velocity is made smooth and continuous using a classic interpolation scheme that has been used several times along the chapter:

$$v_{acc} = v_{S,acc} \cdot \frac{V_R}{\sqrt{V_R^2 + V_{R,SAT}^2}} \tag{2.43}$$

where

$$V_{R,SAT} = L_{acc} \frac{v_{S,acc}}{\mu_{0,acc}}$$

L_{acc} is the length of the access region given by the distance from the gate to the drain/source and $\mu_{0,acc}$ is the mobility at low field of the electrons in the access region. Combining equations 2.42 and 2.43 we obtain:

$$I_{acc} = \frac{Q_{acc} \cdot v_{S,acc}}{\sqrt{1 + \left(\frac{V_{R,SAT}}{V_R}\right)^2}} = \frac{I_{SAT,acc}}{\sqrt{1 + \left(\frac{V_{R,SAT}}{V_R}\right)^2}}$$

After some simple calculation:

$$\begin{aligned} V_R &= \frac{V_{R,SAT} \cdot I_{acc}}{\sqrt{I_{acc}^2 - I_{SAT,acc}^2}} = \frac{V_{R,SAT}}{I_{SAT,acc}} \cdot \frac{I_{acc}}{\sqrt{1 - \left(\frac{I_{acc}}{I_{SAT,acc}}\right)^2}} \\ &= \frac{L_{acc} v_{S,acc}}{\mu_{0,acc} I_{SAT,acc}} \cdot \frac{I_{acc}}{\sqrt{1 - \left(\frac{I_{acc}}{I_{SAT,acc}}\right)^2}} \\ &= \frac{L_{acc}}{\mu_{0,acc} Q_{acc}} \cdot \frac{I_{acc}}{\sqrt{1 - \left(\frac{I_{acc}}{I_{SAT,acc}}\right)^2}} \end{aligned} \tag{2.44}$$

The access region resistance is obtained combining equation 2.42 and 2.44:

$$\begin{aligned} R_{D/S,acc} = \frac{V_R}{I_{acc}} &= \frac{L_{acc}}{\mu_{0,acc} Q_{acc}} \cdot \frac{1}{\sqrt{1 - \left(\frac{I_{SAT,acc}}{I_{acc}}\right)^2}} \\ &= \frac{L_{acc}}{\mu_{0,acc} W q n_{s,acc}} \cdot \frac{1}{\sqrt{1 - \left(\frac{I_{SAT,acc}}{I_{acc}}\right)^2}} \end{aligned} \tag{2.45}$$

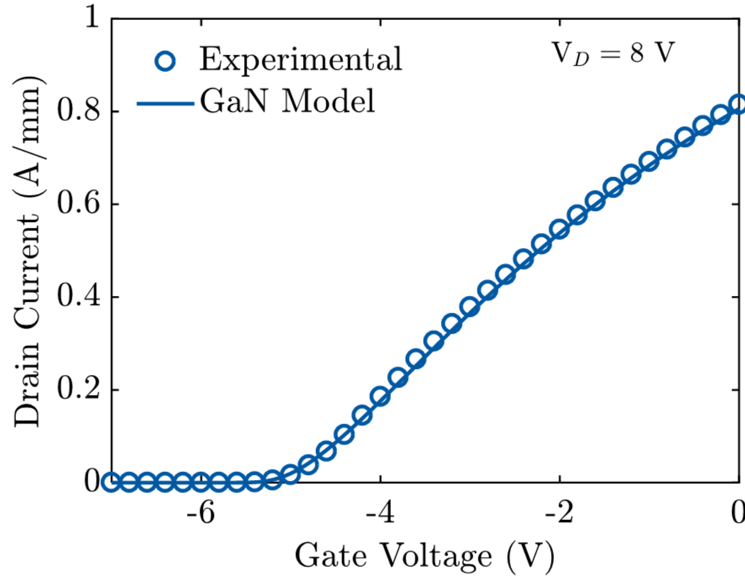

Figure 2.8: I_D-V_G simulation vs experimental data of Schottky HEMT with threshold voltage V_{TH} −4.9 V, length gate length L = 5 μm and width W = 10 μm. The simulation is performed implementing the Verilog-A code in the electronic design automation software Advanced Design System (ADS) by Keysight EEsof EDA.

2.4 Conclusion

A surface potential based model for GaN HEMT has been presented in this chapter including the core model and some of the main real device effects. The model has been implemented using Verilog-A code in the electronic design automation software Advanced Design System (ADS) by Keysight EEsof EDA. The simulation result is then compared with the measured I_D-V_D and I_D-V_G of a Schottky HEMT with threshold voltage V_{TH} −4.9 V, gate length L = 5 μm, width W = 10 μm, length gate-drain access region L_{GD} = 2.5 μm, length gate-source access region L_{GS} = 1.5 μm, thickness AlGaN t_{AlGaN} = 26 nm, percentage of aluminum Al_x = 20% showing excellent agreement (see figure 2.8 and 2.9). To perform the fitting with the experimental data, several parameters have to be extracted following an extraction strategy that will be introduced in Chapter 3 where the model has been used to support our understanding of the effects of cumulative γ-ray irradiation on AlGaN/GaN HEMTs.

In Chapter 4 the model has been modified including a highly doped p-GaN layer, proposing a novel approach to simulate the pGaN/AlGaN/GaN HEMT. This structure is becoming widely used in power electronic applications.

Finally in Chapter 5, using an approach similar to the one proposed to model the pGaN layer, we will present a novel approach to simulate a GaN HEMT with Negative Capacitance under the gate, showing that this structure can lead to an increase of the DC performance of the device.

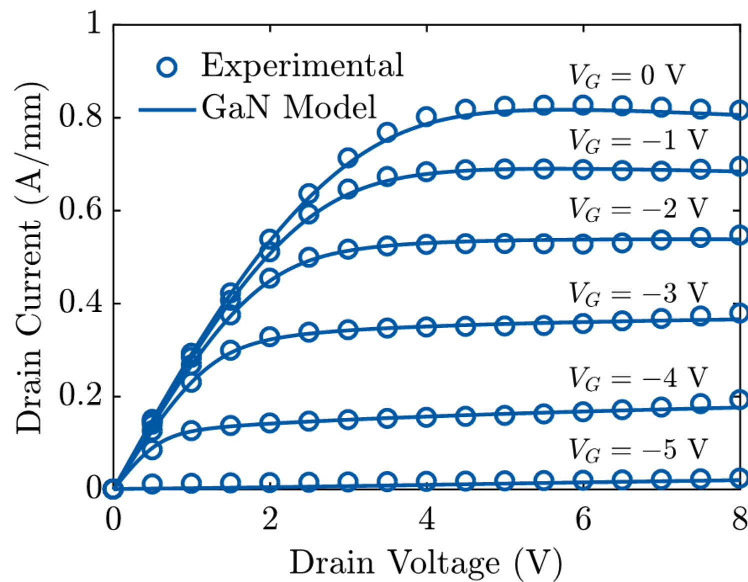

Figure 2.9: I_D-V_D simulation vs experimental data of Schottky HEMT with threshold voltage $V_{TH} - 4.9$ V, length gate length $L = 5$ μm and width $W = 10$ μm. The simulation is performed implementing the Verilog-A code in ADS.

Chapter 3

Understanding of γ-Ray Degradation in Schottky HEMT

3.1 Radiation Defects in GaN

Silicon-based semiconductor devices have dominated space applications for several decades but have now approached their theoretical limit [42]. Subsequently, space industries and research communities have shown interest in wide band-gap semiconductors, such as Gallium Nitride.

Gallium nitride not only shows superior electrical performances such as high current density, high mobility, and high breakdown voltage but also superior radiation hardness, making it an attractive material in radiation-harsh environment applications. For these reasons, many GaN-based devices are used in satellite and military systems, where radiation tolerance is critical [43]. The intrinsically high radiation resistance is the consequence of the strong bonding in binary and ternary nitrides. The stream of ionizing radiation at which GaN materials and devices such as transistors and light-emitting diodes start to show degradation is about two orders of magnitude higher than in their GaAs equivalents [44]. This difference is attributed to the more compact lattice structure of GaN.

A material's ability to resist high-energy radiation is inversely proportional to its crystal lattice constant, a. As we can see in Chapter 1, the lattice constant for GaN (a_{GaN} = 3.189 Å) is about 60% of the lattice constant of Si (a_{Si} = 5.431 Å) and GaAs (a_{GaAs} = 5.653 Å). It is expected, therefore, that the GaN-based electronics will be more stable when exposed to radiations [45]. The energy required to displace an atom from its position in the crystal lattice is denoted by E_d. This parameter has been measured in several semiconductors and empirically determined to be inversely proportional to the volume of the unit cell. From the known size of the GaN unit lattice, it suggests that the GaN is quite radiation hard [43]. Independent of this empirical method, it was deduced, by analyzing the transport properties of electron-irradiated GaN films, that the displacement energy for GaN is (19 ± 2) eV, which is much larger than 9.8 eV obtained for GaAs (see figure 3.1).

3.1.1 Displacement Damage

Displacement damage is the most important effect observed in irradiated GaN devices and is the result of nuclear interaction which cause lattice defects. Displace-

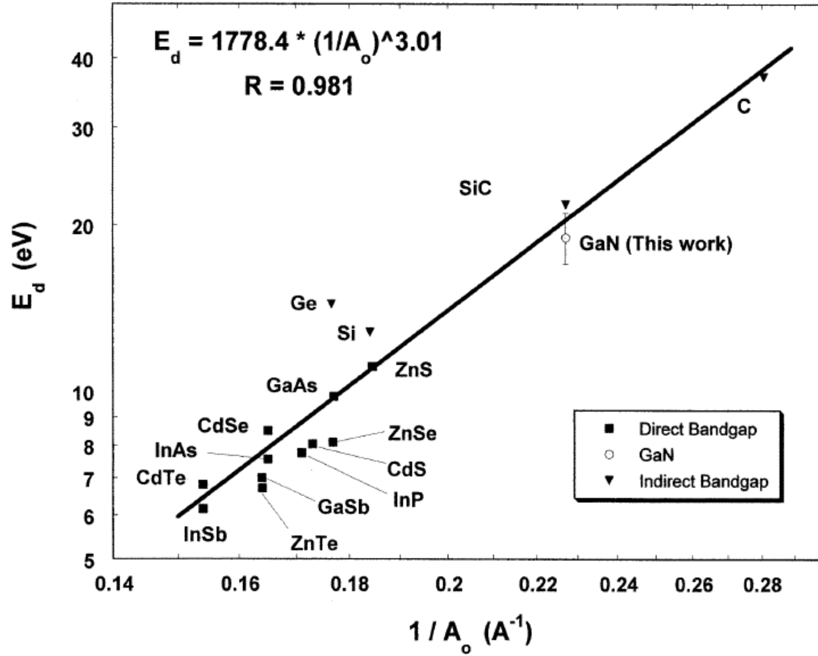

Figure 3.1: Empirical relationship between mean displacement energy E_d and inverse lattice parameter for various semiconductors [43]. GaN excels.

ment damage is due to cumulative long-term non-ionizing radiation damage in the GaN. The collisions between an incoming ion and a lattice atom displaces the atom from its original lattice position, leaving vacancies, interstitials and complexes of both, sometimes with impurities in the GaN [44]. If an energetic particle such as a neutron or proton collides with the nucleus of a lattice atom, the primary knock-on atom may be displaced from the lattice if the incident particle has sufficient energy ($E > E_d$). If a lattice atom is displaced, it may results in a stable defect or trap, which will affect the performance of the HEMT.

Although an atom may be knocked out of its lattice position by the incoming particle, the vacancy-interstitial pair may recombine; a phenomenon which depends on the temperature. In gallium nitride, some annealing thus occurs at room temperature giving it an high amorphization threshold. Depending on the distance between the vacancy and interstitial, two cases are distinguished [43]. If the distance is small, the two point defects are correlated and the recombination rate is proportional to the defect concentration; if it is large, they are not correlated and the recombination occurs through the diffusion of the defects, which is a random process.

The response of GaN to radiation damage is a function of radiation type, dose, energy as well as the carrier density, impurity content and dislocation density in the GaN. There are three main GaN-based heterostructures used for electronics, namely AlGaN/GaN, which is the most common nitride-based heterostructure; AlN/GaN which produces the highest two dimensional electron gas density, but has issues with stability of the AlN and finally, InAlN/GaN, an emerging system with high thermal and and chemical stability and lattice matching to GaN at an In mole fraction of 0.17 [44]. Given the applications for GaN HEMTs, they are commonly be subject to fluxes of high energy protons and electrons if used in low earth or-

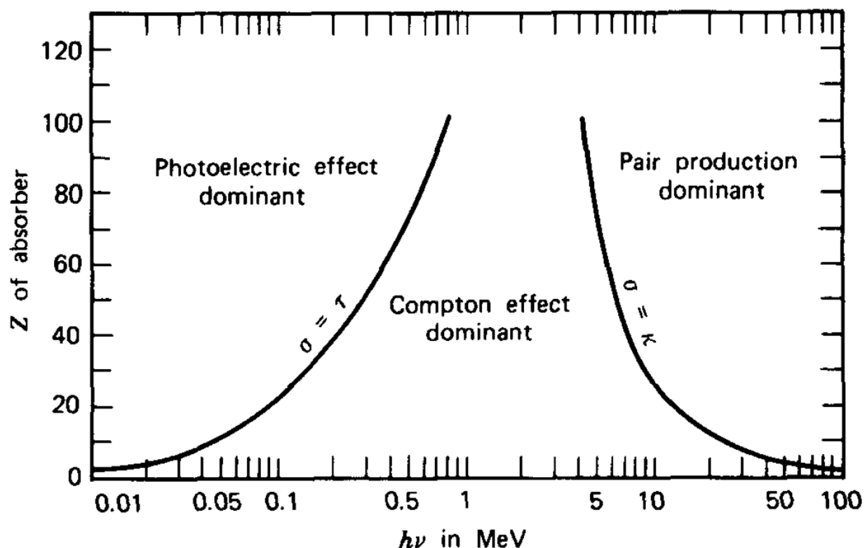

Figure 3.2: The relative importance of the three major types of γ-ray interaction. The lines show the value of Z (number of protons) and $h\nu$ (energy of the incident photons) for which the two neighboring effects are just equal [42].

bit satellites as well as neutrons or γ-rays if used in radiation-hard electronics for nuclear or military systems. Each of these forms of radiation produces different types of damage [46]. In general, proton and electron irradiation produce simple point defects in the nitride lattice [47], while neutron irradiation creates extended defects called Gossick zones, which are heavily disordered core regions surrounded by a space charge region with strong band bending [46].

Regarding γ-radiation, the response is quite complicated. Although a large number of possible interaction mechanisms are known for gamma rays, only three major types play an important role in radiation measurements: *Photoelectric Absorption*, *Compton Scattering*m and *Pair Production* [42].

All these processes lead to the partial or complete transfer of γ-ray photon energy to electron energy (see figure 3.3a,b,c). The relative importance of the three major types of γ-ray interaction is conveniently illustrated in figure 3.2. Three areas are defined on the plot within which photoelectric absorption, Compton scattering, and pair production each predominate. The next paragraphs summarize the mechanisms that characterize each effect using a primary reference in which the topic is exhaustively discussed [42].

Photoelectric Absorption: The photoelectric absorption process is a low-energy phenomena in which the incident photon interact with an absorbed atom, where the energy of the photon is completely absorbed by an electron bounded with the atom (valence band). This interaction cannot take place with an electron in the conduction band and, in the process, the energy of the incident γ-ray has to be higher than the work function of the material. The result is that the electron is ejected by the atom. The photoelectron appears with an energy given by:

$$E_{e^-} = h\nu - E_b \tag{3.1}$$

where E_b represent the energy lost to unbind the electron from the atom. In addition to the photoelectron, the interaction creates a hole in the shell of the atom.

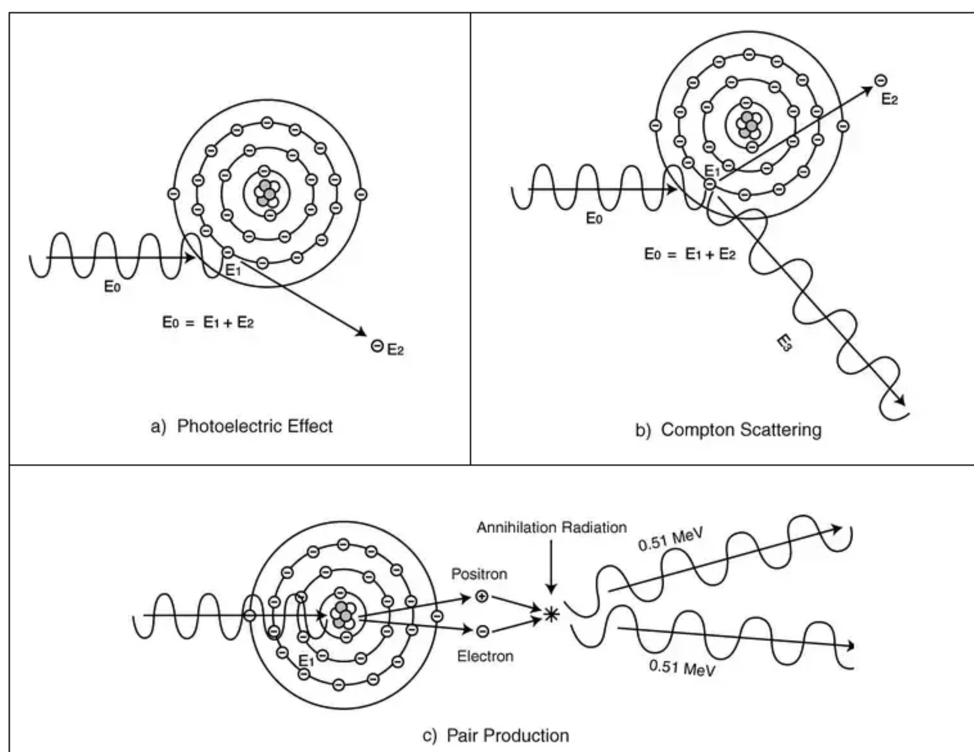

Figure 3.3: Three major types of γ-ray interaction with the incident atom.

This vacancy is quickly filled through capture of a free electron from the medium or rearrangement of electrons from other shells of the atom. Since the lifetime of the hole is almost negligible, the photoelectric absorption is characterized only by the ejection of an electron (see figure 3.3a).

Compton Scattering: The interaction process that leads to Compton scattering is a mid-energy phenomena which takes place between the incident γ-ray photon and an electron in the absorbing material. This is often the most predominant interaction mechanism. In Compton scattering, the photon transfers a portion of its energy to the electron which is known as *recoil electron* and is then deflected through an angle θ with respect to its original direction. The higher the transferred energy from the photon to the electron, the higher the reflection angle θ. The probability that this type of interaction occurs depends on the number of electrons available as scattering targets and therefore, as we can see in figure 3.2, it increases linearly with Z. The Compton scattering is characterized by the generation of an electron and a photon (see figure 3.3b).

Pair Production: The pair production process is an high-energy phenomena only possible in case the γ-ray energy exceeds twice the rest-mass energy of an electron (1.02 MeV). As a practical matter, the probability of this interaction remains very low unless the γ-ray energy approaches several MeV. In the interaction, the incident photon disappears and is replaced by an electron-hole pair (see figure 3.3c). No single expression exist for the probability of pair production per nucleus, but its magnitude increases approximately with quadratic dependence with the increase of the absorber atomic number.

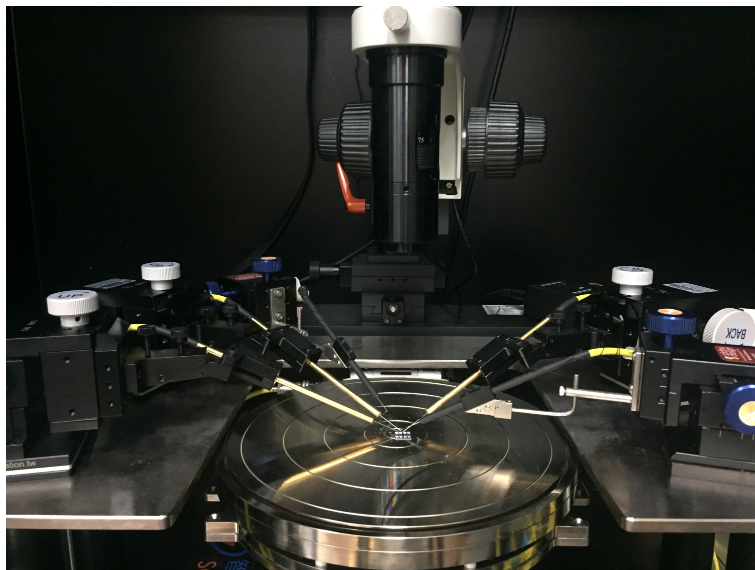

Figure 3.4: Keysight B1500A semiconductor device analyzer used to perform the measurement.

Previous reports of the effects of γ-ray irradiation on GaN devices exhibited some conflicting results. Some studies claim that the defects produced by gamma irradiation can improve the device performance such as increasing drain saturation current [48]. In contrast, others reported the drain current was reduced about 60% after high dosed of irradiation (around 7×10^4 rad) [49]. In some cases, low dose γ-irradiation leads to a partial relaxation of the elastic strain in AlGaN/GaN heterostructures and enhances the electron mobility by 5-10%. Furthermore, the increase in the saturation current is believed to be due to the knock-on of nitrogen atoms. This displacement creates nitrogen vacancies which act as donors and increase the effective channel doping and thus the drain current [44]. In general, GaN-based HEMTs irradiated with γ-rays exhibit shifts in drain current (I_D), threshold voltage (V_{TH}), transconductance (g_m), and gate leakage current (I_G). However, although these effects have been broadly explored [48, 45, 50, 51], the main reasons for the shifts in characteristics remain inconclusive. In addition, the comparison among irradiation effects due to cumulative and single γ-ray dose remains unexplored. This chapter is structured in two parts: (i) The first part is dedicated to the experimental part, studying the effects of γ-ray in four different power Metal Insulator Semiconductor (MIS)-HEMT with different irradiation doses; (ii) the second part is dedicated to the modeling, in order to understand the origin of the instability by comparing simulation results with experimental data.

3.2 γ-Ray Degradation in MIS-HEMT

In this study, we systematically irradiate GaN-on-Si Power MIS-HEMTs in four different γ-ray dose regimes. The device electrical parameters chosen to compare the electrical reliability of the MIS-HEMT device after the irradiation doses are: I_D, V_{TH}, and I_G. Subsequently, X-Ray Photoelectric Spectroscopy (XPS), Scanning Electron Microscopy (SEM) and Energy Dispersive X-Ray (EDX) are performed to further analyze the γ-ray induced degradation.

3.2.1 Experiment Details

The experiment is conducted on a typical AlGaN/GaN MIS-HEMT, fabricated on a 6-inch Si wafer. The devices feature a 5 μm gate length, 100 μm width, 20 μm drain-gate length, 3 μm source-gate length, 26 nm $Al_{0.2}Ga_{0.8}N$ barrier, 30 nm SiN gate dielectric, a passivation layer combining SiN and SiO_2 dielectrics, and an Al-based pad metalization. The devices have a threshold voltage $V_{TH} = -10$ V. Four identical samples are selected with different γ-ray dose regimes (see table 3.1), and each samples further consists of four devices. The irradiation is done with a ^{60}Co source of photon energy 1.33 MeV at room temperature. The radiation room has a cylindrical chamber of 10.6 cm diameter and 14.2 cm height with 8 needles of ^{60}Co source for uniform irradiation. The maximum ^{60}Co source capacity is 185 TBq where the becquerel (Bq) is defined as the activity of a quantity of radioactive material in which one nucleus decays per second and is therefore equivalent to an inverse second, s^{-1}. During the pristine stage and after each irradiation regimes, the devices are measured through Keysight B1500A semiconductor device analyzer (see figure 3.4).

3.2.2 Experiment Results and Discussion

Figure 3.5 shows the comparison of transfer characteristic (I_D-V_G) during the pristine stage and after each γ-ray irradiation dose in all samples. An increase of the drain current and a threshold voltage shift are observed in all the samples after cumulative γ-ray irradiation. The change is more significant after the first irradiation dose, and saturates toward the higher irradiation doses. Table 3.2 summarize the quantitative increase in I_D after each γ-ray dose. We can see that, in comparison to the pristine stage, after 5 kGy γ-ray dose, Sample 1 exhibits a 13% increase in the drain current. For Sample 2, this increase after the same dose, decreases slightly to 12%. The improvement in I_D decreases further to 8% in Sample 3. A similar trend is found after 10 kGy γ-ray dose, since, Sample 3 shows an increase in the drain current up to 12% while Sample 4 reach just a 4%. This demonstrates that the improvement in I_D is larger when the device is irradiated through small incremental cumulative irradiation doses than with significant incremental cumulative γ-ray doses.

Irradiation	Sample 1	Sample 2	Sample 3	Sample 4
	Pristine	Pristine	Pristine	Pristine
γ-Ray Dose (kGy)	1	1	1	1
	2	3	5	10
	3	5	10	20
	4	-	-	-
	5	-	-	-

Table 3.1: γ-ray dose regime for 4 identical samples. Note that each sample consists of 5 devices.

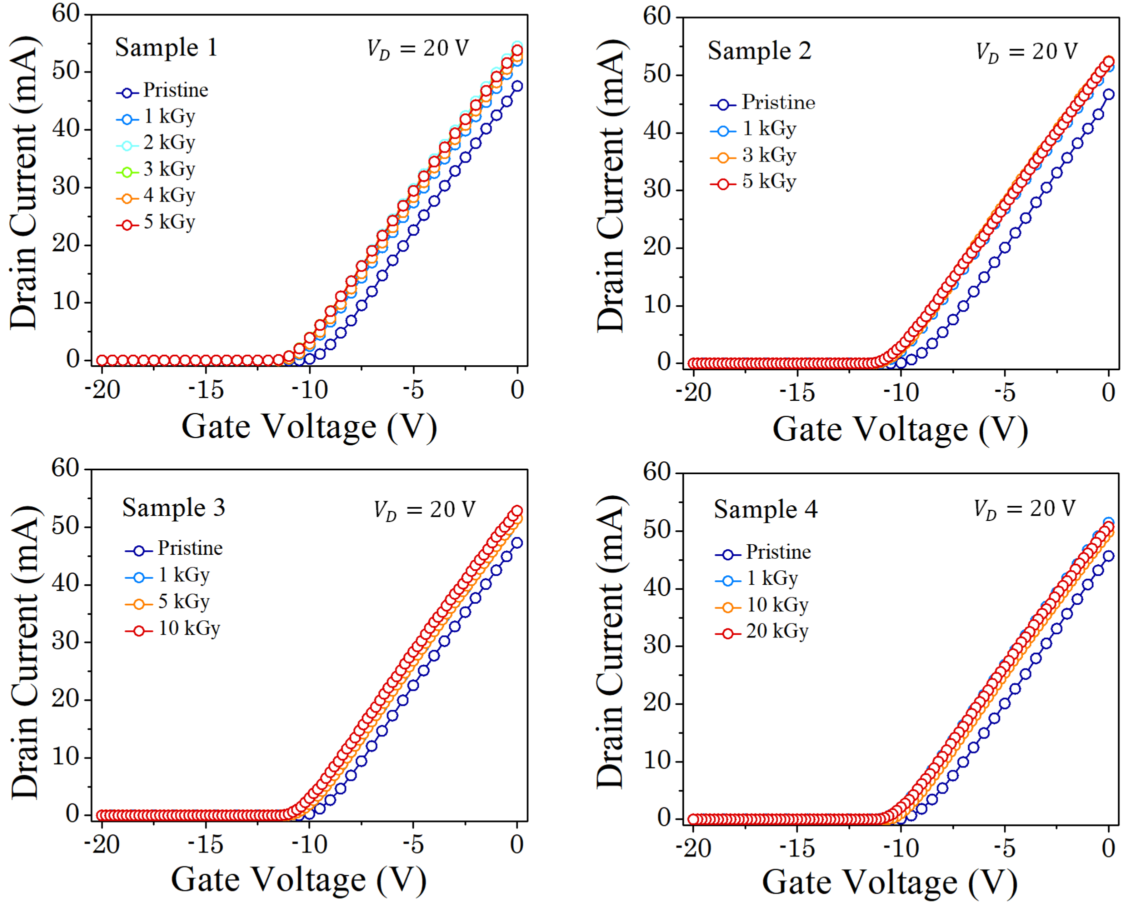

Figure 3.5: Measured I_D-V_G in all four samples after various γ-ray doses.

γ-Ray	Sample 1	Sample 2	Sample 3	Sample 4
(kGy)	(mA)	(mA)	(mA)	(mA)
Pristine	47.6	46.7	47.3	47.9
1	51.2	51.5	52.0	51.9
2	54.5	-	-	-
3	53.5	52.5	-	-
4	53.0	-	-	-
5	54.0	52.4	51.5	-
10	-	-	53.0	49.8
20	-	-	-	50.7
Increase 5 kGy	13%	12%	8%	-
Increase 10 kGy	-	-	12%	4%

Table 3.2: Comparison of I_D at $V_G = 0$ V and $V_D = 20$ V after each γ-ray dose.

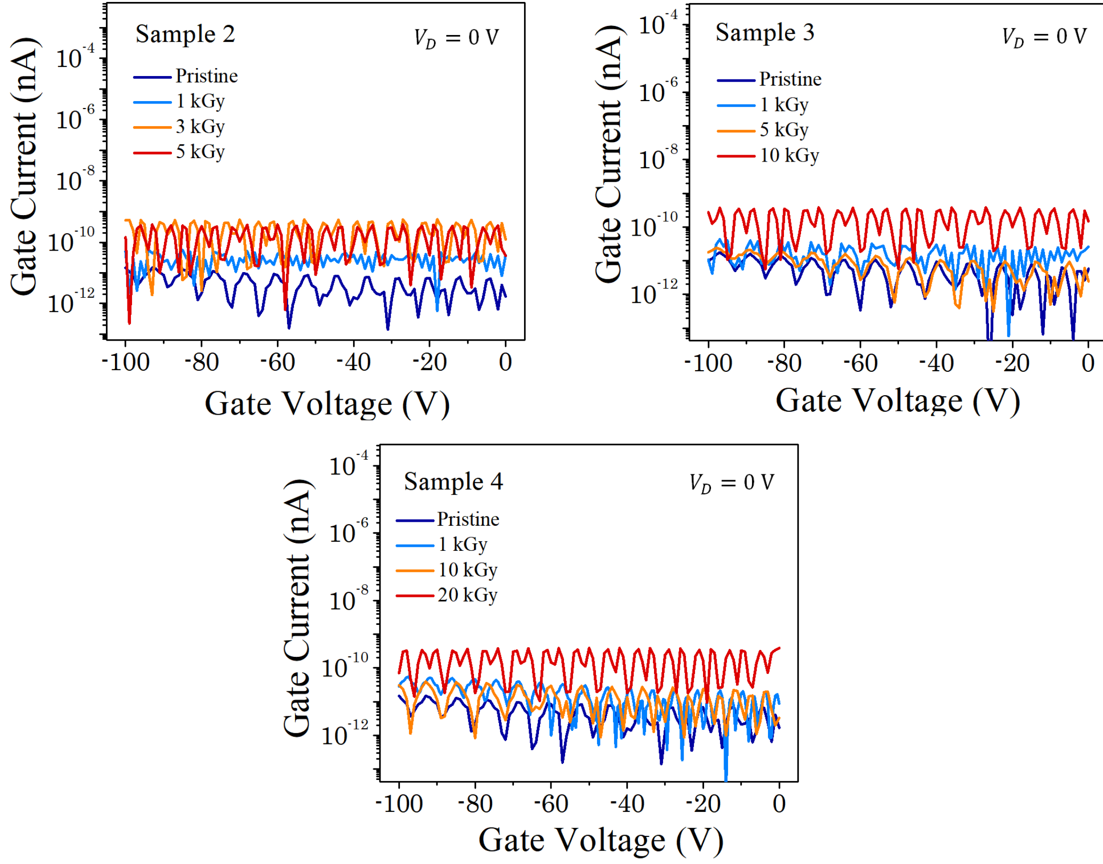

Figure 3.6: Measured I_G-V_G in Sample 2, 3, and 4 after various γ-ray doses.

Previous investigations report different reasons for the improvement in current after γ-irradiation on GaN devices. Some of these point to an increase in the carrier concentration (n_s) in the channel [50], improvement in mobility (μ) [52], generation and annihilation of point defects in terms of nitrogen vacancies (V_N) that act as donor or acceptors [45] and an improvement in the AlGaN/GaN interface due to trap redistribution and modification of existing native defect structures [53]. In an ideal HEMT transistor, the shift in V_{TH} is associated with variation in the sheet density of the total charge σ ($\Delta V_{TH} = \Delta\sigma d/\varepsilon$).

Since the increase in I_D is also associated with shifts in V_{TH} in our case, therefore the dominating reason for improvements in current is the increase in the 2DEG charge density. An increase in n_s can be anticipated due to the creation of nitrogen vacancies (V_N that act as donor) [45]. To confirm the creation of nitrogen vacancies after irradiation, XPS analysis is performed on AlGaN/GaN epi-layer structures during the pristine stage and after 1 kGy of γ-irradiation at the Department of physics, Indian Institute of Technology (IIT) Delhi-India. The XPS system at IIT Delhi is from Omicron Nanotechnology, Germany. It consist of a monochromatic source of energy 1486 eV and a detector of resolution 0.6 eV. The system is calibrated using the carbon (C) peak of energy 285.4 eV. The data analysis post XPS characterization has been carried out using XPSPEAK41 software that uses a standard peak de-convolution method. XPS is used to characterize the chemical composition of Al 2p, Ga 3d, O 1s and N 1s (where the first term is the chemical component and the second term is used to define the outer most shell in each element).

Element	Wt. %	At. %
C	1.51	9.76
O	**6.16**	**29.84**
F	1.24	5.06
Al	**21.10**	**60.61**
Ti	-3.15	-5.10
Ni	-0.14	-0.19
Au	0.05	0.02

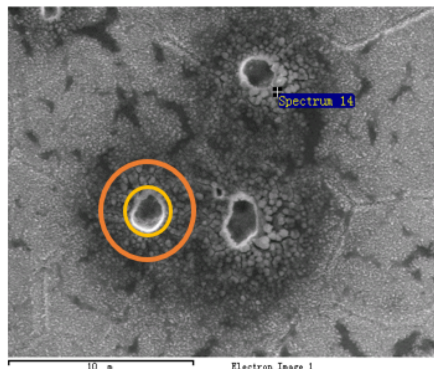

(a)

Element	Wt. %	At. %
C	2.68	15.36
O	**12.56**	**54.00**
F	3.68	13.34
Al	**7.12**	**18.16**
Cl	0.38	0.73
Ti	-1.04	-1.49
Ni	-0.10	-0.12
Au	0.02	0.01

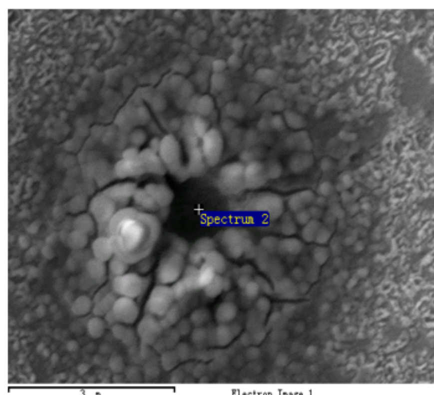

(b)

Figure 3.7: Device pad SEM image after 5 kGy γ-irradiation, showing the creation of small cavities. In the figure is highlighted with a yellow circle the inner cavity and orange the periphery. The table contains the atomic percentage of the elements characterized by EDAX analysis.

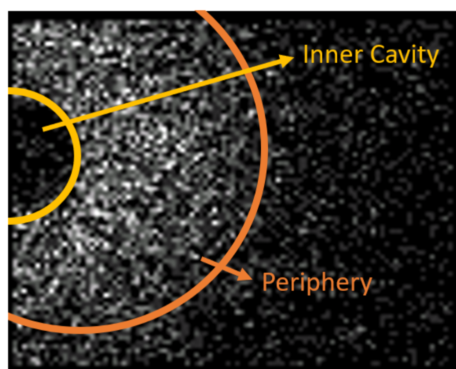

(a)

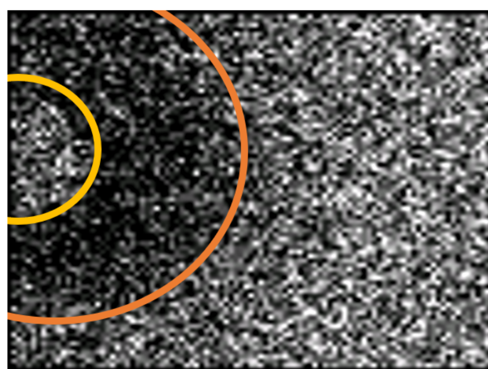

(b)

Figure 3.8: Elemental distribution showing the formation of Aluminum oxide. (a) Shows the distribution of aluminum. The concentration decreases significantly in the periphery of the cavity. (b) Shows the distribution of Oxygen. The concentration is higher in the periphery of the cavity confirming the formation of AlO_x

As no change has been found in the composition of Ga 3d whereas the composition of N 1s is decreased post 1 kGy γ-irradiation in observation, it highlights the creation of nitrogen vacancies after radiation. Simultaneously, by the spectrum of O 1s and Al 2p, annealing at the surface has been confirmed. The detailed discussion about our XPS results can be found in our publication [54]. Figure 3.6 shows the leakage current behaviour with an applied reverse gate bias voltage (V_G), during pristine stage and after each radiation in Samples 2, 3, and 4. It is found that, with the increase of the radiation dose, there is a monotonic increasing in noise in all the samples. For example in Sample 2, the noise is higher after 5 kGy of radiation dose as compared to at 3 kGy and 1 kGy. Similarly in case of Sample 3 the noise is higher post 10 kGy compared to the previous doses of radiation. Finally, the same trend is observed in case of Sample 4. Post 5 kGy of radiation, small cavities has been confirmed on the contact pads of the devices by SEM imaging in all three samples. Furthermore, EDX analysis has been performed around these small cavities. It is found that the aluminum percentage has been reduced around the periphery of these small cavities from 61% Al composition inside the cavity to 18% on its periphery as shown in figure 3.7. The elemental mapping in EDAX analysis confirms the formation of AlO_x as we can see in figure 3.8 and in the table of figure 3.7.

3.3 γ-Ray Degradation in Schottky HEMT

In this section, we will demonstrate that the physics-based GaN model presented in Chapter 2 can facilitate the analysis of the effects of the γ-ray induced degradation and be used to understand the origin of the instability by comparing simulation results with experimental data of the fabricated AlGaN/GaN HEMT subjected to cumulative γ-ray dose. Meanwhile, the parameters extracted from the modeling part, such as mobility and contact resistance are also verified simultaneously with experimentally measured values carried out using a dedicated Hall measurement and Circular Transmission Line Measurement (C-TLM).

3.3.1 Device Fabrication and Experimental Results

The Schottky AlGaN/GaN HEMTs are fabricated at Indian Institute of Technology (IIT) Delhi-India in a dedicated fabrication facility. AlGaN/GaN epi-layers stacks are fabricated using Metal Oxide Chemical Vapor Deposition (MOCVD) technique. Ti/Al/Ni/Au stack is used for ohmic contact formation whereas Ni/Au is used for the Schottky contact formation. The gate length is $L = 0.8$ μm, whereas the width is $W = 100$ μm. SiN of thickness 1000 Å has been used as a final passivation for the device. The γ-radiation is performed using a ^{60}Co source with photon energy 1.33 MeV and 1.17 MeV at room temperature. Four doses of γ-ray are given cumulatively in the order of 1 kGy, 9 kGy, 20 kGy and 30 kGy. Figure 3.9 shows the measured I_D-V_G characteristic subjected to different cumulative γ-ray radiations. In this case we observe an increase in drain current (I_D) with no change in the threshold voltage (V_{TH}) after irradiating the Schottky HEMT devices.

In addition, a dedicated structures for Hall measurements and circular line measurements (C-TLM) are fabricated to investigate the shifts in carrier concentration (n_s), mobility (μ), contact resistance (R_C) and sheet resistance (R_{sh}). In table 3.3 we can see that the extracted 2DEG density remains almost the same while the

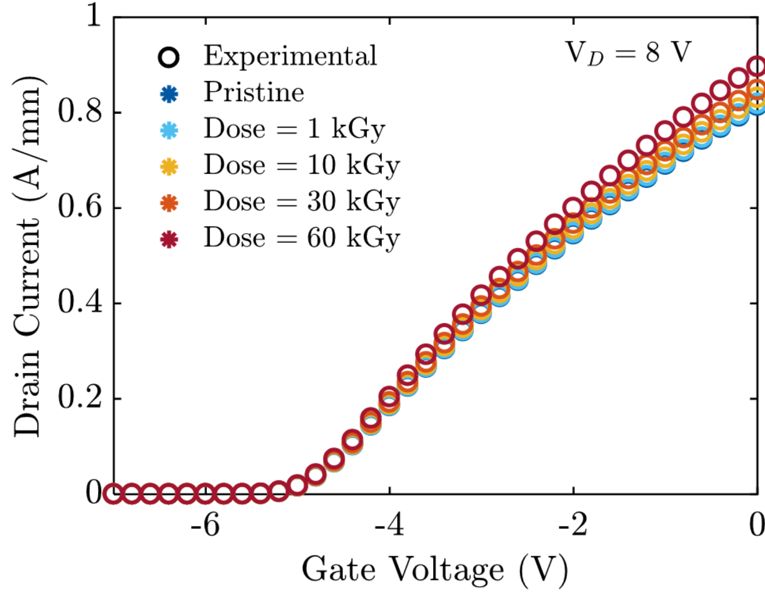

Figure 3.9: Measured I_D-V_G characteristic subjected to cumulative γ-ray radiations.

mobility presents a significant increase. The physical discussion leading to an increase of the mobility has been reported earlier, such as the decrease of the active defects/traps [53], increase in the diffusion length of the minority carrier [45], and relaxation in the elastic strain and structural-impurity reordering [52]. Furthermore, the extracted R_C and R_{sh} exhibit a decrease with the increase of the radiation dose. The decrease in the contact resistance can be explained by the annealing effect due to the localized rising temperature [48] while the sheet resistance is inversely proportional to the increasing mobility.

Despite the experimental data obtained from dedicated Hall measurement and C-TLM indicate an increase in the mobility and a decrease in the contact and sheet resistance, it is difficult to precisely indicate the main root cause of the increase in the drain current, because all the extracted parameters in table 3.3 are possibly leading to this increase. In order to clarify the main root cause, the physics-based

γ-Ray	n_s	μ	R_C	R_{sh}
(kGy)	$\times 10^{12}$ (cm^{-2})	(cm^2/Vs)	(Ω)	($\Omega/\square$)
Pristine	7.5	1590	2.18	482
1	7.7	1603	2.14	478
10	7.5	1670	1.98	461
30	7.7	1715	1.52	428
60	7.9	1875	1.15	375

Table 3.3: Carrier concentration and mobility from Hall Measurement, contact resistance and sheet resistance from C-TLM

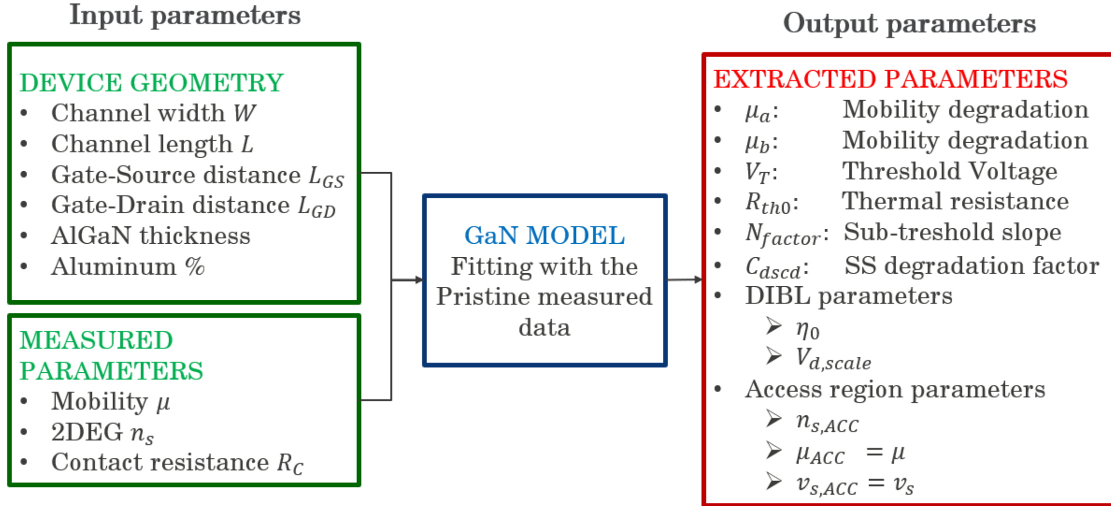

Figure 3.10: Input output parameters in used to calibrate the model with the pristine case and with the experimental data coming from the Hall measurement and C-TLM. The saturation velocity under the gate region (v_S) and access region ($v_{S,acc}$) are supposed to be identical and equal to 1.05×10^7 cm/s. The same assumption is made for the mobility which is always the same along channel and access region and equal to the value determined experimentally by Hall measurement.

GaN model presented in Chapter 2 is used implementing the Verilog-A code in the electronic design automation software Advanced Design System (ADS) by Keysight EEsof EDA. The parameters extraction strategy that was used will be explained in the next section.

3.3.2 Parameter Extraction Strategy

In this section, we turn our focus on the extraction strategy used in order to extract the parameters for the device under study. It is important to emphasize that the following extraction method was used throughout the thesis every time a simulation result is fitted to the experimental data. Figure 3.11 has the intermediate plots during the extraction of the main parameters which are identified by tuning the simulation with the experimental data.

The fitting starts with 3.11a, where the threshold voltage is extracted from the I_D-V_G in linear scale. Then the mobility is extracted using at the same time I_D-V_G in linear scale and the transconductance plotted in figure 3.11e. The next step is the extraction of the n_{factor} which defines the sub-threshold slope and I_{G0} which is an empirical parameter used to describe the gate leakage. This is done from the I_D-V_G in log scale (see figure 3.11b). To facilitate the extraction we supposed $\mu_{acc} = \mu_0$ and $v_{S,acc} = v_S$. With this simplification $n_{s,acc}$, R_C, and v_S is are defined fitting the simulation result with the measured I_D-V_G. In figure 3.11c we can see the effect introduced by this parameters in increasing the ON resistance and the saturation current. Finally the self-heating effect is taken into account tuning the parameter R_{TH} (see figure 3.11d). The quality of the parameter extraction is usually evaluated by the fitting of the transconductance and drain conductance. In figure 3.11e and f we can see that the simulation shows excellent agreement with the experimental data.

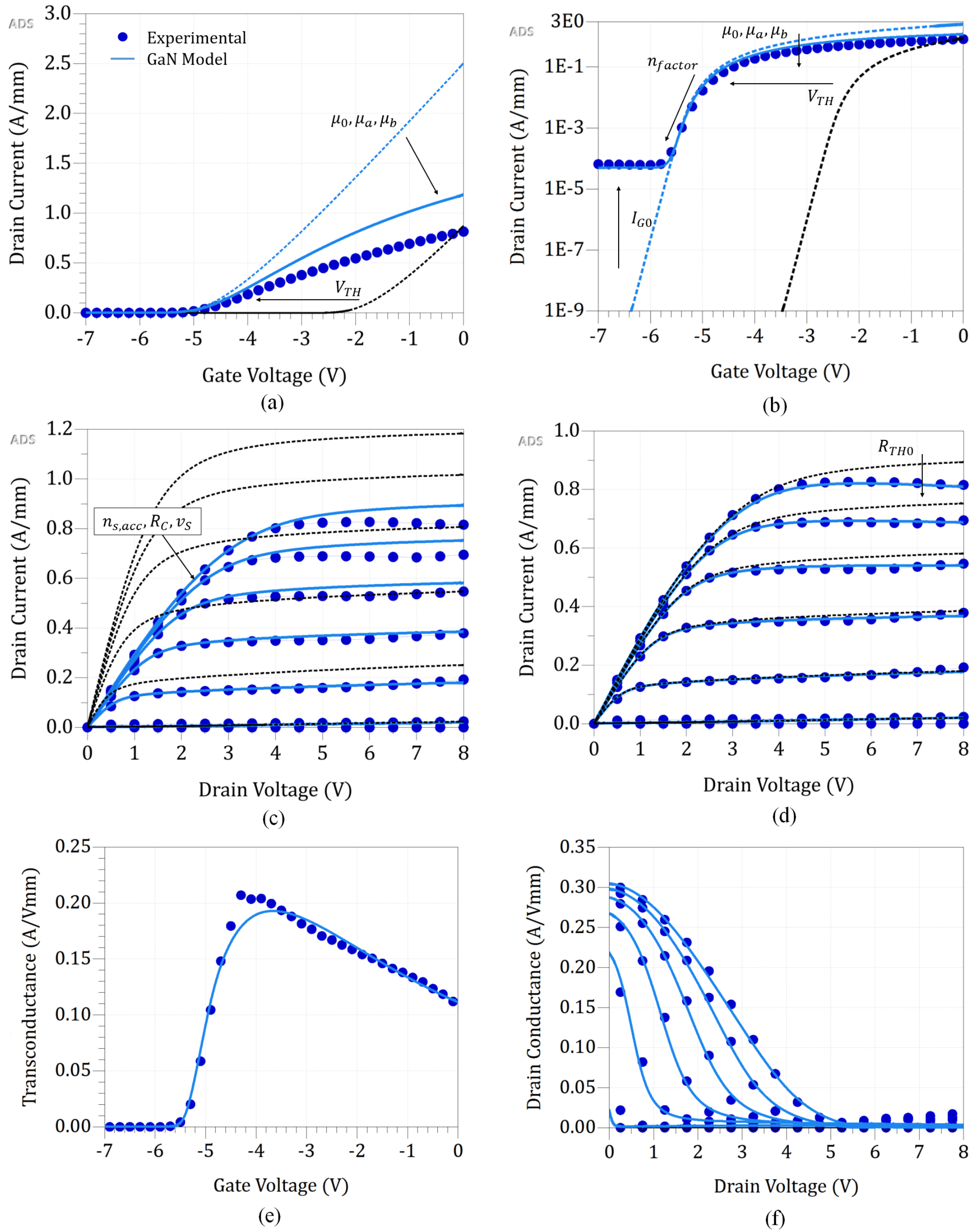

Figure 3.11: Step by step DC parameter extraction strategy tuning the simulation performed using ADS with the measured I_D-V_G and I_D-V_D. In the figures is shown how to extract the main parameters starting from threshold voltage identification from I_D-V_G.

The measurement fitted in figure 3.11 is the I_D-V_G and I_D-V_D of the Schottky HEMT fabricated to study the effects of γ-ray radiation n GaN-based HEMT devices. Now that the model is well calibrated with the pristine case of the real device, the next step is to use the GaN model to facilitate the analysis of the effects of the γ-ray induced degradation and to understand the origin of the instability using as input the experimental data coming from the Hall measurement and C-TLM of the fabricated AlGaN/GaN HEMT subjected to cumulative γ-ray dose.

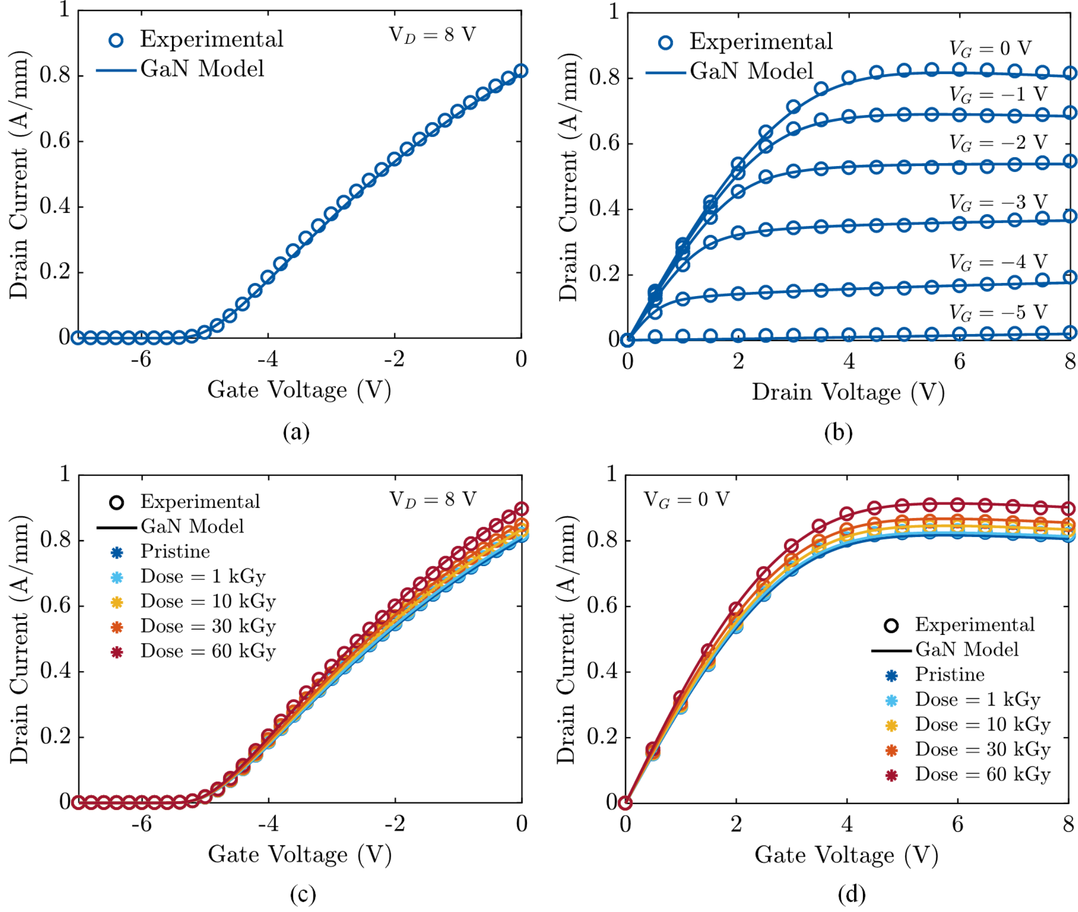

Figure 3.12: I_D-V_G and I_D-V_D before radiation (pristine case) and for each radiation dose. The simulation shows excellent agreement with the experimental data. The GaN model can follow the change in the mobility and contact resistance due to the cumulative γ-irradiation. For this reason the GaN model can give us an insight of the contribution of each parameters in the increase of the drain current.

Extracted Parameter		Value
V_{TH}	Threshold Voltage	-4.9 (V)
n_{factor}	SS Factor	0.5
$C_{d,scd}$	SS Degradation Factor	0.15
μ_a	1st Order μ_0 Degradation	11×10^{-9}
μ_b	2st Order μ_0 Degradation	0
$V_{d,scale}$	DIBL Parameter	7
η_0	DIBL Parameter	0.035
R_{TH0}	Thermal Resistance	350 (K/W)
λ	Channel Length Modulation	1×10^{-3}

Table 3.4: Output parameters based on the fitted curve in the fresh device.

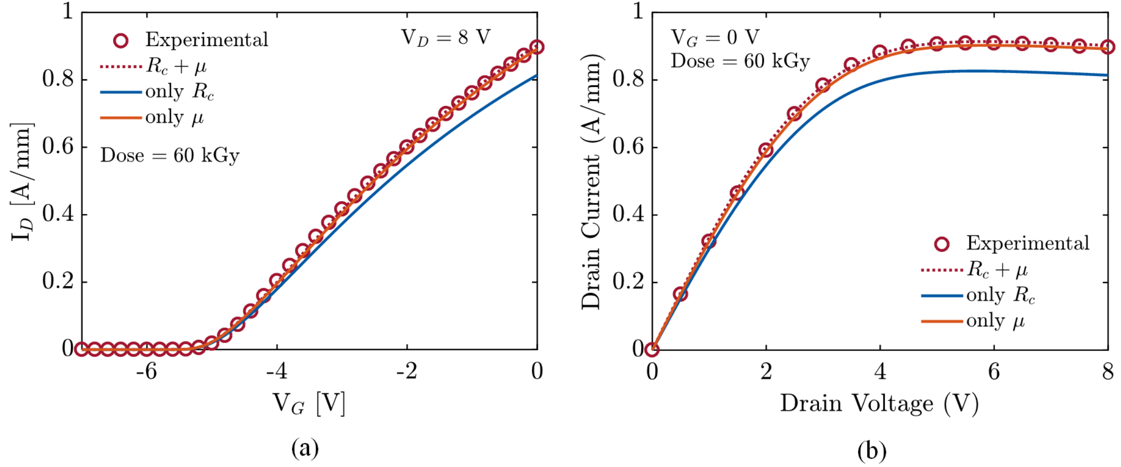

Figure 3.13: Fitted I_D-V_G and I_D-V_D characteristics tuning only the mobility and the contact resistance to identify which one is the leading factor in the origin of the instability.

3.3.3 Understanding of γ-Ray Degradation using GaN Model

In order to further clarify the main cause of the increase of the drain current in the radiated device, the physic-based GaN model is used following the methodology shown in figure 3.10. First of all, by using the charge density and mobility from Hall measurement and the contact resistance from the C-TLM (see table 3.3) the pristine case can be fitted and the output parameters can be extracted. The result of this procedure is resumed in table 3.4. Furthermore, the GaN model calibrated with the output parameters is used to fit the experimental characteristics in the devices under different radiation doses. The simulation has been fitted for all the measured gate bias in 4 identical samples showing always excellent agreement with the experimental data. Figure 3.12 shows the comparison of the experimental and fitted I_D-V_G and I_D-V_D before radiation (pristine case) and for each radiation dose. In order to further understand the main cause resulting in I_D increase, the I_D-V_G and I_D-V_D characteristics are simulated considering that only the μ is changing with the increase of the irradiation dose (R_C is fixed) or R_C is changing with the increase of the irradiation dose (μ is fixed). As compared to the experimental curve, it is clearly noticeable that the fitted I_D-V_G and I_D-V_D obtained by only considering the contact resistance as fitting parameter, shows a larger deviation compared to the fitted I_D-V_G and I_D-V_D obtained by only considering the the mobility as fitting parameter (see figure 3.13). This support the conclusion that the main degraded factor leading to the increase of the drain current is the increase of the mobility.

3.4 Conclusion

In this chapter, the degradation in GaN-based HEMTs due to γ-radiation has been extensively studied. The chapter face up the problem of understanding the effect of this degradation using two approaches. From the experimental point of view, the analysis is carried out involving I-V characterization, C-TLM characterization and

material characterization such as Hall measurement, EDAX and XPS analysis. In the second part the GaN model developed in the previous chapter is used to help our understanding of the measurement results and point the leading factor in the degradation due to γ-radiation in the fabricated AlGaN/GaN Schottky HEMTs.

Chapter 4

Modeling of E-Mode GaN HEMT

4.1 Working Principle

As introduced in Chapter 1, GaN-based HEMTs are receiving significant attentions for high power, high frequency, and high efficiency power switching applications due to the advantage of GaN over the conventional silicon and to the possibility of manufacturing these devices at a comparable or lower cost than their aging Si-based competitors [55].

Despite the exceptional properties of GaN HEMTs, the inherent 2DEG not only provides a high mobility in the channel but also leads to an intrinsic normally-on characteristic. In practical power switching applications, enhancement-mode (E-mode) devices with positive threshold voltage (V_{TH}) are preferred compared to depletion-mode (D-mode) devices for consideration of fail-safe and simplifying the gate drive topology [56]. In the last years, different approaches, designed to fabricate normally-off HETMs, have been proposed [57], each one with different advantages/disadvantages:

(i) **Fluorine Implantation:** in the early stages, fluorine plasma ion implantation into the AlGaN or GaN gate region to deplete the channel showed good results. The main problem is that the stability of the threshold voltage strongly depends on the optimization of the implantation process [58].

(ii) **MIS/MOS-HEMTs with Recessed Gate:** in this case, the AlGaN layer is partially removed to contact the insulator with the GaN and reduce the electron concentration in the channel increasing the threshold voltage. However this method is sensitive to trapping-related degradation mechanisms, caused by defects at the GaN/insulator interface and/or in the bulk insulator, which under stress conditions can affect the shift of the threshold voltage [59].

(iii) **p-(Al)GaN/AlGaN/GaN:** characterized by a layer of (Al)GaN, doped with acceptor atoms such as magnesium (Mg), between the gate and the barrier layer, which causes the band diagram to rise from the gate side pulling the conduction band in the channel up and, consequently, opposing the formation of the 2DEG. However, p-types are characterized by long-term degradation and the difficulty related to its doping [56].

To date, the normally-off p-GaN solution seems to represent a promising technology because of the good trade-off between reliability and cost and is now available from

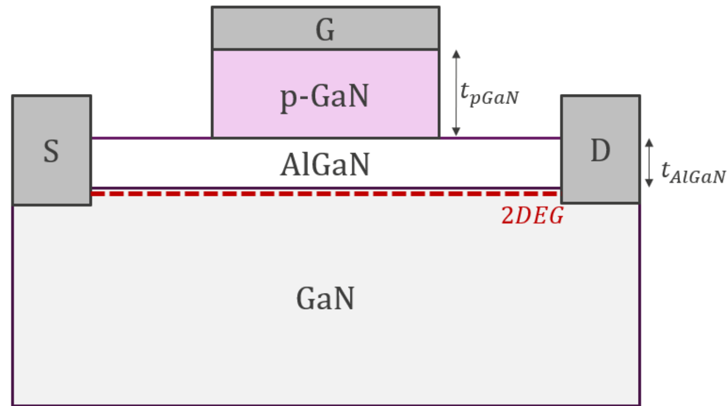

Figure 4.1: p-GaN/AlGaN/GaN HEMT structure discussed in this chapter where the p-GaN material is deposited under the gate of a Schottky HEMT device.

a broad range of suppliers [60]. In this type of structure, a Schottky contact is established between the top metal layer and the p-type semiconductor. However, relatively few data on the effect of the Schottky contact under the gate are available in literature [61].

To understand the phenomenological behavior of the gate vertical voltage drop in p-GaN HEMT, different models have been proposed [62, 63, 55, 56, 61]. These simplified analytical models always consider the gate as two back diodes. The top diode comes from the Schottky junction, while the bottom diode is similar to a PiN diode with the AlGaN acting as the "insulator" and the 2DEG as n-type semiconductor. The main limit of this approach is that the model of the equivalent circuit of the gate structure is made by only two back diodes, whose behavior is complicated to predict and varies depending on the bias, as reported by A. Stockman *et al.* [63] and N. Xu *et al.* [56]. This solution is not optimal and does not take into account the Schrödinger's and Poisson's equations that should be solved in order to have a precise understanding of what is happening in each layer under the gate.

Following the approach presented by T. L. Wu *et al.* [61], which investigates the p-GaN/AlGAN/GaN structure starting from its Capacitance-Voltage (C-V) characteristics, we propose a novel solution to understand the p-GaN HEMT using a physical-based model that defines the vertical voltage drop in the structure by solving the Schrödinger's and Poisson's equations. The developed model is implemented in the GaN model presented in Chapter 2 and is verified comparing the simulation results with the experimental data measured from four samples. The results give an unprecedented insight of the effect of the p-layer in the device; analyzing the gate capacitance, the thickness of the depletion region, the electric field and the vertical voltage drop in each layer under the gate.

4.2 Modeling the p-GaN HEMT

In order to understand the p-GaN/AlGaN/GaN structure (see figure 4.1), it is important to give a clear definition of the voltage drop in each layer of the structure. Figure 4.2 shows a detailed typical cross section of the device along with the energy-band diagram simulated using Synopsis' TCAD software where the Poisson's equa-

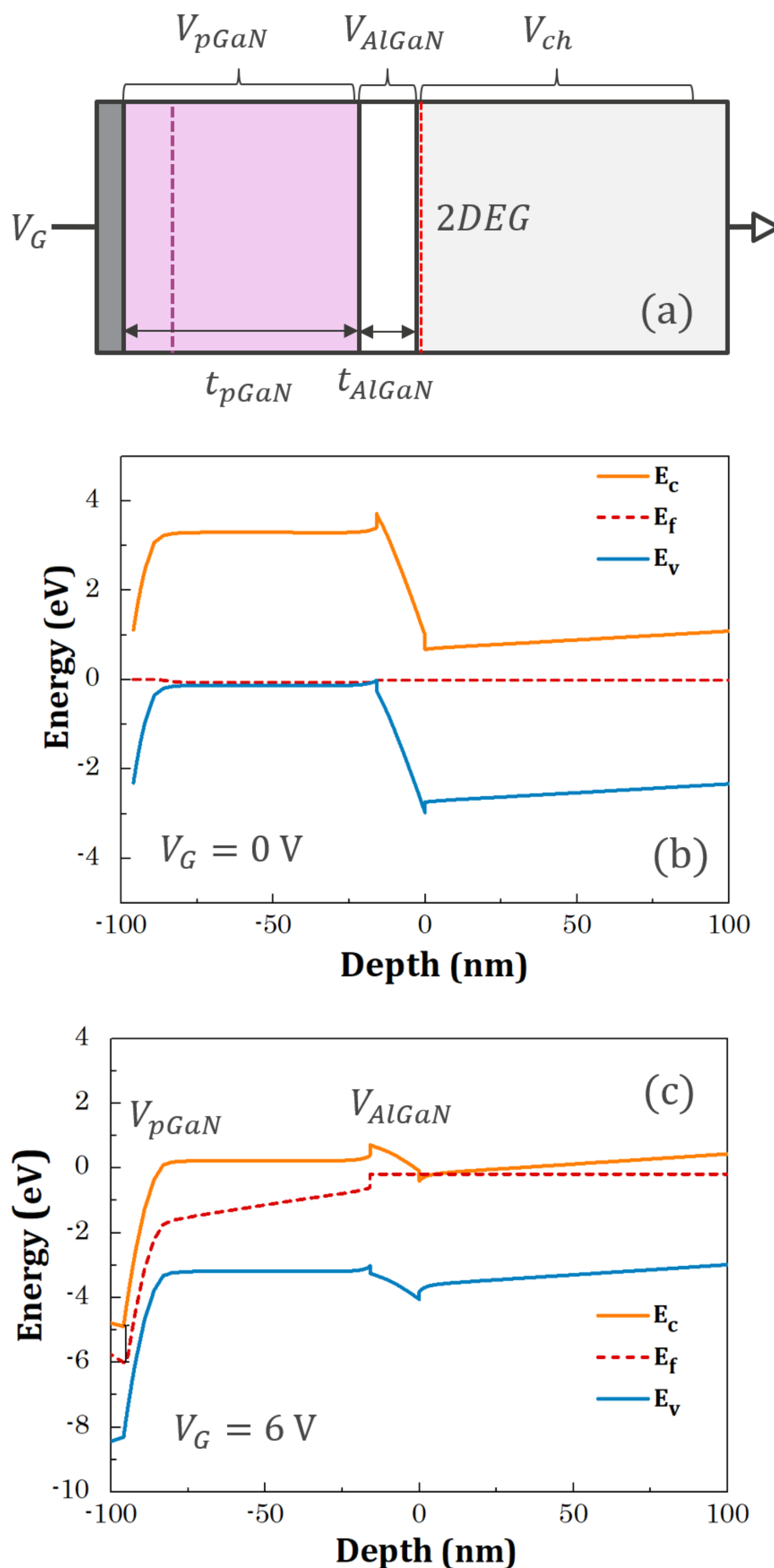

Figure 4.2: (a) Detailed cross section of the p-GaN/AlGaN/GaN structure with relative voltages along with the simulated energy-band diagram at (b) zero bias and (c) $V_G = 6$ V.

tion is solved self-consistently with the carrier continuity equations, taking into account the polarization charge [61]. From the energy band diagram we can see that the effect introduced by the p-GaN layer is to push down the Fermi level in the channel, causing the device to become normally-off. At zero bias (see figure 4.2b), the static voltage drop in each layer defines the threshold voltage of the device. The analysis of this important parameter has been exhaustively done by B. Bakeroot *et al.* [64] resulting in the following simplified equation:

$$V_{TH} = \psi_B + V_{bi} + \frac{\Delta E_{c1}}{q} - \frac{\Delta E_{c2}}{q} - V_b$$

where ψ_B is the Schottky barrier height of the metal towards the conduction band, V_{bi} the built-in potential of the Schottky contact, ΔE_{c1} the conduction band offset between the p-GaN and the AlGaN barrier, ΔE_{c2} the conduction band offset between the AlGaN and the GaN, and V_b the voltage barrier in the AlGaN resulting from the polarization and piezoelectric charge given by the unique polar properties of GaN materials. When a bias is applied, the vertical voltage drop is given by:

$$V_G = V_{TH} + V_{pGaN} + V_{AlGaN} + \psi_s(x) \tag{4.1}$$

where V_{pGaN} is the voltage drop in the p-GaN later and V_{AlGaN} is the voltage drop in the AlGaN which is dependent to the 2DEG charge:

$$V_{AlGaN} = \frac{q n_s}{\varepsilon_{AlGaN}} \cdot t_{AlGaN} \tag{4.2}$$

The surface potential $\psi_s(x)$ is strictly related with the energy of the electron in the 2DEG that is given by the Fermi level E_f and the channel potential dependence at any point x in the channel V(x):

$$\psi_s(x) = \frac{E_f}{q} + V(x)$$

It is interesting to see that equation 4.1 is the same as equation 2.3 introduced in Chapter 2 to model the AlGaN/GaN structure with the addition of the term V_{pGaN} to take into account the voltage drop in the p-GaN layer. This means that if V_{pGaN} is defined, the new structure can be implemented in the previously developed AlGaN/GaN model.

When a positive bias is applied (see figure 4.2), the surface potential $\psi_s(x)$ will start to increase until the energy of the electrons in the channel reaches the conduction band, leading to the formation of the 2DEG. Combining equations 4.1 and 4.2, the 2DEG charge can be expressed as follow:

$$n_s = \frac{\varepsilon_{AlGaN}}{q \cdot t_{AlGaN}} \cdot \left[V_G - V_{TH} - V_{pGaN} - \psi_s(x)\right] \tag{4.3}$$

The problem can be simplified if we assume a uniform charge distribution in the 2DEG, which is valid without loss of generality in case $V_S = V_D = 0$. In this case the surface potential is given by ψ_m and the charge in the channel is $q n_s = Q_{ch}$ leading to the following equation:

$$Q_{ch} = C_{AlGAN}\left[V_G - V_{TH} - V_{pGaN} - \psi_m\right] \tag{4.4}$$

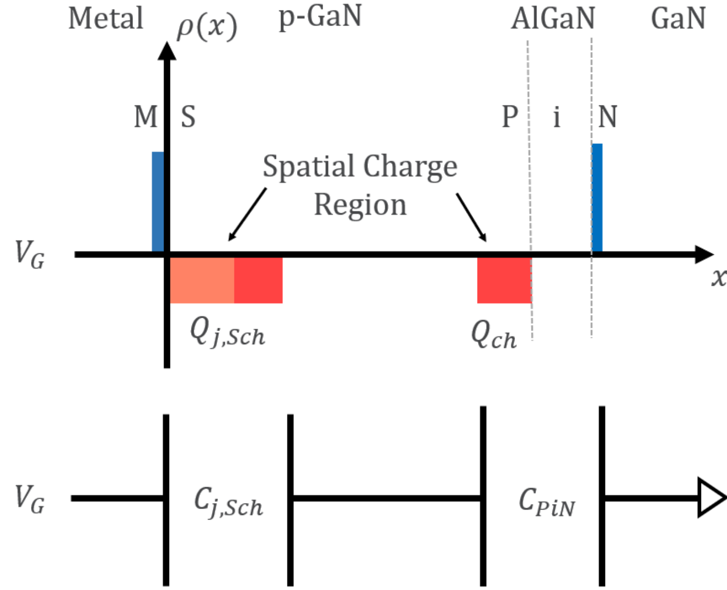

Figure 4.3: Qualitative representation of the charge distribution when a positive bias is applied in the p-GaN/AlGaN/GaN structure. Regarding the PiN junction the 2DEG channel can be considered equivalent to an highly doped n-type semiconductor.

4.2.1 Voltage Drop in the p-GaN Layer

V_{pGaN} is the result of two voltage drops: (i) is the drop in the metal/p-GaN contact which forms a Schottky junction and (ii) is the drop in the p-GaN/AlGaN contact which forms a PiN structure with the AlGaN as insulator and the two 2DEG as N-layer (see figure 4.3).

Schottky Junction

To model the Schottky junction we consider its depletion region like a series capacitance with C_{PiN} following the approach proposed by T. L. Wu *et al.* [61]. Consequently, they share the same dynamic charge:

$$dQ_{ch} = C_{PiN}\, dV_{PiN} = C_{j,Sch}\, dV_{j,Sch}$$

The Schottky junction capacitance is given by:

$$\boxed{C_{j,Sch} = \frac{C_{j0}}{\left(1 + \frac{V_{j,Sch}}{V_{bi}}\right)^m}} \tag{4.5}$$

where $m = (0 \sim 1)$ is a dimensionless non-ideality factor usually used to describe the non-uniformity of the doping profile [65]. In case of non-uniform doping:

$$Q = q \int_0^{x_d} N(x)\, dx \tag{4.6}$$

Then:

$$C = \frac{dQ}{dV} = \frac{dQ}{dx} \cdot \frac{dx}{dV}$$
$$= qN(x)\frac{dx}{dV}$$
$$= qN(x)\frac{dx}{dC} \cdot \frac{dC}{dV}$$

where:

$$\frac{dx}{dC} = \varepsilon \frac{d(C^{-1})}{dC} = -\frac{\varepsilon}{C^2} \Longrightarrow \quad qN(x) = -\frac{C^3}{q\varepsilon \cdot \frac{dC}{dV}} \tag{4.7}$$

From equation 4.5, equation 4.7 can be divided in:

$$\left.\begin{aligned} &\text{(i)} \quad \frac{dC}{dV} = -\frac{mC_{j0}}{V_{bi}}\left(1+\frac{V}{V_{bi}}\right)^{-1-m} \\ &\text{(ii)} \quad C^3 = C_{j0}^3\left(1+\frac{V}{V_{bi}}\right)^{-3m} \end{aligned}\right\} \quad \frac{\text{(ii)}}{\text{(i)}} = -\frac{V_{bi}C_{j0}^2}{m}\left(1+\frac{V}{V_{bi}}\right)^{1-2m}$$

Finally, the non-uniform doping profile can be expressed as:

$$N(V) = \frac{V_{bi}C_{j0}^2}{q\varepsilon m}\left(1+\frac{V}{V_{bi}}\right)^{1-2m}$$

$$\boxed{\text{If} \quad C_{j0} = \sqrt{\frac{qN_A\varepsilon}{2V_{bi}}} \quad \Longrightarrow \quad N(V) = \frac{N_A}{2m}\left(1+\frac{V}{V_{bi}}\right)^{1-2m}} \tag{4.8}$$

From equation 4.8 we can see that if (1) $m < 1/2$, $N(V)$ will increase with the increase of the voltage and if (2) $m > 1/2$, N(V) will decrease. To verify the result just obtained in equation 4.8, we can start from the equation that relates the thickness of the depletion region and the capacitance of equation 4.5:

$$x_d = \frac{\varepsilon}{C} = \sqrt{\frac{2\varepsilon V_{bi}}{qN_A}}\left(1+\frac{V}{V_{bi}}\right)^m \tag{4.9}$$

Then:

$$\frac{dx}{dV} = \frac{m}{V_{bi}}\sqrt{\frac{2\varepsilon V_{bi}}{qN_A}}\left(1+\frac{V}{V_{bi}}\right)^{m-1}$$

$$\Longrightarrow \quad dx = \frac{m}{V_{bi}}\sqrt{\frac{2\varepsilon V_{bi}}{qN_A}}\left(1+\frac{V}{V_{bi}}\right)^{m-1} dV$$

From equation 4.6, combined with equations 4.8 and 4.9:

$$
\begin{aligned}
Q &= q\int_0^{x_d} N(x)\,dx = q\int_0^{V} N(V)\cdot\frac{m}{V_{bi}}\sqrt{\frac{2\varepsilon V_{bi}}{qN_A}}\left(1+\frac{V}{V_{bi}}\right)^{m-1} dV \\
&= \int_0^{V} \frac{qN_A}{2m}\left(1+\frac{V}{V_{bi}}\right)^{1-2m}\frac{m}{V_{bi}}\sqrt{\frac{2\varepsilon V_{bi}}{qN_A}}\left(1+\frac{V}{V_{bi}}\right)^{m-1} dV \qquad (4.10) \\
&= \int_0^{V} \sqrt{\frac{qN_A\varepsilon}{2V_{bi}}}\left(1+\frac{V}{V_{bi}}\right)^{-m} dV = \int_0^{V} C\,dV
\end{aligned}
$$

Analyzing equations 4.5, 4.8, 4.9, and 4.10, we can see that charge, capacitance, non-uniform doping and thickness are all correctly related, meaning that the model is self-consistent. From equation 4.10, the charge depleted in the Schottky junction can be calculated solving the integral:

$$
\boxed{Q_{j,Sch} = \frac{V_{bi}}{1-m}\sqrt{\frac{qN_A\varepsilon_{GaN}}{2V_{bi}}}\left(1+\frac{V_{j,Sch}}{V_{bi}}\right)^{1-m}} \qquad (4.11)
$$

Since, the Schottky capacitance can be considered in series with the PiN capacitance, the charge $C_{j,Sch}$ is the sum of the static charge Q_0 that corresponds to equation 4.11 at zero bias, and the dynamic charge Q_{ch} (see figure 4.3):

$$
\begin{cases}
Q_{j,Sch} = Q_0 + Q_{ch} \\
Q_0 = \dfrac{V_{bi}}{1-m}\sqrt{\dfrac{qN_A\varepsilon_{GaN}}{2V_{bi}}}
\end{cases} \qquad (4.12)
$$

Combining equation 4.11 and equation 4.12 and squaring both sides we obtain:

$$
(Q_0+Q_{ch})^2 = \left(Q_{j,Sch}\right)^2
$$

$$
(Q_0+Q_{ch})^2 = \left[Q_0\cdot\left(1+\frac{V_{j,Sch}}{V_{bi}}\right)^{1-m}\right]^2 (Q_0+Q_{ch})^2
$$

$$
\implies \quad V_{j,Sch} = V_{bi}\cdot\left[\left(1+\frac{Q_{ch}}{Q_0}\right)^{\frac{1}{1-m}} - 1\right]
$$

The voltage drop in the Schottky junction can be expressed as:

$$
\boxed{V_{j,Sch} = V_{bi}\cdot\left[\left(1+Q_{ch}\cdot\sqrt{\frac{2(1-m)^2}{qN_A\varepsilon_{GaN}V_{bi}}}\right)^{\frac{1}{1-m}} - 1\right]} \qquad (4.13)
$$

In case of uniform doping where $m = 1/2$, equation 4.13 becomes:

$$V_{j,Sch} = \frac{Q_{ch}^2 + 2Q_{ch}\sqrt{2qN_A\varepsilon_{GaN}V_{bi}}}{2qN_A\varepsilon_{GaN}} \tag{4.14}$$

From equation 4.14, it is interesting to observe that:

(i) at zero bias the device is off, $Q_{ch} = 0$, and the dynamic voltage drop in the Schottky junction is zero;

(ii) the voltage drop in the p-GaN is inversely proportional to the doping level;

(iii) $V_{j,Sch}$ has a quadratic dependence with the gate charge while the AlGaN layer $V_{AlGAN} = Q_{ch}/C_{AlGaN}$ is linearly dependent.

PiN Junction

To model the voltage drop in the PiN junction, it is important to assume that the 2DEG channel is equivalent to a particular highly doped n-type semiconductor where the doping level is modulated by the charge density in the channel and therefore by the gate voltage. The analysis starts from equation 4.15, which describes the relationship between the electric field of the p-type semiconductor and the insulator contacts under the simplified assumption that there is no surface charge present between the p-GaN and the AlGaN:

$$\varepsilon_{GaN}\mathscr{E}_P = \varepsilon_{AlGaN}\mathscr{E}_{AlGaN} \tag{4.15}$$

The two electric fields are defined as:

$$\begin{cases} \mathscr{E}_P = \dfrac{qN_A}{\varepsilon_{GaN}} t_P \\ \mathscr{E}_{AlGaN} = \dfrac{qn_s}{\varepsilon_{AlGaN}} \end{cases} \tag{4.16}$$

Combining equations 4.15 and 4.16 leads to:

$$qN_A t_P = qn_s$$

$$\implies \quad t_P = \frac{n_s}{N_A} \tag{4.17}$$

Equation 4.17 express the thickness of the depletion region in the p-GaN/AlGaN contact as proportional with the charge in the channel and inversely proportional with the Mg concentration in the p-GaN. From equation 4.6 and under the assumption of uniform distribution, which is valid without loss of generality in case $V_S = V_D = 0$, we can relate the gate charge with t_P:

$$t_P = \frac{Q_{ch}}{qN_A} \tag{4.18}$$

The potential drop in the p-GaN is given by:

$$V_P = \int_0^{t_P} \mathscr{E}_P \, dx = \frac{qN_A}{2\varepsilon_{GaN}} t_P^2 \tag{4.19}$$

Combining equations 4.18 and 4.19:

$$V_P = \frac{Q_{ch}^2}{2qN_A\varepsilon_{GaN}} \tag{4.20}$$

From equation 4.20, which describes the dynamic voltage drop in the p-GaN/AlGaN contact, we can do the same considerations of equation 4.14, observing that:

(i) at zero bias the device is off, $Q_{ch} = 0$, and the dynamic voltage drop in the p-GaN/AlGaN contact is zero;

(ii) the voltage drop in the p-GaN is inversely proportional to the doping level;

(iii) V_P has a quadratic dependence with the gate charge. This means that for high voltages, the voltage drop in the p-layer will become predominant.

The total drop in the p-GaN layer is given by the contribution of both equations 4.13 and 4.20, which in case of uniform doping with $m = 1/2$ becomes:

$$V_{pGaN} = \frac{Q_{ch}^2 + Q_{ch}\sqrt{2qN_A\varepsilon_{GaN}V_{bi}}}{qN_A\varepsilon_{GaN}} \tag{4.21}$$

4.2.2 Fully Depleted p-GaN

The thickness of the p-GaN is an important parameter to take into account. From equation 4.21, we see that the extension of the depletion region is inversely proportional to the doping level in the p-GaN. If the Mg concentration is low enough, the depletion region will extend significantly up to the case of a fully depleted device. In case of fully depleted p-GaN layer, the Space Charge Region (SCR) cannot continue to increase and the relative capacitance becomes constant and equal to:

$$C_{fd} = \frac{\varepsilon_{GaN}}{t_{pMAX}}$$

To have a smooth and continuous transition, we propose to solve the problem starting from the definition of voltage drop in a fully depleted device. In this case the capacitance is constant and the voltage drop is given by:

$$V_{fd} = \frac{Q_{ch}}{C_{fd}} = Q_{ch} \cdot \frac{t_{pMaX}}{\varepsilon_{GaN}} \tag{4.22}$$

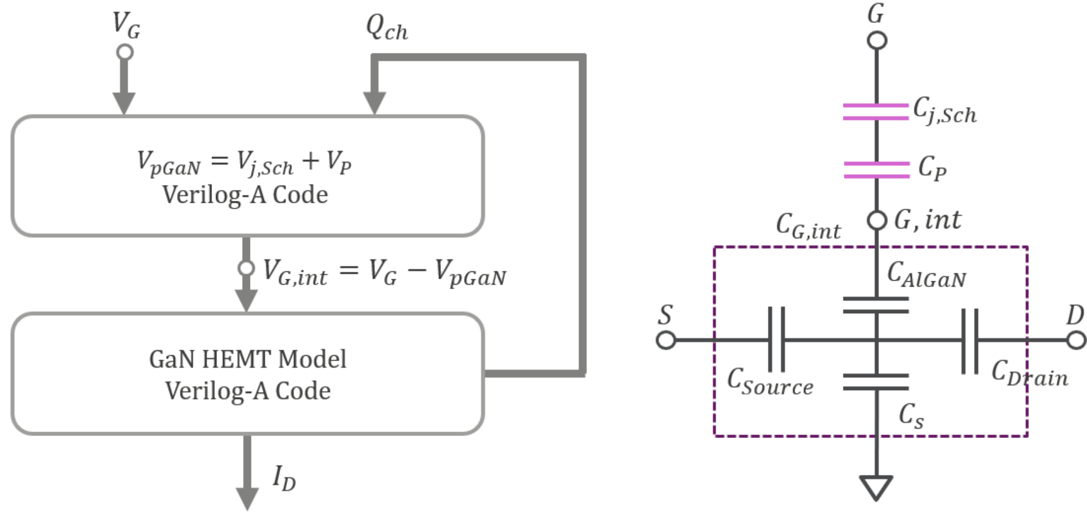

Figure 4.4: Modeling flow-chart used to simulate the p-GaN/AlGaN/GaN structure next to its equivalent circuit

Equations 4.21 and 4.22 can be interpolated using the following classic interpolation scheme:

$$V_{p,eff} = \frac{V_{pGaN}}{\sqrt[k]{1+\left(\frac{V_{pGaN}}{V_{fd}}\right)^k}} \tag{4.23}$$

where k is an interpolation coefficient with default value $k = 2$. Using this expression to define the voltage drop in the p-GaN layer, we take into account the fact that the SCR cannot extent above a maximum value t_{pMAX}.

The calculation of the charge in the channel which is strongly related with the surface potential and therefore the Fermi level (see equation 4.4), can be obtained solving the Schrödinger's and Poisson's equations. This is done by different physics-based compact models [31, 29, 30], each one with a different algorithm.

In this case, the p-layer has been implemented using Verilog-A in the core model presented in Chapter 2. Figure 4.4 shows the modeling flow-chart used to simulate the p-GaN/AlGaN/GaN structure next to its equivalent circuit. The new developed model has been used to study the impact of the p-type layer starting from the device measurements of four samples.

4.3 Results

To verify the developed mode, it has been used to fit the experimental data of four samples. The heterostructures are grown by MOCVD on a 200 mm silicon (111) substrate. A 70 nm Mg-doped p-type GaN is grown on top of an epitaxial stack consisting of an AlN nucleation layer, GaN buffer layer, GaN channel, and 16 or 12.5 nm $Al_{0.25}Ga_{0.75}N$ barrier layer.

Two different flows in growing the last p-type GaN ayer are used [61]. To investigate the C-V characteristics, a simple 75 μm × 75 μm is fabricated. A summary of the important process parameters can be found in table 4.1.

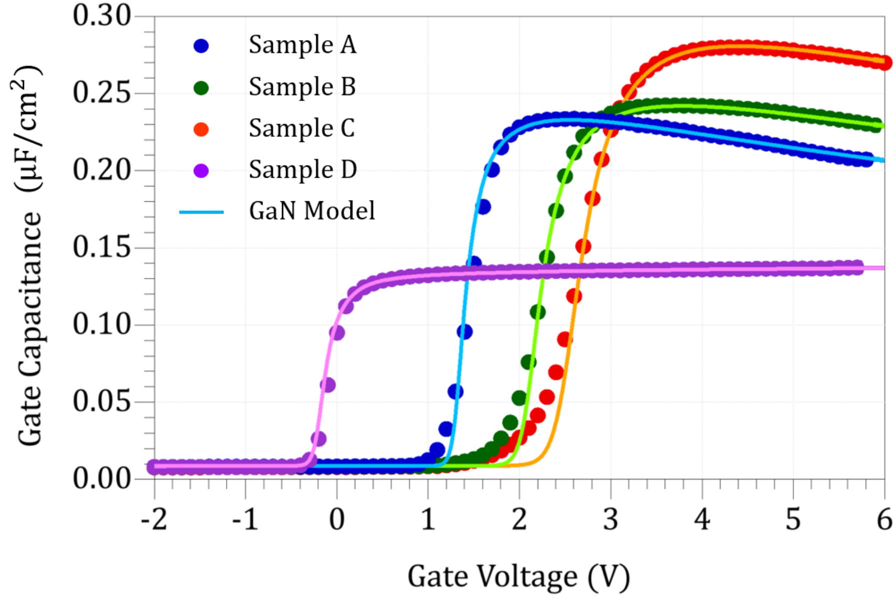

Figure 4.5: Measured and simulated C-V characteristic. The simulation shows excellent agreement with the experimental data for all the samples. In case of Samples A, B, and C, with the increase of the gate voltage it follows the decrease of the capacitance due to the increase of the depletion region thickness, while in case of Sample D which has a fully depleted p-GaN it remains constant.

4.3.1 Gate Capacitance

In figure 4.5 the simulation and the measured experimental data are compared showing excellent agreement and demonstrating that the new developed model is able to include the effect of the p-GaN layer. Since the developed model is physical based, it allows an unprecedented insight of the effect of each layer in the structure. In fact, the total gate capacitance is the resulting of the series of the Schottky junction, the PiN junction and the surface capacitance:

$$C_G = \left(\frac{1}{C_{j,Sch}} + \frac{1}{C_{PiN}} + \frac{1}{C_s} \right)^{-1} \tag{4.24}$$

In figure 4.6, the contribution given by each series capacitor is plotted for Sample A. The three capacitance are sharing the same dynamic charge dQ_{ch}, so their relative

	Sample A	Sample B	Sample C	Sample D
Mg flow	Low	Medium	Medium	Very Low
AlGaN	16 nm	16 nm	12.5 nm	16 nm
$L \times W$	75 × 75 μm	75 × 75 μm	75 × 75 μm	75 × 75 μm
Al	25%	25%	25%	25%
p-GaN	70 nm	70 nm	70 nm	70 nm

Table 4.1: Summary of the important device parameters of Samples A,B,C, and D.

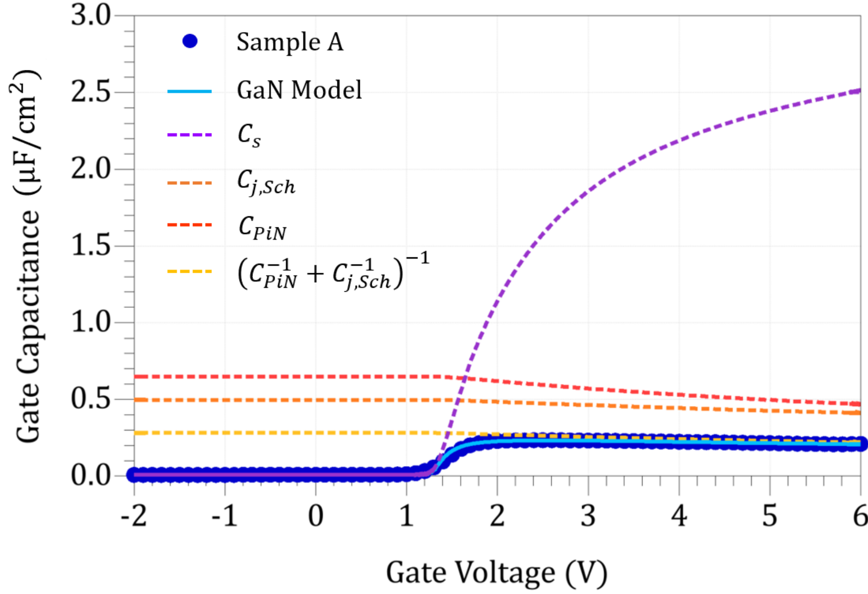

Figure 4.6: Contribution of each capacitance in the p-GaN/AlGaN/GaN structure for the calculation of the total capacitance C_G of Sample A. For $V_G > V_{TH}$, when the 2DEG is formed, the surface capacitance C_s becomes big enough to be considered negligible in the calculation of the total capacitance C_G.

values can be calculated from the respective voltage drop as:

$$C_x = \frac{dQ_{ch}}{dV_x}$$

In figure 4.7(a, b, c, and d), the effect of the Schottky junction capacitance in series with the PiN capacitance is highlighted for Samples A, B, C, and D respectively. Unlike MIS-HEMT, where the total capacitance is the series capacitance of the two insulator layers in the stack, the p-GaN introduces the effect of lowering the total gate capacitance as the gate voltage increases, as a consequence of the increase of the SCR thickness. Since the developed model is physical-based, the number of parameters is reduced and the extraction is facilitate.

Table 4.2 shows the extracted parameters for Samples A, B, C and D. The extracted N_A indicates that in Samples A, B, and C the Mg concentration is always around 10^{19} cm^{-3}. The main reason why Sample C looks higher compared to Sample A and B is due to the thickness of the AlGaN, which is 12.5 nm in Sample C and 16 nm in Sample A and B.

4.3.2 Depletion Region

In Sample D, the gate capacitance behaves differently because the Mg concentration is significantly lower compared to the other three samples. In this case C_G is constant and the p-layer can be considered fully depleted since the SCR is not extending anymore. From figure 4.7d, we can see that at a sufficiently high gate voltage, for example $V_G = 4$ V, the contribution of C_s can be neglected and the gate capacitance is given simply by C_{PiN} and $C_{j,Sch}$. In the fully depleted case this is

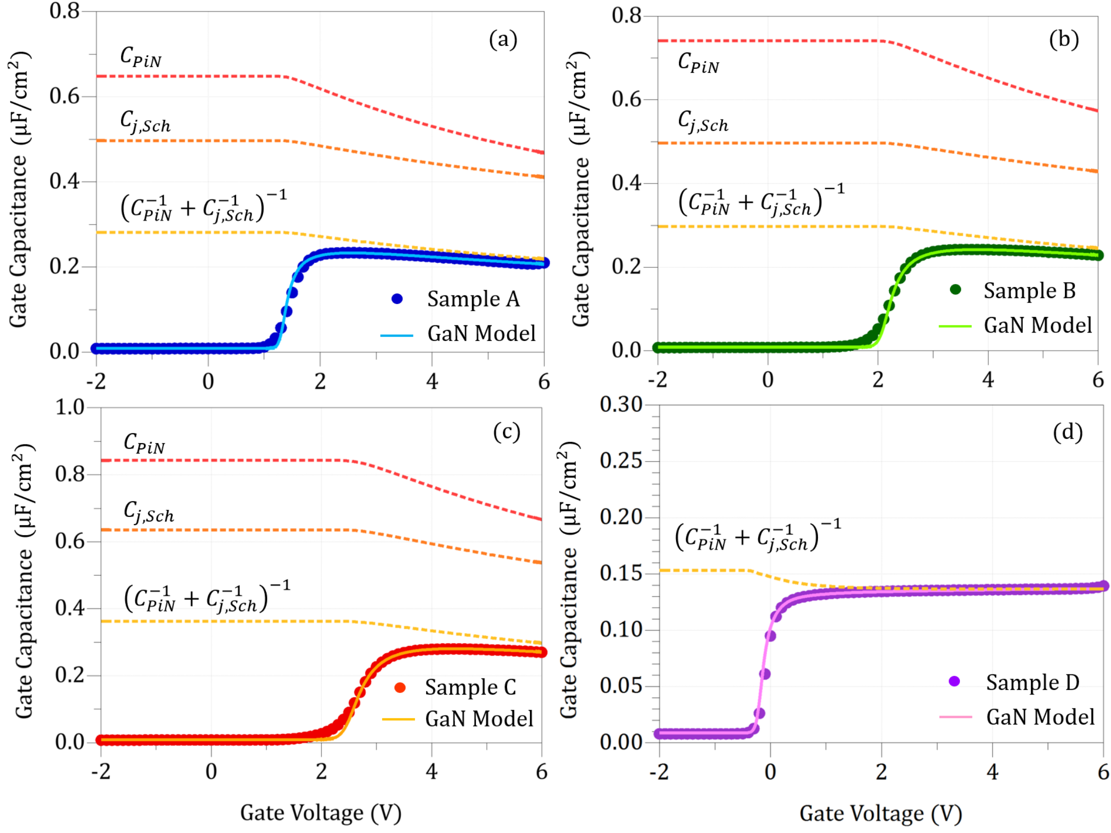

Figure 4.7: Detail of the effect of the Schottky and the PiN junction lowering the total capacitance when the gate voltage increases for Samples A, B, and C. In case of Sample D the device is fully depleted so since the voltage drop is defined by the interpolation of equations 4.21 and 4.22, it becomes hard to distinguish the single effect of the Schottky junction and the PiN junction. For this reason only their total contribution is plotted.

equivalent to:

$$C_G = \left(\frac{t_{pMAX}}{\varepsilon_{GaN}} + \frac{t_{AlGaN}}{\varepsilon_{AlGaN}}\right)^{-1}$$

The maximum extension of the depletion region can be extracted:

$$t_{pMAX} = \varepsilon_{GaN} \cdot \left(\frac{1}{C_G} - \frac{t_{AlGaN}}{\varepsilon_{AlGaN}}\right)$$

As we can see in table 4.2, the extracted value is $t_{pMAX} = 41.5$ nm which is smaller than the expected $t_{pGaN} = 70$ nm. This means that the depletion region in a fully depleted device is not extending along all the p-GaN layer but it will saturate at a maximum value $t_{pMAX} < t_{pGaN}$.

To have an intuition of the reason why this happens, in figure 4.10 a qualitative representation of the charge distribution in the two series capacitors is plotted. When the gate voltage increases, the thickness of the depletion region in both contacts increases causing the decrease of the corresponding capacitance.

Under the assumption that the charge in the plates of the capacitance must be the same, the extension of the depletion region will continue to increase until the charge N_A in the p-type semiconductors is enough to guarantee that the charge in

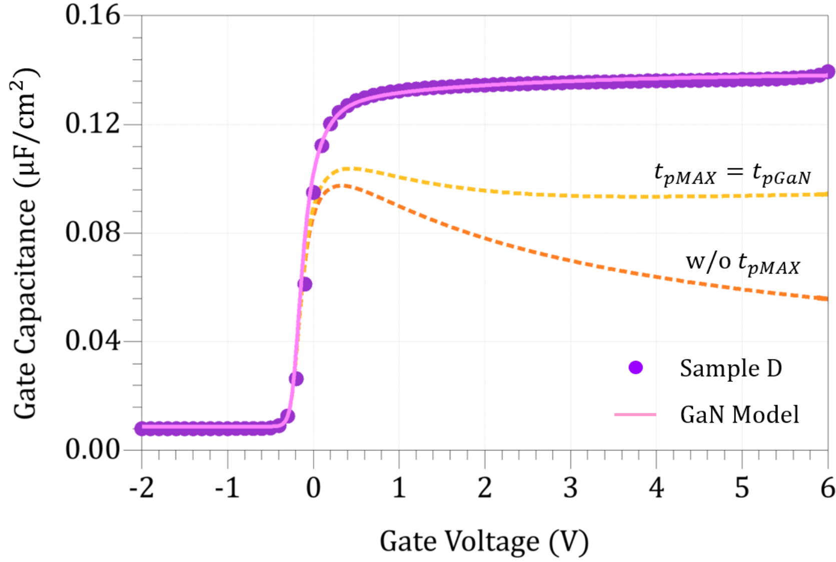

Figure 4.8: Simulation result of Sample D setting the maximum extension of the depletion region equal to the thickness of the p-GaN layer and without taking into account the maximum extension of the depletion region.

the two plates of the PiN capacitance is balanced. If the entire p-layer is emptied the 2DEG should disappear to maintain the conservation of the charge. For this reason $t_{pMAX} < t_{pGAN}$.

Figure 4.8 shows the result of the simulation conducted on Sample D comparing the cases $t_{pMAX} = 41.5$ nm with $t_{pMAX} = t_{pGAN} = 70$ nm, and $t_{pMAX} = \infty$. If $t_{pMAX} = t_{pGAN} = 70$ nm, at $V_G = 4$ V the gate capacitance becomes too small, confirming that the depletion region is not extending along all the p-GaN layer. If the maximum extension of the SCR is not considered and equation 4.21 is used instead of equation 4.23, the gate capacitance will continue to decrease.

The extracted $t_{pMAX} = 42$ nm is significantly smaller compared to the p-GaN thickness because in case of Sample D the doping level is very low. Since for Samples A, B, and C the doping is very high and consequently the effect introduced by

	Unit	Sample A	Sample B	Sample C	Sample D
N_A	cm^{-3}	1.35×10^{19}	1.75×10^{19}	2.2×10^{19}	4×10^{17}
V_{bi}	V	1.95	1.95	1.95	1.2
V_{TH}	V	1.5	2.4	2.9	0.1
C_{GSO}	μF/cm^2	0.008	0.008	0.008	0.008
t_{pMAX}	nm	65	65	65	42
n_{factor}	-	0.5	1.5	2.5	0.5
m	-	0.5	0.5	0.5	0.5
k	-	3	3	3	3

Table 4.2: Summary of the extracted parameters for Samples A,B,C, and D.

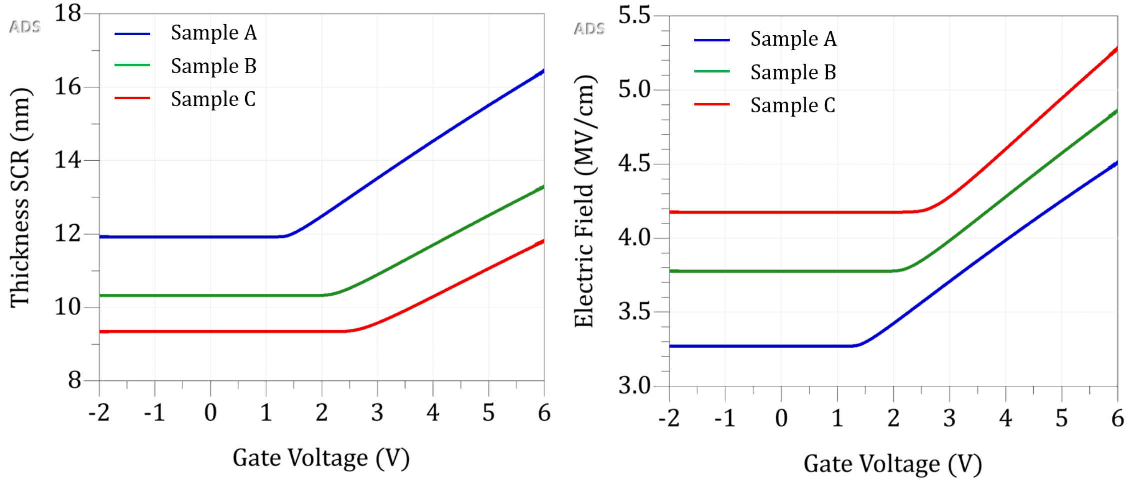

Figure 4.9: Depletion region in Sample A, B, and C next to the corresponding Electric field in the Schottky junction.

the saturation of the depletion region is almost negligible. With this assumption, the thickness and the electric field in the Schottky junction can be calculated as:

$$\begin{cases} t_{j,Sch} = \dfrac{\varepsilon_{GaN}}{C_{j,Sch}} = \sqrt{\dfrac{2\varepsilon_{GaN} V_{bi}}{qN_A}} \left(1 + \dfrac{V_{j,Sch}}{V_{bi}}\right)^m \\ \mathscr{E}_{j,Sch} = \dfrac{2(V_{bi} + V_{j,Sch})}{t_{j,Sch}} \end{cases} \tag{4.25}$$

Figure 4.9 shows that in case of high Mg concentration, the average thickness of the Schottky junction is around $t_{j,Sch}$ = 13 nm with an electric field of $\mathscr{E}_{j,Sch}$ = 3.7 MV/cm. In Chapter 1 table 1.1 we can see that the breakdown voltage in GaN materials is around 3.3 MV/cm which is slightly smaller than the average simulated electric field in the Schottky junction. The value of $\mathscr{E}_{j,Sch}$ is particularly high also

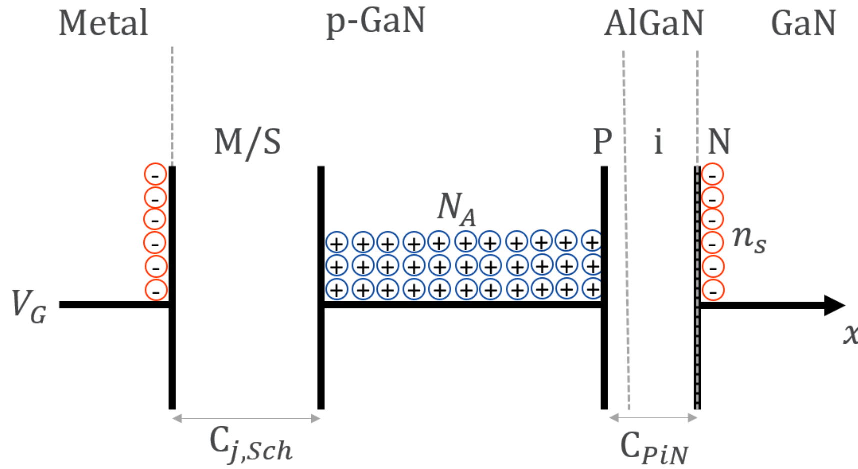

Figure 4.10: Qualitative representation of the charge distribution in the two series capacitance. To keep the charge balanced, the p-layer cannot be completely depleted.

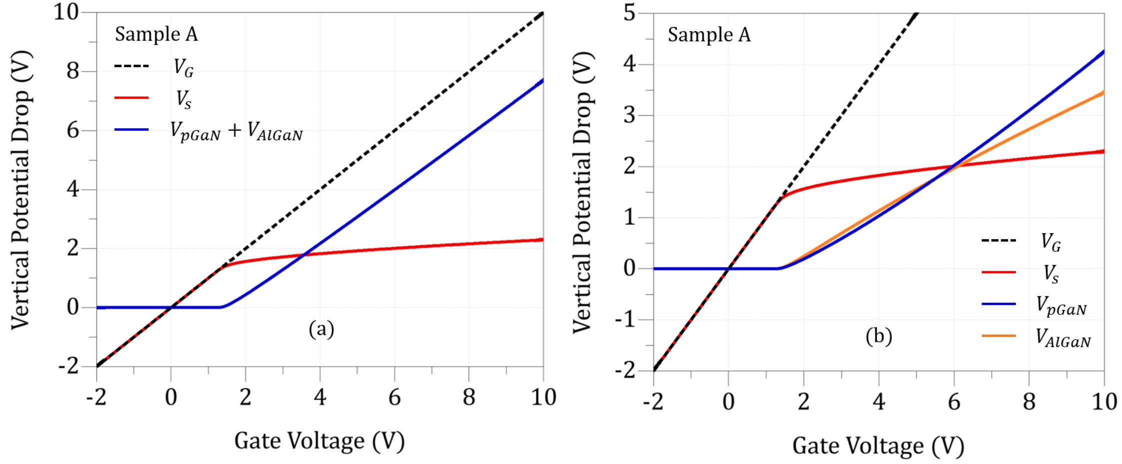

Figure 4.11: Vertical voltage drop in the channel vs voltage drop in the p-GaN and AlGaN layers. The simulation is calibrated with the extracted parameters of Sample A.

at zero bias confirming that such magnitude is not dependent from the model but from the material parameters. In fact at zero bias the electric field is:

$$\mathscr{E}_{j0} = \frac{2V_{bi}}{t_{j0}} = \sqrt{\frac{2qN_A V_{bi}}{\varepsilon_{GaN}}} \tag{4.26}$$

where t_{j0} is the thickness of the deletion region at zero bias. Here, it is important to observe that this is not the average electric field in the Schottky junction but the maximum electric field at the metal-semiconductor interface. The average electric field along the depletion region can be calculated as:

$$\mathscr{E}_{j,m} = \frac{\mathscr{E}_{j,MAX} + \mathscr{E}_{j,MIN}}{2} = \frac{\mathscr{E}_{j,MAX}}{2} \sim 1.8 MV/cm \tag{4.27}$$

which is smaller than $\mathscr{E}_{BR} = 3.3$ MV/cm. Furthermore, it has to considered that the model of the metal/semiconductor interface ignored some possible effects that take place when the metal is deposited on the GaN material such as inhomogenities, dangling bond and any abrupt change at the interface.

4.3.3 Vertical Potential Drop

Thanks to the developed model, we can give an unprecedented insight of the potential drop in each layer of the device. To do so, we will not consider the voltage drop at zero bias given by the static elements of the heterojunction such as work function, built-in potential, piezoelectric polarization charge, and conduction band offset [64], but only the dynamic potential, to see how it is divided in each layer of the device with the increase of the gate voltage.

Figure 4.11 shows the vertical voltage drop in the p-GaN/AlGaN/GaN structure while fitting the experimental data of Sample A. In figure 4.11a it is possible to see that:

- if $V_G < V_{TH}$ the increase of the gate voltage is all taken by the channel which sees an increase of the Fermi level until it reaches the conduction band and the 2DEG is formed;

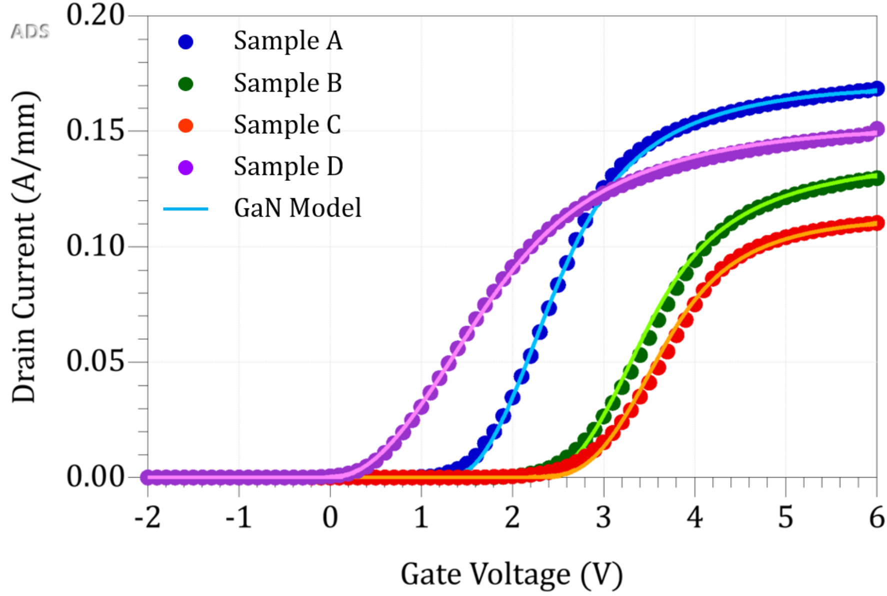

Figure 4.12: Measured and simulated I_D-V_G characteristic. The simulation shows good agreement with the experimental data for all the samples.

- if $V_G > V_{TH}$, the potential in the channel is almost saturated and the increase in the gate voltage is taken by the p-GaN and he AlGaN layer.

In figure 4.11b we can see in detail how the voltage drop is divided between the p-GaN and AlGaN. In case of high doping, the two drops are almost the same for all the operation region since V_{pGaN} is inversely proportional to the doping level as we can see in equation 4.23. If the simulation is conducted up to 10 V, at a certain moment, the p-GaN voltage will become dominant since its dependence with Q_{ch} is quadratic while for the AlGaN is linear. The same considerations are valid also for Sample B and C.

4.3.4 I_D-V_G

To conclude the developed physical-based model of the p-GaN/AlGaN/GaN HEMT has been used to fit the I_D-V_G measurements for each sample showing a good agree-

	Unit	Sample A	Sample B	Sample C	Sample D
$L \times W$	μm	0.8×100	0.8×100	0.8×100	0.8×100
μ_0	cm^2/Vs	1400	1100	1000	1400
μ_a	-	5×10^{-9}	7×10^{-9}	9×10^{-9}	2×10^{-9}
μ_b	-	5×10^{-17}	3×10^{-17}	6×10^{-17}	8×10^{-17}
v_S	cm/s	1.1×10^5	1.1×10^5	1.1×10^5	1.1×10^5
$n_{s,acc}$	cm^{-2}	7.5×10^{12}	7.5×10^{12}	7.5×10^{12}	6.5×10^{12}

Table 4.3: Summary of the extracted parameters for Samples A,B,C, and D.

ment with the experimental data and confirming the validity of the model. Figure 4.12 shows the result of the simulation compared with the measured drain current while tables 4.2 and 4.3 indicate all the extracted parameters. The meaning of all these parameters is explained in Chapter 2. The velocity saturation and the mobility in the access region are assumed to be the same as in the channel.

4.4 Conclusion

In this chapter, we proposed a novel approach to extend the GaN model developed in Chapter 2, including a p-GaN layer under the gate of the AlGaN/GaN structure. To the best of the knowledge of the author this is the first time a physical-based compact model includes such structure. The physics and the strategy used to implement the Verilog-A code has been well explained and verified comparing the simulation results with the experimental data measured on four different devices. Inspired by the method used in this chapter to include the p-GaN layer under the gate, and aware of the results that ferroelectric materials are showing, in the rising NCFET technology, when deposited under the gate of Si-based devices, the main objective of the next chapter study is to try to implement the negative capacitance in the AlGaN/GaN model to study how this unique material can improve the DC performance of GaN-based devices.

Chapter 5

Negative Capacitance in GaN HEMT

5.1 Concept and Reasons

The necessity for extremely low power consumption in not only important in the high power electronic applications but also in low power systems, which requires this property to better conduct data sensing, data processing and data communication [66]. At transistor level, the most effective way to reduce power consumption is lowering the supply voltage V_{dd}. However, if V_{dd} is lowered, the drive current of the transistor is also reduced. if the drive current is reduced, the circuit delay is increased and off-state leakage current keeps flowing during the period [67], which is not desirable from the low power consumption perspective .

In order to achieve energy-efficient switching at given V_{dd}, the ratio between ON-current and OFF-current needs to be as high as possible. The increase in I_{ON}/I_{OFF} can be translated in a decrease of the sub-threshold slope of the transistor [68]. In general, the sub-threshold slope (SS) is expressed by:

$$SS = \frac{\delta V_G}{\delta \log_{10}(I_{DS})} = \left(\frac{\delta \psi_s}{\delta \log_{10}(I_{DS})}\right) \cdot \left(\frac{\delta V_G}{\delta \psi_s}\right) \tag{5.1}$$

where ψ_s is the surface potential. The first term of equation 5.1 is a transport term which represent the conductance, meaning how much current can flow by lowering the potential along the channel. Standard FET analysis shows that this ratio is $\sim 2.3 \cdot k_B T/q$ because of the so-called Boltzmann tyranny which defines the fundamental thermionic limit of the SS that in case of a MOSFET is 60 mV/dec at room temperature [66].

The second term is a voltage divider term which represent how efficiently the surface potential ψ_s can bend at a given gate voltage V_G [67]. Since V_G and ψ_s are related by a capacitive voltage divider as shown in figure 5.1a, it is apparent that the second term (often called the body factor m) given by:

$$\frac{\delta V_G}{\delta \psi_s} = 1 + \frac{C_s}{C_{ins}} \tag{5.2}$$

must exceed one, thus putting a lower limit to the sub-threshold slope of 60 mV/dec. To overcome this limit, Tunnel Field-Effect Transistor (TFET) improves the first term by utilizing band-to-band tunnelling and energy filtering between source and

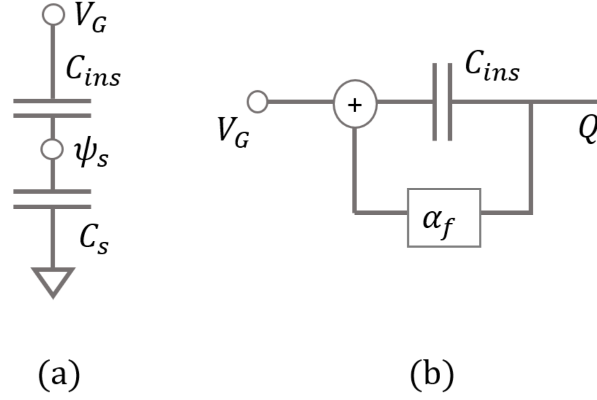

Figure 5.1: (a) Equivalent circuit for the division of the gate voltage between the insulator capacitance and the semiconductor capacitance in a standard FET structure. (b) Block diagram of a special capacitance with positive feedback to introduce the concept of negative capacitance.

channel band edges [67]. Negative Capacitance Field-Effect Transistor (NCFET) improves the second term by amplifying ψ_s due to negative capacitance of the ferroelectric gate insulator [68].

In the last few years, a number of proof-of-concept demonstrations of negative capacitance have been achieved [69, 70, 71, 72]. The physical mechanism that allows ferroelectric materials to show negative capacity can be understood in terms of positive feedback as follows. Suppose we have a (positive) capacitor C_0 (F/cm^2) that sees a terminal voltage equal to the applied voltage V plus a feedback voltage $\alpha_f Q$ proportional to the charge on the capacitor Q (C/cm^2), like the one shown in figure 5.1b:

$$Q = C_0(V + \alpha_f Q) \tag{5.3}$$

This yields:

$$Q = \frac{C_0}{1 - \alpha_f C_0} \cdot V = C_{ins} V$$

Clearly with $\alpha_f C_0 > 1$, C_{ins} becomes negative, leading to an instability so that the charge would increase until limited by the nonlinear terms that have been neglected in this qualitative example. The negative capacitor can be stabilize by putting an ordinary capacitor C_s in series so that the overall capacitance $C_{tot} = (1/C_{ins} + 1/C_s)^{-1}$ is positive. From equations 5.1 and 5.2 it follows that the body factor:

$$\frac{\delta V_G}{\delta \psi_s} = 1 - \frac{C_s}{C_0} \cdot (\alpha_f C_0 - 1) \tag{5.4}$$

can, in principle, be made arbitrarily small showing that the negative capacitance can be used as a voltage transformer that steps up the applied potential V_G into the channel potential ψ_s [73]. More generally, the linear capacitor of equation 5.3 could be replaced with a more general non linear capacitance function, such that

$$V = F^{-1}(Q) - \alpha_f Q$$

that can be expanded up to the fifth power to write:

$$V = \alpha_0 Q + \beta_0 Q^3 + \gamma Q^5 \tag{5.5}$$

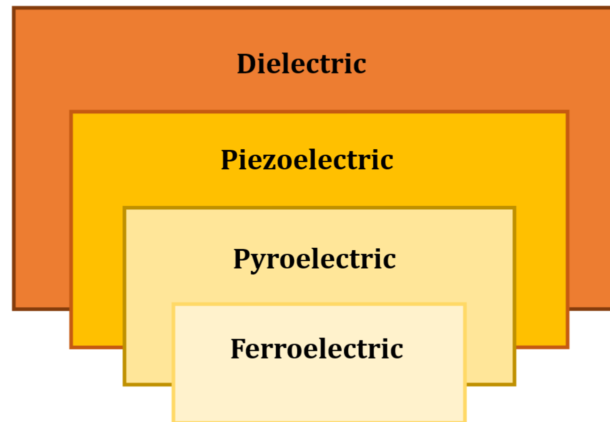

Figure 5.2: Classification of ferroelectric within the group of (crystalline) dielectrics. Ferroelectric are a subgroup of pyroelectric, which themselves are a subgroup of piezoeletric.

where the parameter $\alpha_0 = 1/C_0 - \alpha_f$. With this premise, the generic role of positive feedback in giving rise to negative capacitance has been presented. It should be noted that equation 5.5 does not just represent a toy model for ferroelectrics. In fact, it can be obtained starting from the state-of-the-art approach for modeling the dynamics of ferroelectric capacitors based on the Landau-Khalatnikov (LK) equation [74], which will be introduced in the next section.

The main objective of this chapter is to present the working principle of ferroelectric materials and try to implement the negative capacitance in the developed GaN model to study how this unique material can improve the DC performance of the device.

5.2 Ferroelectric Dynamics

Ferroelectricity describes a non-linear dielectric behavior and is characterized by a permanent reorientable polarization [75]. As introduced in Chapter 1, crystal possessing a permanent dipole, that is often referred to as spontaneous polarization, are classified as pyroelectrics. Ferroelectricity is defined as a crystal property where a permanent dipole can be reoriented with an applied electric field. Because ferroelectric crystal must have a permanent dipole, every ferroelectric is therefore also a pyroelectric and every pyroelectric is also a piezoelectric [76]. Figure 5.2 shows this subgroup-relation.

The distinguishing characteristic of ferroelectric crystal from all other pyroelectric crystals is the reorientability of the dipole moment. For example, AlN is a pyroelectric material, but under the application of an electric field opposing the dipole direction, it will undergo dielectric breakdown prior to the switching of the polarization to the opposite direction. There are no definitive crystallographic considerations distinguishing ferroelectrics from pyroelectrics; the only difference lies in the ability of the permanent dipole to be reoriented with an electric field less than the dielectric breakdown field [75].

The ferroelectric response is typically characterized by measuring the polarization response to the electric field. This response is a hysteresis loop. A typical

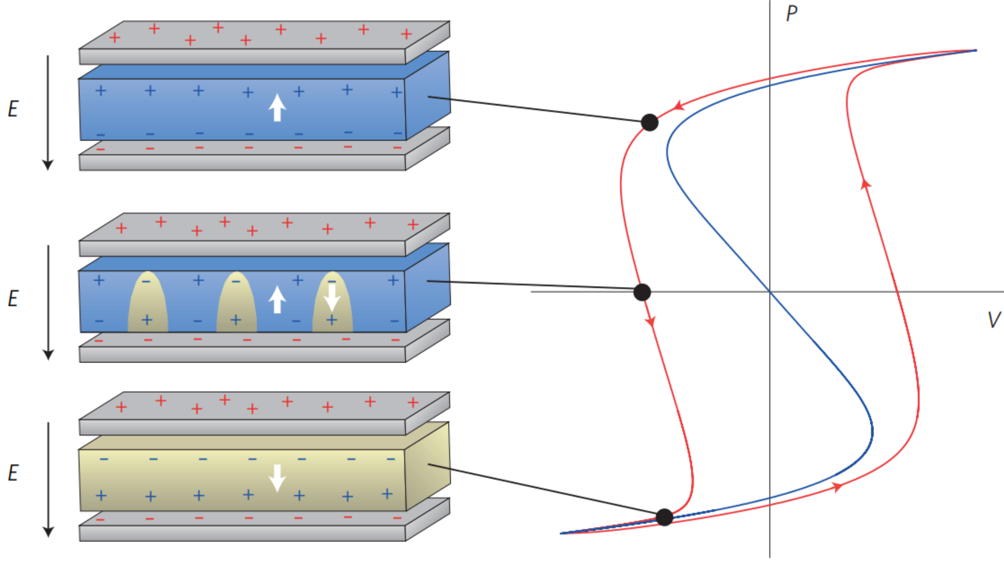

Figure 5.3: Typical ferroelectric hysteresis loop in Metal-Ferroelectric-Metal (MFM) structure. Left: instantaneous distribution of charge in the electrodes (grey) and in the ferroelectric during polarization reversal. White and black arrows indicate the polarization direction and the direction of the electric field respectively. Right: correlation between these charge distributions and different point of the hysteresis loop in the polarization vs voltage (P-V) characteristic.

example is provided in figure 5.3 alongside the relative polarization direction and the direction of the electric field [70].

5.2.1 Landau-Khalatnikov Model

A phenomenological approach to describe the dielectric behavior of ferroelectric starts from equation 5.6 by L. D. Landau and I. M. Khalatnikov:

$$\rho \frac{dP}{dt} = -\frac{dU}{dP} \tag{5.6}$$

where P (C/cm^2) is the polarization, $\rho > 0$ is the frictional inertia of the system that account for dissipative processes during the ferroelectric switching [69] and U (eV) is a series expansion of the free energy of the ferroelectric material that can be written as:

$$U = \left(\frac{\alpha_0}{2}\right)P^2 + \left(\frac{\beta_0}{4}\right)P^4 + \left(\frac{\gamma_0}{6}\right)P^6 - P\mathscr{E}_F \tag{5.7}$$

where $\mathscr{E}_F$ is the electric field across the FE and α_0, β_0 and γ_0 are anisotropy constants [74]. By minimizing the free energy with respect to the polarization, one obtains an expression for the eletric field parallel to the polarization:

$$\frac{dU}{dP} = 0 \longrightarrow \mathscr{E}_{F0} = \alpha_0 P + \beta_0 P^3 + \gamma_0 P^5 \tag{5.8}$$

that leads to:

$$\mathscr{E}_F = \alpha_0 P + \beta_0 P^3 + \gamma_0 P^5 + \rho \frac{dP}{dt} \tag{5.9}$$

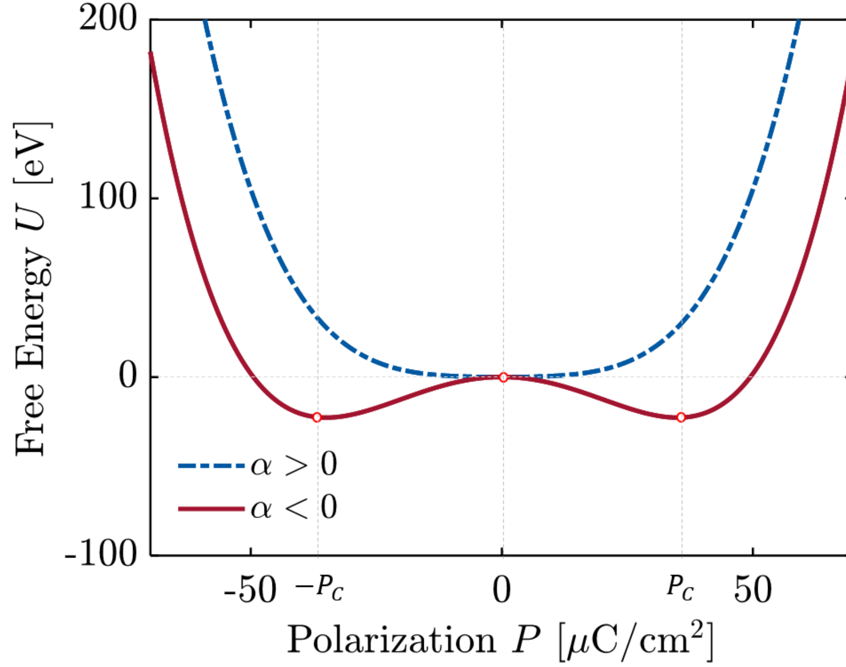

Figure 5.4: Calculated polarization dependence of free energy. If $\alpha_0 > 0$, the lowest free energy state is for zero polarization. If $\alpha_0 < 0$, there are two non-zero lowest free energy states that corresponds to the coercive polarization $\pm P_C$.

Equation 5.7 and 5.9 can be utilized to do some considerations about the stability of the system. For simplicity, the contribution of the fifth order term is neglected ($\gamma_0 = 0$) and β_0 is positive. In figure 5.4 is shown that the polarization dependence of the free energy differs dramatically respect to the sign of α_0. When $\alpha_0 > 0$ the lowest free energy state is for zero polarization. If $\alpha_0 < 0$ there are two minimum free energy states with non-zero polarization. In figure 5.5, is plotted the corresponding electric field $\mathscr{E}_F$ vs the polarization which result in the typical S shaped characteristic.

Since the Negative capacitance is given by the negative slope of the S curve, obtained in the interval $-P_c < P < P_c$ where P_c is called Coercive Polarization, figure 5.5 shows that, to have the desired behaviour, α_0 has to be negative. This condition is not always true, in fact the value of α_0 changes linearly with the temperature as we will discuss in the next subsection. Finally, in figure 5.6 the polarization in the ferroelectric is plotted vs his derivative over time dP/dt (supposing the electric field $\mathscr{E}_F = 0$). The figure shows that $dP/dt = 0$ at three different values:

a) $P = P_R$ b) $P = 0$ c) $P = -P_R$

where P_R is called Remnant Polarization. At $P \pm P_R$, if a small perturbation increase (decrease) the polarization, dP/dt becomes negative (positive), which pushes P back to the starting point. This means that $P = \pm P_R$ are dynamically stable solutions of 5.9. This situation is illustrated by the convergent arrows around $P = \pm P_R$. On the other hand, at $P = 0$, if a small perturbation increase (decrease) the polarization, dP/dt becomes negative (positive), which pushes P away until it reaches the dynamically stable points $P = \pm P_R$. This situation is illustrated by the divergent arrows at $P = 0$.

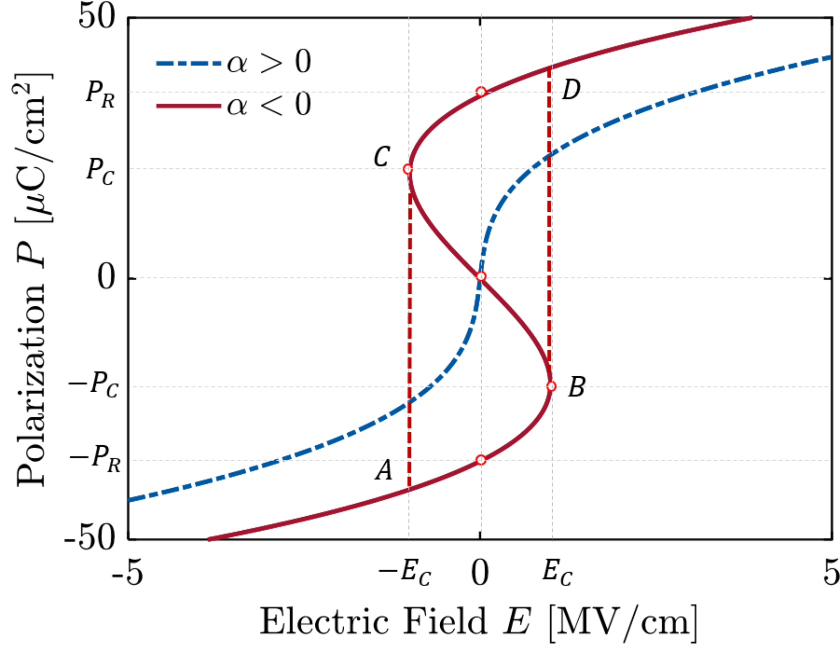

Figure 5.5: Polarization as a function of the electric field. If $\alpha_0 > 0$ the capacitance is always positive. The negative slopes of the S curve when $\alpha_0 < 0$ results in a negative capacitance. The scheme A-B-C-D represent the unstable hysteresis-free path. The conventionally observed includes in the scheme A-B-D-C, which includes the hysteresis.

To put this in perspective, the above-mentioned analysis of the stability of a ferroelectric material shows that the negative capacitance state is not stable in an isolated FE capacitor. For this reason, it is really difficult to experimentally capture this phenomenon. The only way to stabilize the ferroelectric is to put it in series with a dielectric so that (supposing the same thickness to simplify) the total electric field is:

$$\begin{aligned}\mathscr{E}_T &= \mathscr{E}_{DE} + \mathscr{E}_F \\ &= \left(\frac{1}{\varepsilon} + \alpha_0\right) P + \beta_0 P^3 + \gamma_0 P^5 + \rho \frac{dP}{dt}\end{aligned}$$

If $1/\varepsilon + \alpha_0 > 0$ than the ferroelectric is stabilized. In order to use the negative capacity to improve the performance of the device in VLSI, the ferroelectric material is deposited under the gate of the device in series with the capacity given by the oxide. It is therefore important to carefully design the thickness of such layer in order to have a stable system [77].

To plot figure 5.4, 5.5 and 5.6 the value of α_0 and β_0 has been extracted from experimental data. In these calculations we assumed a coercive electric field $\mathscr{E}_C = 1$ MV/cm and a Remnant polarization $P_R = 35$ μC/cm^2. Based on these parameters, the anisotropic constants are calculated using the following procedure.

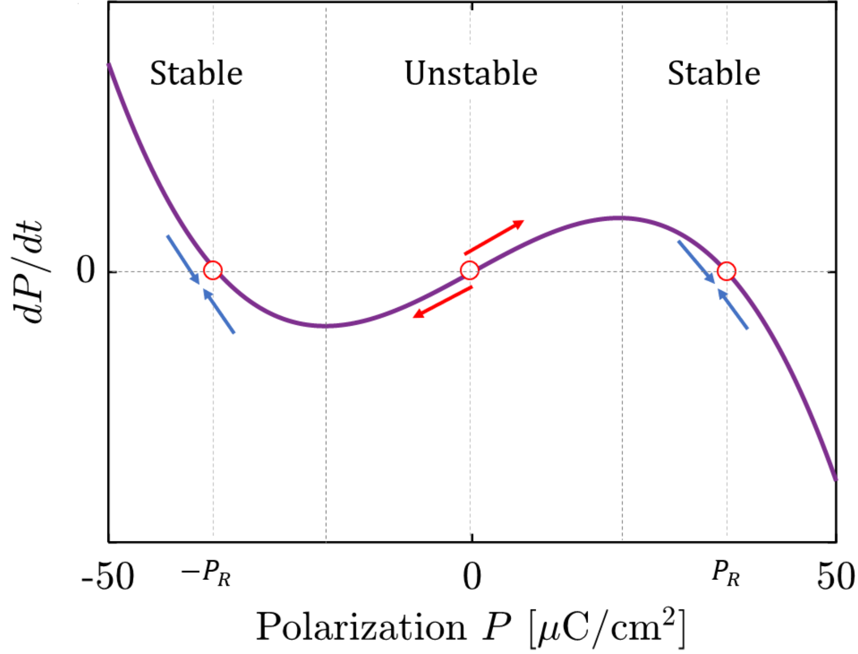

Figure 5.6: dP/dt as a function of the polarization. The system is stable when $P = \pm P_R$ and unstable if $P = 0$. From figure 5.5 is possible to see that the instability occur when the ferroelectric is in the negative capacitance condition.

Procedure for Extraction of the Anisotropic Constants

In figure 5.5, it is shown that the electric field is equal to zero when $P = 0$ and $P = P_R$. In this condition, equation 5.8 leads to the following relations:

$$0 = \alpha_0 P_R + \beta_0 P_R^3 \Longrightarrow P_R = \pm\sqrt{-\frac{\alpha_0}{\beta_0}} \tag{5.10}$$

Differentiating both sides of equation 5.8 with respect to P, the following relation is obtained:

$$\frac{d\mathscr{E}_F}{dP} = \alpha_0 + 3\beta_0 P^2$$

From figure 5.5, we can see that at $\mathscr{E}_F = \mathscr{E}_C$, $d\mathscr{E}_F/dP = 0$ and $P = -P_C$:

$$0 = \alpha_0 + 3\beta P_C^2 \Longrightarrow P_C = \sqrt{-\frac{\alpha_0}{3\beta_0}}$$

that leads to the following relation with the coercive electric field:

$$-\alpha_0 P_C - \beta_0 P^3 = \mathscr{E}_C = -2\alpha_0\sqrt{-\frac{\alpha_0}{3\beta_0}} \tag{5.11}$$

Solving equations 5.10 and 5.11 with respect to α_0 and β_0, the following relations are obtained:

$$\alpha_0 = -\frac{3\sqrt{3}}{2}\cdot\frac{\mathscr{E}_C}{P_R} \qquad \beta_0 = \frac{3\sqrt{3}}{2}\cdot\frac{\mathscr{E}_C}{P_R^3} \tag{5.12}$$

In [78], it is shown how to extract the coefficients taking into account also the fifth order term γ_0. In this case the required information from the experimental data

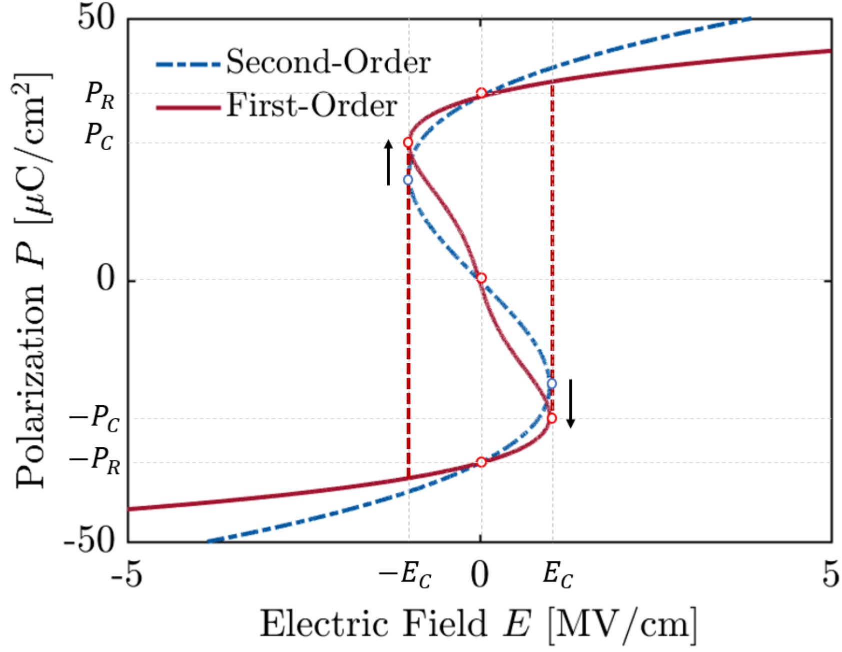

Figure 5.7: Polarization as a function of the electric field in a first-order transition with $P_R = 35$ μC/cm^2, $P_C = 36$ μC/cm^2, $\mathscr{E}_C = 1$ MV/cm compared with the relative second-order transition. The hysteresis loop is almost the same so they cannot be distinguished easily from the experimental data.

are: the Riemman polarization P_R, the coercive electric field $\mathscr{E}_C$ and the coercive polarization P_C. Comparing 5.12 and 5.13, it is easy to see that they coincide if $r_p = \sqrt{3}$.

$$\alpha_0 = -\frac{\mathscr{E}_C}{P_C} \cdot \frac{r_p^2(3r_p^2 - 5)}{2(r_p^2 - 1)^2} \qquad \beta_0 = \frac{\mathscr{E}_C}{P_C^3} \cdot \frac{r_p^4 - 5}{2(r_p^2 - 1)^2}$$
$$\gamma_0 = -\frac{\mathscr{E}_C}{P_C^5} \cdot \frac{r_p^2 - 3}{2(r_p^2 - 1)^2} \qquad \text{where} \quad r_p = \frac{P_R}{P_C} \tag{5.13}$$

In this more general case where we are considering also the fifth order coefficient, it is possible to study the phase transition of different order polar materials as we can see in the next section.

5.2.2 Temperature Dependence

The phase transition of polar materials can be categorized into two different orders: the first order and the second order [77] depending on the value of the anisotropic coefficients:

- $\gamma_0 \approx 0$ and $\beta_0 > 0 \longrightarrow$ second-order transition
- $\gamma_0 > 0$ and $\beta_0 < 0 \longrightarrow$ first-order transition

Figure 5.5 shows an example of second-order phase transition from non-polar phase to polar phase. However, many ferroelectric materials undergo first-order phase

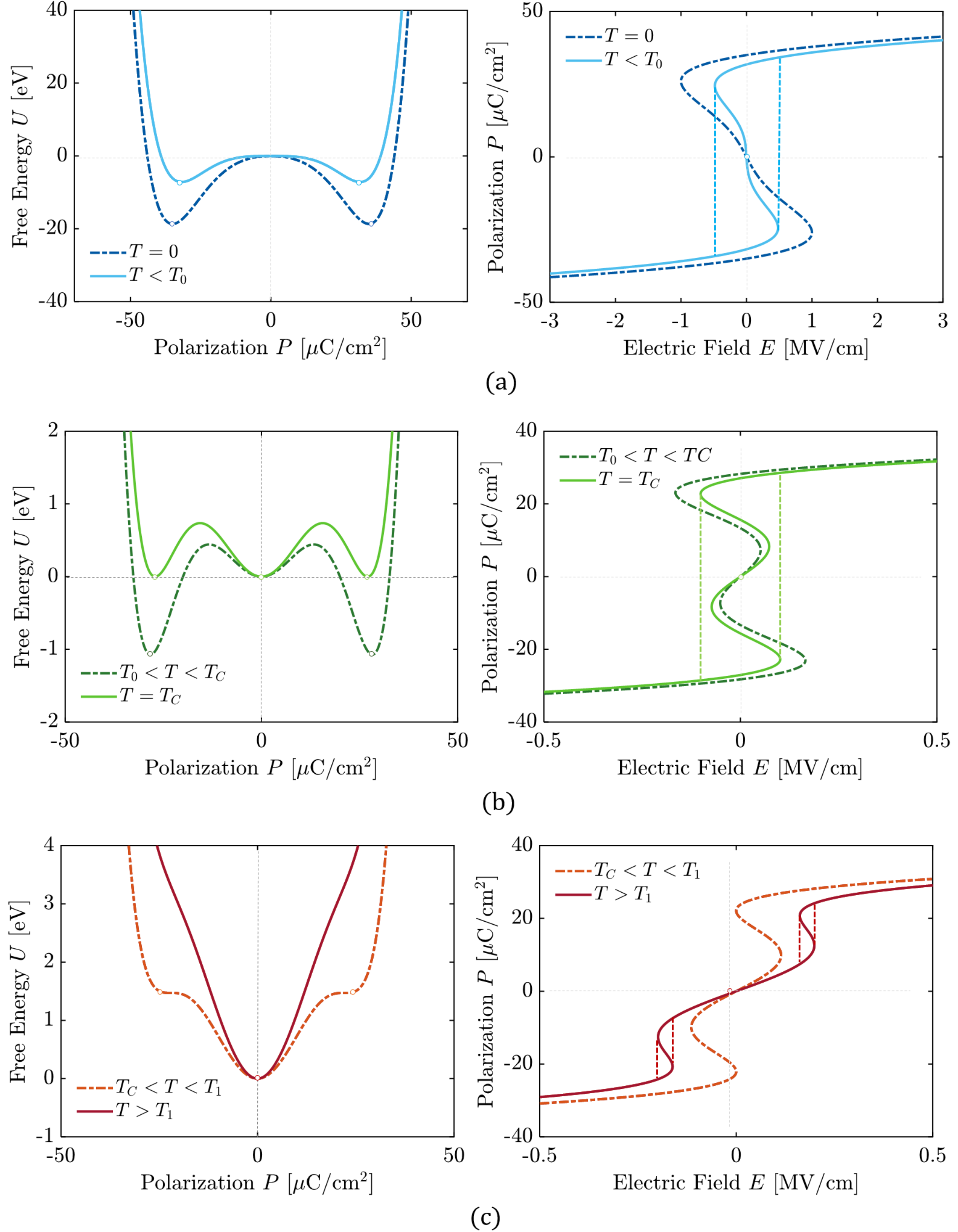

Figure 5.8: First-order phase transition with varying temperature.

transition. The phenomenological theory described by the L-K equations can account for this as well. To do so, the fifth order term γ_0 must be taken into account.

The main difference between the two behaviors is in the number of independent variables that we use. In case of first-order transition ($\gamma_0 > 0$), there are three independent variables: P_R, $\mathscr{E}_C$ and P_C. In case of the second-order transition ($\gamma_0 \approx 0$), there are two independent variables: P_R and $\mathscr{E}_C$. This means that the coercive polarization cannot be controlled and so $P_C = P_R/\sqrt{3}$. In the example of figure 5.5, $P_C \sim 20\ \mu\text{C/cm}^2$. In figure 5.7 are compared the P-$\mathscr{E}$ curves using the same $P_R = 35$,

μC/cm^2 and $\mathscr{E}_C$ = 1 MV/cm. For the first-order phase transition the coercive polarization is forced to be P_C = 26 μC/cm^2 instead of P_C = 20 μC/cm^2. This small difference, though ostensibly trivial, will dramatically impact the study of the temperature dependence.

The temperature dependence of the dielectric behavior results from the assumption that the coefficient α depends linearly with the temperature while β_0 and γ_0 are temperature-independent coefficients [76]:

$$\alpha_{T0} = \alpha_0 \left(1 - \frac{T}{T_0}\right)$$

where T_0 is the Curie-Weiss temperature. Equation 5.7 can be rewritten taking into account this effect:

$$U = \left(\frac{\alpha_{T0}}{2}\right) P^2 + \left(\frac{\beta_0}{4}\right) P^4 + \left(\frac{\gamma_0}{6}\right) P^6 - P\mathscr{E}_{FT} \tag{5.14}$$

and then

$$\mathscr{E}_F = \alpha_{T0} P + \beta_0 P^3 + \gamma_0 P^5 + \rho \frac{dP}{dt} \tag{5.15}$$

In case of second-order phase transition, if the temperature $T > T_0$, α_{T0} becomes positive and the material loses its ferroelectric property since the ferroelectric phase can never be induced by applying an electric field. In this condition, the characteristic of the polarization vs the free energy and the electric field is similar to the blue line in figure 5.4 and 5.5. The free energy presents one global minima at $P = 0$ and the P-$\mathscr{E}$ has always positive slope.

In case of first-order transition, the situation is dramatically different. Below the Curie-Weiss temperature T_0, the free energy presents two global minima and a characteristic single hysteresis (see figure 5.8a). Above T_0 three local minimums can be observed. However the shape of the P-$\mathscr{E}$ curve is still a single hysteresis (see figure 5.8b). Above the critical Curie temperature T_C, the P-$\mathscr{E}$ characteristic changes, showing the so called "broken hysteresis". The effect becomes more evident if the temperature goes beyond the limit temperature of ferroelectric (T_1). In this condition, the ferroelectric has two negative slopes mediated by a non-polar phase (see figure 5.8c).

Finally, if the temperature is still increased above the limit temperature of the field-induced ferroelectric properties (T_2), the ferroelectric phase can never be induced by applying an electric field. As result, no hysteresis is present beyond T_2. From equation 5.14, T_C, T_1 and T_2 can be formulated as [79].

$$T_C = T_0 \cdot \left(1 + \frac{3}{16} \frac{\beta_0^2}{|\alpha_0 \gamma_0|}\right)$$

$$T_1 = T_0 \cdot \left(1 + \frac{1}{4} \frac{\beta_0^2}{|\alpha_0 \gamma_0|}\right)$$

$$T_2 = T_0 \cdot \left(1 + \frac{9}{20} \frac{\beta_0^2}{|\alpha_0 \gamma_0|}\right)$$

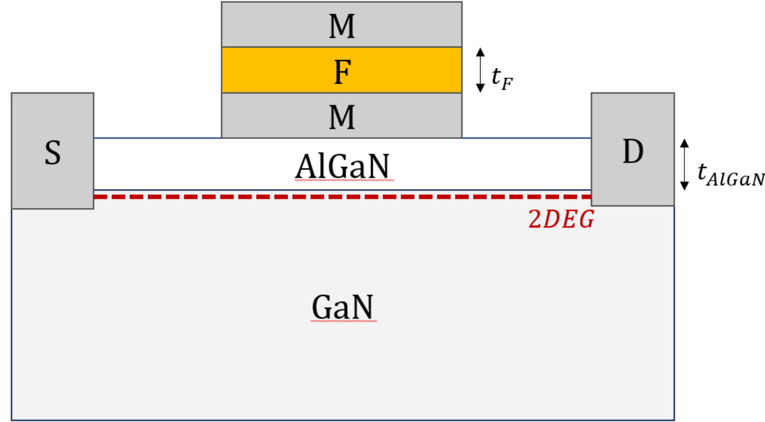

Figure 5.9: Cross-section of the MFMIS structure discussed in this chapter where the ferroelectric material is deposited under the gate of a Schottky HEMT device.

5.3 Device Implementation

It is easy to see that if we set $Q_F = P \cdot A_F$ and $V_F = \mathscr{E}_F t_F$, where t_F is the thickness and A_F is the area of the ferroelectric, equation 5.9 leads to an expression for the voltage across the ferroelectric capacitor [73]:

$$V_F = \alpha_T Q_F + \beta Q_F^3 + \gamma Q_F^5 + \rho \frac{dQ_F}{dt} \tag{5.16}$$

with the anisotropic constants:

$$\alpha_T = t_F \cdot \frac{\alpha_{T0}}{A_F} \quad , \quad \beta = t_F \cdot \frac{\beta_0}{A_F} \quad \text{and} \quad \gamma = t_F \cdot \frac{\gamma_0}{A_F}$$

From equation 5.16 is possible to express the corresponding FE non-linear capacitance as:

$$C_F = \left(\frac{dV_F}{dQ_F} \right)^{-1} = \frac{1}{\alpha_T + 3\beta Q_F^2 + 5\gamma Q_F^4} \tag{5.17}$$

Using equation 5.17, the voltage drop across the ferroelectric can be rewritten as:

$$V_F = \int_0^{Q_F} \frac{1}{C_F} dQ + \rho \frac{dQ_F}{dt} \tag{5.18}$$

demonstrating that the equivalent circuit for a ferroelectric capacitor consists of an internal resistor ρ in series with a non-linear capacitor C_F dependent from the charge in the ferroelectric.

5.3.1 Modeling NC-GaN HEMT

The concept of NCFET was first proposed in 2008 by S. Salahuddin and S. Datta [73]; gradually it gained popularity due to its remarkable characteristics. NCFET has the same structure as the MOSFET except that a ferroelectric thin layer is deposited at the top of the gate insulator. If deposited under the gate of a transistor, the Metal-Ferroelectric-Metal-Insulator-Semiconductor (MFMIS) structure

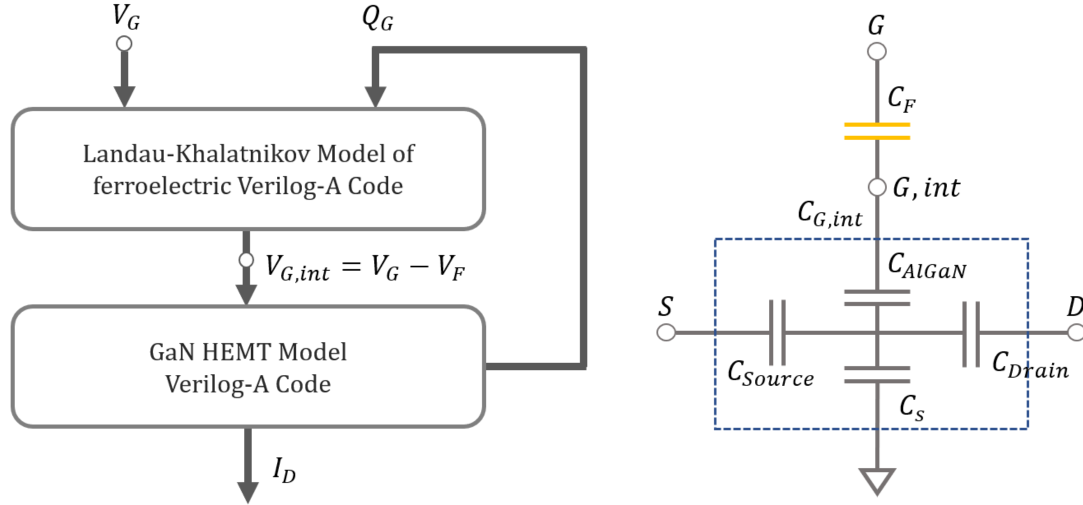

Figure 5.10: Modeling flow-chart implemented in Verilog-A and used to simulate the NC-GaN HEMT. The GaN model is based on the experimental data of the non-irradiated Schottky HEMT studied in Chapter 3.

(see figure 5.9) can be equivalently represented by two circuit components: the ferroelectric capacitance C_F and the internal gate capacitance $C_{G,int}$. The purpose of the intermediate metallic layer is to average out the non-uniform potential profile along the source-drain direction and any charge non-uniformity, thereby, making the single-domain Landau-Khalatnikov based description of the system a valid one.

A negative value of C_F results in a voltage amplification at the internal gate, and can be expressed through the following equation [80]:

$$A_V = \frac{V_{G,int}}{V_G} = \frac{|C_F|}{|C_F| - C_{G,int}} \tag{5.19}$$

where the ferroelectric capacitance is expressed in equation 5.17 and $C_{G,int}$ is the series of the surface capacitance C_s and the insulator capacitance which is C_{ox} in case of MOSFET and C_{AlGaN} in case of GaN HEMT. This internal voltage amplification will results in higher ON current at the same applied voltage [81].

The internal positive capacitance has the important role to keep the NC state stable, as discussed previously in the chapter. This is true only if the total gate capacitance $C_G = (C_{G,int}^{-1} + C_F^{-1})^{-1}$ is positive. This condition implies that $|C_F| > C_{G,int}$ to realize a thermodynamically stable NC state. At the same time, the effect of the amplification will be greater, the more $(|C_F| - C_{G,int}) \ll 1$. Keeping $C_{G,int}$ constant, it is easy to understand that the impact of the ferroelectric can be engineered changing the thickness of that layer (and the value of the corresponding capacitance $C_F = \varepsilon_F / t_F$).

Since $|C_F| > C_{G,int}$ ensures the condition of no hysteresis [81], the simulation has been conducted in the quasi-static domain. In this scenario, the dynamic term dQ_F/dt of equation 5.16 can be ignored. Furthermore, we assume $Q_F = Q_G$ since the ferroelectric is in series with the gate capacitance. It is important to emphasize that the primary purpose of this study is to show the impact of the negative capacitance in GaN HEMT devices to provide comprehensive insight into the physics

behind the electrical behaviour and the model is not specifically dependent on the ferroelectric material and set the relative of parameters α_0, β_0, γ_0 and T_0 chosen. To put this study into perspective, the GaN HEMT model has been calibrated with the experimental data of the non-irradiated Schottky HEMT studied in Chapter 3. The anisotropic constants are the same used by U. Radhakrishna in the Manual: MVSNC model [82] where the ferroelectric in a second-order phase transition material implemented under the gate of a MOSFET.

To model the NC-GaN HEMT we follow the same strategy used in Chapter 4 to implement the p-GaN layer under the gate. From the voltage balance condition we get:

$$\begin{aligned} V_G &= V_F + V_{TH} + V_{AlGaN} + \psi_s \\ &= \alpha Q_G + \beta^3 Q_G + \gamma^5 Q_G^5 + V_{TH} + V_{AlGaN} + \psi_s \end{aligned} \tag{5.20}$$

where V_{TH} is the threshold voltage, $V_{AlGAN} = qn_s/C_{AlGAN}$ and ψ_s is the surface potential. Q_G in terms of surface potential can be expressed as:

$$Q_G = \int_{\psi_S}^{\psi_D} LWC_{AlGaN} \cdot \frac{(V_{G0}-\psi)(V_{G0}-\psi+V_T)}{(V_{G0}-\psi_m+V_T)(\psi_D-\psi_S)} d\psi \tag{5.21}$$

(see equation 2.30 in Chapter 2 for more details). Now ψ_s can be substituted from equation 5.20 in 5.21 to obtain Q_G as a function of V_F for a given value of V_G. Figure 5.10, showns the modeling flow-chart implemented in Verilog-A which is used to solve the system of equation in order to obtain the drain current (I_D) of the NC-GaN HEMT.

Simulation Results

The key to study the impact of the ferroelectric layer is in the internal voltage amplification defined in equation 5.19 which is related to the difference between the ferroelectric and internal capacitance:

$$|C_F| - C_{ins} = \frac{|\varepsilon_F|}{t_F} - \left(\frac{t_{AlGaN}}{\varepsilon_{AlGaN}} + \frac{1}{C_s}\right)^{-1}$$

Keeping the thickness of the AlGaN constant, the matching between the two capacitance can be increased varying the thickness of the ferroelectric. figure 6.11 and 6.12 show the results of the simulations while implementing the Verilog-A code in the ADS software. Figure 5.12a represents the internal node amplification.

It is clear that with the increase of the thickness, there is an increase in the matching between the two series capacitance which consequently increases the voltage amplification of the internal note (see equation 5.19). This continues until the thickness reaches a critical limit until the condition ($|C_F| > C_{G,int}$) is no longer true and the system becomes unstable. Figures 5.12a,b,c,d,e,f show that A_V can lead to a significant increase of the drain current current improving the DC performance of the device such as ON current, transconductance and drain conductance.

In the best case, which corresponds to a thickness of the ferroelectric layer t_F = 60 nm, the simulation shows a voltage amplification of the internal node $A_V = 3$ tripling the value of the transconductance compared to the normal Schottky HEMT

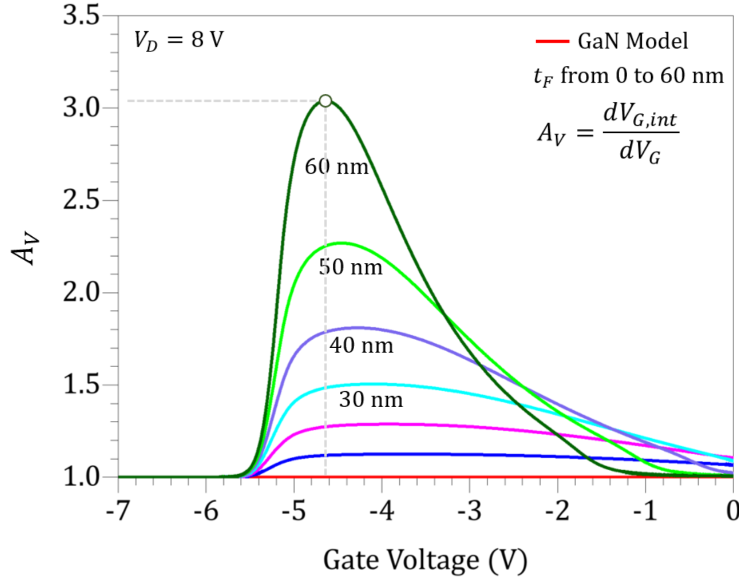

Figure 5.11: Impact of variation of the ferroelectric thickness on the voltage amplification of the internal node.

(see figure 5.12c). From the I_D-V_G characteristic in linear scale (see figure 5.12a), we can observe that under the effect of negative capacitance the same drain current, at $V_G = -2$ V, can be reached at $V_G = -4$ V and the same drain current, at $V_G = 0$ V, can be reached at $V_G = -3$ V where the threshold of the device is $V_{TH} = -4.9$. From the I_D-V_G characteristic in logarithmic scale (figure 5.12b) we see that the sub-threshold slope is decreased by 25% where the ON current is now fourfold.

In figure 5.12e and 5.12f are plotted the I_D-V_D and drain conductance respectively. Both are significantly increased. In particular we can observe that the I_D-V_D at $V_G = -4$ is now almost bigger than the I_D-V_D at $V_G = -2$ of the normal Schottky HEMT. All these improvements are consistent with the studies conducted on the NCFET showing that the negative capacitance can be used to improve the performances of GaN devices.

Finally, to conclude our study we take into account the impact of the variation of the ferroelectric temperature, keeping in mind that the material has a second-order phase transition. This means that (taking as reference figure 5.5), with the increase of the temperature, the negative capacitance decreases. When the temperature is higher than the Curie-Weiss the S curve is folded to such a point that the ferroelectric loses its negative slope resulting in a positive capacitance causing the voltage amplification of the internal node to be $A_V < 1$ and leading to the collapse of the drain current. Figure 5.13a shows the impact of the variation of the ferroelectric temperature in the voltage amplification of the internal node.

The results of the simulation is consistent with the theory. With the rise of the temperature, the DC performances of the device start decreasing. At $\Delta T > T_0$ the ferroelectric capacitance is positive and the gain becomes $A_V < 1$ leading to a collapse of the drain current (in figure 5.13b the I_D-V_G is plotted as example).

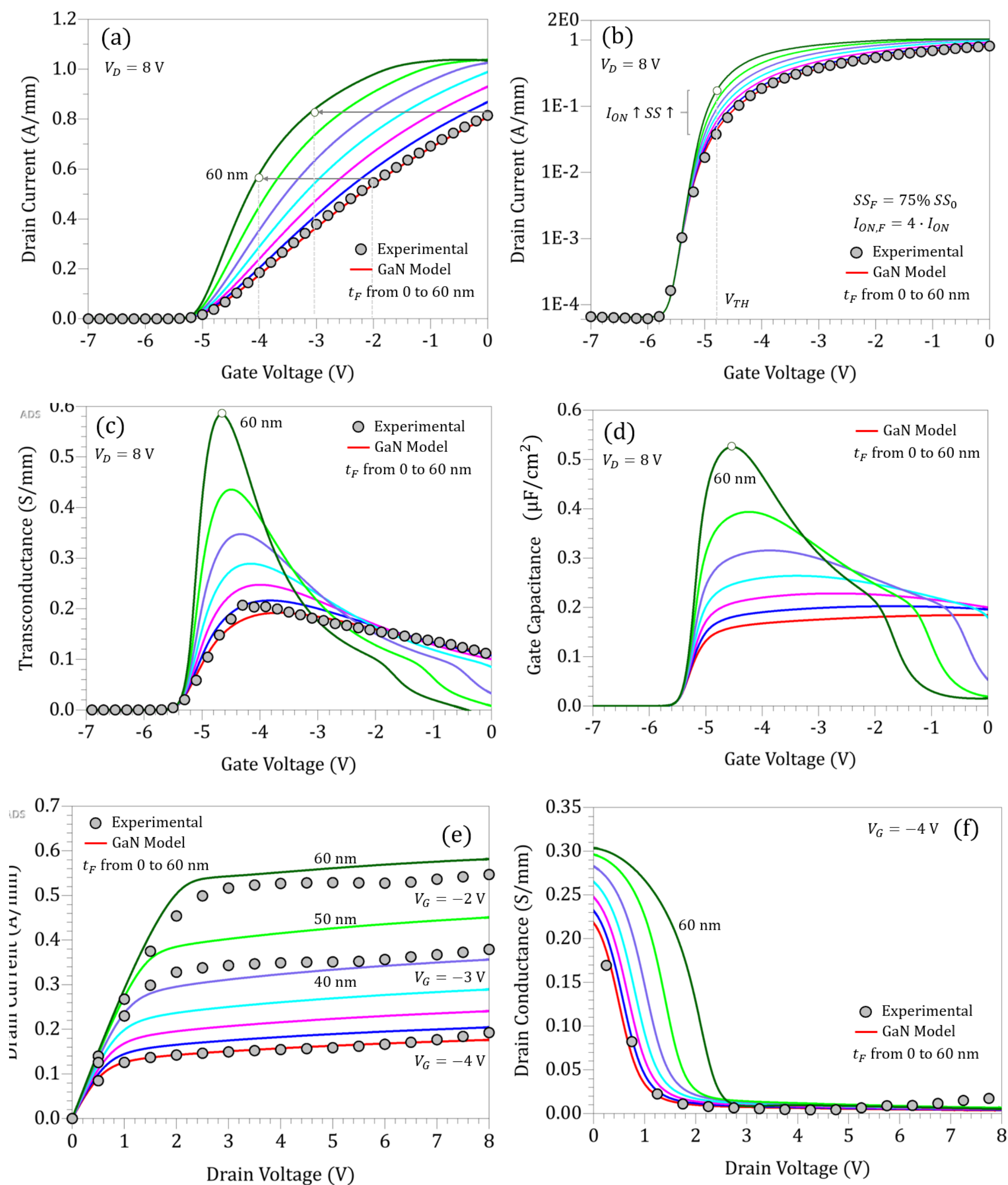

Figure 5.12: Impact of variation of the ferroelectric thickness on the DC performance of GaN HEMT. All the DC performances are significantly increased. In order are plotted: (a) I_D-V_G linear scale, (b) I_D-V_G log scale, (c) transconductance, (d) gate capacitance, (e) I_D-V_D and (f) drain conductance.

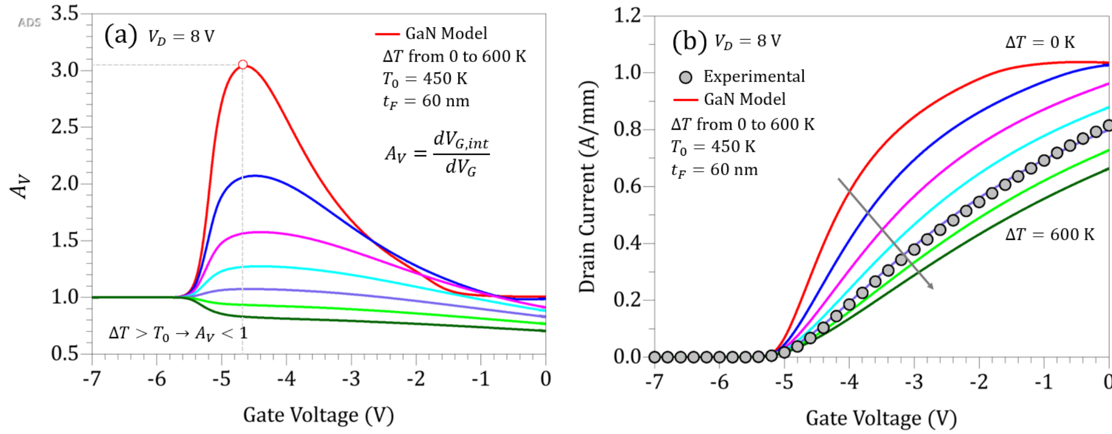

Figure 5.13: Impact of the variation of the temperature in the DC performance of NC-GaN HEMT.

5.4 Conclusion

In this chapter the ferroelectric concept and the main reasons that makes it a good candidate for the improvement of the performance of GaN HEMT devices has been presented. Following the phenomenological approach described by the Landau-Khalatnikov equations we studied the physics of such material presenting a method for the extraction of the anisotropic constants. Depending from the value of these parameters we defined two types of phase transition of polar materials: 1st order phase 2nd order phase. Following that, we studied the temperature dependence of the material.

Finally, the ferroelectric theory has been used to implement the ferroelectric layer under the gate of our developed GaN HEMT. The GaN Model has been calibrated with the non-irradiated Schottky HEMT studied in Chapter 3. The result is consistent with the studies conducted on the NCFET [80, 83, 84, 82] where the MFMIS structure shows higher ON-current, and transconductance.

Conclusion and Future Work

Conclusion

Despite the recent commercial success of GaN-based HEMT devices, internal physical mechanisms are often not completely understood. Sophisticated theories and physic-based compact models have been developed for previous generations of semiconductor devices. However, the unique properties of nitrides present a challenge.

This thesis explores the nature of gallium nitride from the point of view of compact modeling paying particular attention to power electronic applications. Different structures are taken into account along this study: from the simple Schottky HEMT structure, to the MIS-HEMT and p-GaN HEMT. To model the behaviour of such devices, in Chapter 2, the physics of the typical AlGaN/GaN Schottky HEMT is studied by solving the Schrödinger's and Poisson's equations in order to have a unified and accurate definition of the Fermi level and 2DEG charge. The developed GaN model is then implemented using Verilog-A in the electronic design automation software Advanced Design System (ADS) by Keysight EEsof EDA.

The physical-based nature of the developed model can provide an insightful understanding of the device characteristics. For this reason, in Chapter 3 after a brief introduction about the main effects of γ-radiation on GaN-based devices, we study the origin of the induced degradation with the help of the developed GaN model. To do so we analyze the γ-ray effect of the fabricated GaN HEMT using two approaches. First, the analysis of the effect of radiation in GaN-based HEMT is carried out through electrical and material characterization of the devices subjected to different doses of γ-ray. In the second part the physical-based GaN modeling is used to help our understanding of the measurement results and point the leading factor in the induced degradation.

Since the developed GaN model is able to reproduce only the behaviour of the typical AlGaN/GaN Schottky HEMT, Chapter 4 proposes a novel approach to study the effects of the p-GaN layer under the gate in the p-GaN/AlGaN/GaN structure which is becoming widely used for power electronics applications thanks to its normally-off characteristic and good reliability. To the best of the knowledge of the author this is the first time a physical-based compact model includes such structure. In order to verify the model, it has been implemented using Verilog-A in the ADS software and the simulation results has been compared with the experimental data obtained from four devices showing excellent agreement.

Finally, in Chapter 5, inspired by the method used to include the p-GaN layer under the gate, and aware of the results that ferroelectric materials are showing in the rising NCFET technology, we studied the physics of such material following the phenomenological approach described by the Landau-Khalatnikov equations. The ferroelectric material has been implemented in the AlGaN/GaN model showing

that the amplification of the internal node can lead to a significant increase of the drain current improving the DC performance of the device such as ON current, transconductance and drain conductance.

Future Work

Several aspects presented in this Thesis are worth further investigation at the conclusion of this project. First of all the Schottky HEMT model presented in Chapter 2 is not complete. Different real device effects should be taken into account such as gate leakage, self heating effect, trapping. The simulations has always been conducted in DC because we didn't have the measurement equipment to characterize the device in AC. This is an other aspect that could be explored. Furthermore, the model should include field-plates since they are widely used to increase the breakdown voltage of GaN HEMTs.

Regarding Chapter 4 the developed p-GaN/AlGaN/GaN structure should include different real device effects such as interfacial charge and gate leakage. The latter has always been studied using two back diodes: a reverse Schottky diode and a PiN diode. Our model offer the advantage that the voltage drop, the thickness of the depletion region and the electric field in each layer of the structure are well defined thanks to the solution of the Schrödinger's and Poisson's equations. In this way modeling the gate leakage becomes more precise offering a new perspective in the understanding of this effect, which is still controversial.

Finally, Chapter 5 offers a good starting point to understand how ferroelectric materials can lead to an improvement of the performances of GaN-based devices. Even if the theory of ferroelectric material is well defined, different aspects are still not completely understood such as the multidomain structure of ferroelectric materials. Furthermore, the simulation has been conducted under the assumption of quasi-static domain, completely ignoring the important effect introduced by the hysteretic nature of this material. Regarding the implementation of the ferroelectric layer in the AlGaN/GaN structure, it is important to clarify that this study is purely theoretical and even if the results are consistent with the studies conducted in NCFET, it needs to be verified comparing the simulation with the experimental data measured on a fabricated device.

Bibliography

[1] Y.S. Chauhan et al. *FinFET Modeling for IC Simulation and Design: Using the BSIM-CMG Standard*. Elsevier Science, 2015. ISBN: 9780124200852. URL: https://books.google.com.tw/books?id=nXGDBAAAQBAJ.

[2] U. Mishra and J. Singh. *Semiconductor Device Physics and Design*. Series on Integrated Circuits and Systems. Springer Netherlands, 2007. ISBN: 9781402064807. URL: https://books.google.com.tw/books?id=6NAtk7zr3n4C.

[3] J. Piprek. *Nitride Semiconductor Devices: Principles and Simulation*. Wiley, 2007. ISBN: 9783527610716. URL: https://books.google.com.tw/books?id=iDiGR5Un5xoC.

[4] R.S. Muller and T.I. Kamins. *Device Electronics for Integrated Circuits*. Wiley, 2002. ISBN: 9780471593980. URL: https://books.google.com.tw/books?id=G-dhQgAACAAJ.

[5] E.F. Schubert. *Physical Foundations of Solid-State Devices*. E. Fred Schubert, 2015. ISBN: 9780986382628. URL: https://books.google.com.tw/books?id=l5gSBwAAQBAJ.

[6] U.K. Mishra et al. "GaN-Based RF power devices and amplifiers". In: *Proceedings of the IEEE* 96 (Mar. 2008), pp. 287–305. DOI: 10.1109/JPROC.2007.911060.

[7] E O. Johnson. "Physical limitations on frequency and power parameters of transistors". In: *RCA Rev* 26 (Apr. 1965), pp. 27–34. DOI: 10.1109/IRECON.1965.1147520.

[8] U.K. Mishra, Primit Parikh, and Yifeng Wu. "AlGaN/GaN HEMTs - An overview of device operation and applications". In: *Proceedings of the IEEE* 90 (July 2002), pp. 1022–1031. DOI: 10.1109/JPROC.2002.1021567.

[9] Shuji Nakamura. "GaN growth using GaN Buffer layer". In: *Japanese Journal of Applied Physics* 30 (Oct. 1991), pp. L1705–L1707. DOI: 10.1143/JJAP.30.L1705.

[10] H Amano et al. "Metalorganic vapor phase epitaxial growth of a high quality GaN film using an AlN buffer layer". In: *Applied Physics Letters* 48 (Mar. 1986), pp. 353–355. DOI: 10.1063/1.96549.

[11] Shuji Nakamura, Takashi Mukai, and Masayuki Senoh. "Candela-Class High-Brightness InGaN/AlGaN Double-Heterostructure Blue-Light-Emitting Diodes". In: *Applied Physics Letters* 64 (Apr. 1994), pp. 1687–1689. DOI: 10.1063/1.111832.

[12] Siddha Pimputkar et al. "Prospects for LED lighting". In: *Nature Photonics* 3 (Apr. 2009), pp. 180–182. DOI: 10.1038/nphoton.2009.32.

[13] E.F. Schubert. *Light-Emitting Diodes (3rd Edition)*. E. Fred Schubert, 2018. ISBN: 9780986382666. URL: https://books.google.com.tw/books?id=GEFKDwAAQBAJ.

[14] Dominic King-Smith and David Vanderbilt. "Theory of Polarization of Crystalline Solids". In: *Physical review. B, Condensed matter* 47 (Feb. 1993), pp. 1651–1654. DOI: 10.1103/PhysRevB.47.1651.

[15] L. Vegard. "Die Konstitution der Mischkristalle und die Raumfüllung der Atome". In: *Zeitschrift fur Physik* 5 (Jan. 1921), pp. 17–26. DOI: 10.1007/BF01349680.

[16] Energias Market Research. *Global Gallium Nitride (GaN) Semiconductor Devices Market to Witness a CAGR of 14.2% during 2018-2024*. Oct. 2018. URL: https://www.energiasmarketresearch.com/gallium-nitride-semiconductor-devices-market-size/.

[17] Yole Développement. *Power GaN 2018: Epitaxy, Devices, Applications and Technology Trends*. Dec. 2018. URL: https://www.i-micronews.com/produit/power-gan-2018-epitaxy-devices-applications-and-technology-trends/.

[18] MarketsandMarkets. *GaN Power Device Market - Global Forecast to 2023*. Dec. 2017. URL: https://www.marketsandmarkets.com/Market-Reports/gallium-nitride-wafer-market-93870461.html.

[19] R. Quay. *Gallium Nitride Electronics*. Springer Series in Materials Science. Springer Berlin Heidelberg, 2008. ISBN: 9783540718925. URL: https://books.google.com.tw/books?id=iL%5C_dAR2xyFMC.

[20] Hao Zhang. *Physics Based Virtual Source Compact Model of Gallium-Nitride High Electron Mobility Transistors*. 2017. URL: http://hdl.handle.net/10012/11678.

[21] Sourabh Khandelwal and T.A. Fjeldly. "A physics based compact model of I–V and C–V characteristics in AlGaN/GaN HEMT devices". In: *Solid-State Electronics* 76 (Oct. 2012), pp. 60–66. DOI: 10.1016/j.sse.2012.05.054.

[22] Bing J. Sheu et al. "A compact IGFET charge model". In: *Circuits and Systems, IEEE Transactions on* 31 (Sept. 1984), pp. 745–748. DOI: 10.1109/TCS.1984.1085562.

[23] M.-C Jeng, P.K. Ko, and Chenming hu. "Deep-submicrometer MOSFET model for analog/digital circuit simulations". In: *Technical Digest - International Electron Devices Meeting* (Feb. 1988), pp. 114–117. DOI: 10.1109/IEDM.1988.32766.

[24] W. Liu et al. *BSIM 3v3.2 MOSFET Model Users' Manual*. Tech. rep. UCB/ERL M98/51. EECS Department, University of California, Berkeley, 1998. URL: http://www2.eecs.berkeley.edu/Pubs/TechRpts/1998/3486.html.

[25] Larry Dunleavy et al. "Modeling GaN: Powerful but Challenging". In: *IEEE Microwave Magazine* 11 (2010), pp. 82–96.

[26] I. Angelov, H. Zirath, and N. Rosman. "A new empirical nonlinear model for HEMT and MESFET devices". In: *IEEE Transactions on Microwave Theory and Techniques* 40.12 (Dec. 1992), pp. 2258–2266. DOI: 10.1109/22.179888.

[27] Andrey Kokolov and L I. Babak. “Methodology of built and verification of non-linear EEHEMT model for GaN HEMT transistor”. In: *Radioelectronics and Communications Systems* 58 (Oct. 2015), pp. 435–443. DOI: 10.3103/S0735272715100015.

[28] J. Xu et al. “Dynamic FET model - DynaFET - for GaN transistors from NVNA active source injection measurements”. In: *2014 IEEE MTT-S International Microwave Symposium (IMS2014)* (June 2014), pp. 1–3. DOI: 10.1109/MWSYM.2014.6848293.

[29] X. Cheng and Y. Wang. “A Surface-Potential-Based Compact Model for AlGaN/GaN MODFETs”. In: *IEEE Transactions on Electron Devices* 58.2 (Feb. 2011), pp. 448–454. DOI: 10.1109/TED.2010.2089690.

[30] Ujwal Radhakrishna and Dimitri Antoniadis. “MIT Virtual Source GaN HEMT-High Voltage (MVSG-HV) compact model”. In: (Jan. 2015). DOI: 10.4231/D3086365H.

[31] S. Khandelwal et al. “ASM GaN: Industry Standard Model for GaN RF and Power Devices—Part 1: DC, CV, and RF Model”. In: *IEEE Transactions on Electron Devices* 66.1 (Jan. 2019), pp. 80–86. DOI: 10.1109/TED.2018.2867874.

[32] S. A. Albahrani et al. “ASM GaN: Industry Standard Model for GaN RF and Power Devices—Part-II: Modeling of Charge Trapping”. In: *IEEE Transactions on Electron Devices* 66.1 (Jan. 2019), pp. 87–94. DOI: 10.1109/TED.2018.2868261.

[33] O. Wing. *Gallium Arsenide Digital Circuits*. The Springer International Series in Engineering and Computer Science. Springer US, 2012. ISBN: 9781461315414. URL: https://books.google.com.tw/books?id=i58ACAAAQBAJ.

[34] S. Khandelwal, N. Goyal, and T. A. Fjeldly. “A Physics-Based Analytical Model for 2DEG Charge Density in AlGaN/GaN HEMT Devices”. In: *IEEE Transactions on Electron Devices* 58.10 (Oct. 2011), pp. 3622–3625. DOI: 10.1109/TED.2011.2161314.

[35] S. Khandelwal, Y. S. Chauhan, and T. A. Fjeldly. “Analytical Modeling of Surface-Potential and Intrinsic Charges in AlGaN/GaN HEMT Devices”. In: *IEEE Transactions on Electron Devices* 59.10 (Oct. 2012), pp. 2856–2860. DOI: 10.1109/TED.2012.2209654.

[36] A.S. Householder. *The Numerical Treatment of a Single Nonlinear Equation*. International series in pure and applied mathematics. McGraw-Hill, 1970. URL: https://books.google.com.tw/books?id=yk0UvgEACAAJ.

[37] X Xi et al. *BSIM4.3.0 MOSFET Model - User's Manual*. Jan. 2003.

[38] S. Khandelwal et al. “Analytical modeling of surface-potential and drain current in AlGaAs/GaAs HEMT devices”. In: (Nov. 2012), pp. 183–185. DOI: 10.1109/RFIT.2012.6401654.

[39] S. Khandelwal and T. A. Fjeldly. “A Surface-Potential-Based Compact Model for Study of Non-Linearities in AlGaAs/GaAs HEMTs”. In: (Oct. 2012), pp. 1–4. DOI: 10.1109/CSICS.2012.6340055.

[40] F. M. Yigletu et al. “Compact Charge-Based Physical Models for Current and Capacitances in AlGaN/GaN HEMTs”. In: *IEEE Transactions on Electron Devices* 60.11 (Nov. 2013), pp. 3746–3752. ISSN: 0018-9383. DOI: 10.1109/TED.2013.2283525.

[41] Sudip Ghosh et al. “Modeling of Source/Drain Access Resistances and their Temperature Dependence in GaN HEMTs”. In: (Aug. 2016). DOI: 10.1109/EDSSC.2016.7785254.

[42] G.F. Knoll. *Radiation Detection and Measurement*. John Wiley & Sons, 2010. ISBN: 9780470131480. URL: https://books.google.com.tw/books?id=4vTJ7UDel5IC.

[43] A. Ionascut-Nedelcescu et al. “Radiation hardness of gallium nitride”. In: *IEEE Transactions on Nuclear Science* 49.6 (Dec. 2002), pp. 2733–2738. DOI: 10.1109/TNS.2002.805363.

[44] S J. Pearton et al. “Review—Ionizing Radiation Damage Effects on GaN Devices”. In: *ECS Journal of Solid State Science and Technology* 5 (Jan. 2016), Q35–Q60. DOI: 10.1149/2.0251602jss.

[45] Jonathan Lee et al. “Low dose 60 Co gamma-irradiation effects on electronic carrier transport and DC characteristics of AlGaN/GaN high-electron-mobility transistors”. In: *Radiation Effects and Defects in Solids* 172 (Mar. 2017), pp. 1–7. DOI: 10.1080/10420150.2017.1300903.

[46] Alexander Polyakov et al. “Radiation effects in GaN materials and devices”. In: *J. Mater. Chem. C* 1 (Jan. 2013), pp. 877–887. DOI: 10.1039/C2TC00039C.

[47] M G Ganchenkova and Risto Nieminen. “Nitrogen Vacancies as Major Point Defects in Gallium Nitride”. In: *Physical review letters* 96 (June 2006), p. 196402. DOI: 10.1103/PhysRevLett.96.196402.

[48] Ya-Hsi Hwang et al. “Effect of Gamma Irradiation on DC Performance of Circular-Shaped AlGaN/GaN High Electron Mobility Transistors”. In: *ECS Transactions* 61 (Mar. 2014), pp. 205–210. DOI: 10.1149/06104.0205ecst.

[49] J. T. Moran et al. “The Effects of Temperature and Electron Radiation on the Electrical Properties of AlGaN/GaN HFETs”. In: *IEEE Transactions on Nuclear Science* 56.6 (Dec. 2009), pp. 3223–3228. DOI: 10.1109/TNS.2009.2033694.

[50] O Aktas et al. “60Co gamma radiation effects on DC, RF, and pulsed I–V characteristics of AlGaN/GaN HEMTs”. In: *Solid-State Electronics* 48 (Mar. 2004), pp. 471–475. DOI: 10.1016/j.sse.2003.08.003.

[51] G. A. Umana-Membreno et al. “/sup 60/Co gamma irradiation effects on n-GaN Schottky diodes”. In: *IEEE Transactions on Electron Devices* 50.12 (Dec. 2003), pp. 2326–2334. DOI: 10.1109/TED.2003.820122.

[52] A M. Kurakin et al. “Mechanism of mobility increase of the two-dimensional electron gas in AlGaN/GaN heterostructures under small dose gamma irradiation”. In: *Journal of Applied Physics* 103 (Apr. 2008), pp. 083707–083707. DOI: 10.1063/1.2903144.

[53] S.A. Vitusevich et al. “Improvement of interface properties of AlGaN/GaN heterostructures under gamma-radiation”. In: *Applied Surface Science* 255 (Nov. 2008), pp. 784–786. DOI: 10.1016/j.apsusc.2008.07.029.

[54] C. Sharma et al. “Investigation of the Degradations in Power GaN-on-Si MIS-HEMTs subjected to the cumulative γ-ray Irradiation”. In: *2019 European Symposiym on Reliability of Electron Devices* 221 (2019).

[55] A. N. Tallarico et al. “Investigation of the p-GaN Gate Breakdown in Forward-Biased GaN-Based Power HEMTs”. In: *IEEE Electron Device Letters* 38.1 (Jan. 2017), pp. 99–102. DOI: 10.1109/LED.2016.2631640.

[56] Ning Xu et al. “Gate leakage mechanisms in normally off p-GaN/AlGaN/GaN high electron mobility transistors”. In: *Applied Physics Letters* 113.15 (2018), p. 152104. DOI: 10.1063/1.5041343.

[57] Matteo Meneghini et al. “Trapping phenomena and degradation mechanisms in GaN-based power HEMTs”. In: *Materials Science in Semiconductor Processing* 78 (Oct. 2017). DOI: 10.1016/j.mssp.2017.10.009.

[58] Yuhao Zhang et al. “Threshold voltage control by gate oxide thickness in fluorinated GaN metal-oxide-semiconductor high-electron-mobility transistors”. In: *Applied Physics Letters* 103 (July 2013). DOI: 10.1063/1.4815923.

[59] Wataru Saito et al. “Recessed-Gate Structure Approach Toward Normally Off High-Voltage AlGaN/GaN HEMT for Power Electronics Applications”. In: *Electron Devices, IEEE Transactions on* 53 (Mar. 2006), pp. 356–362. DOI: 10.1109/TED.2005.862708.

[60] E. A. Jones, F. F. Wang, and D. Costinett. “Review of Commercial GaN Power Devices and GaN-Based Converter Design Challenges”. In: *IEEE Journal of Emerging and Selected Topics in Power Electronics* 4.3 (Sept. 2016), pp. 707–719. DOI: 10.1109/JESTPE.2016.2582685.

[61] T. Wu et al. “Analysis of the Gate Capacitance–Voltage Characteristics in p-GaN/AlGaN/GaN Heterostructures”. In: *IEEE Electron Device Letters* 38.12 (Dec. 2017), pp. 1696–1699. DOI: 10.1109/LED.2017.2768099.

[62] S. Stoffels et al. “Failure mode for p-GaN gates under forward gate stress with varying Mg concentration”. In: *2017 IEEE International Reliability Physics Symposium (IRPS)*. Apr. 2017. DOI: 10.1109/IRPS.2017.7936310.

[63] A. Stockman et al. “Gate Conduction Mechanisms and Lifetime Modeling of p-Gate AlGaN/GaN High-Electron-Mobility Transistors”. In: *IEEE Transactions on Electron Devices* 65.12 (Dec. 2018), pp. 5365–5372. DOI: 10.1109/TED.2018.2877262.

[64] B. Bakeroot et al. “Analytical Model for the Threshold Voltage of p -(Al)GaN High-Electron-Mobility Transistors”. In: *IEEE Transactions on Electron Devices* 65.1 (Jan. 2018), pp. 79–86. DOI: 10.1109/TED.2017.2773269.

[65] Y. Tsividis and C. McAndrew. *Operation and Modeling of the MOS Transistor, Third Edtion International Edition*. OUP USA, 2012. ISBN: 9780199829835. URL: https://books.google.com.tw/books?id=fCOAMAEACAAJ.

[66] M. Si M. A. Alam and P. D. Ye. “A critical review of recent progress on negative capacitance field-effect transistors”. In: *Applied Physics Letters* 114.9 (Feb. 2019). DOI: 10.1063/1.5092684.

[67] M. Kobayashi and T. Hiramoto. “On device design for steep-slope negative-capacitance field-effect-transistor operating at sub-0.2V supply voltage with ferroelectric HfO2 thin film”. In: *AIP Advances* 6.2 (Feb. 2016). DOI: 10.1063/1.4942427.

[68] M. Kobayashi et al. “Negative Capacitance for Boosting Tunnel FET performance”. In: *IEEE Transactions on Nanotechnology* 16.2 (Mar. 2017), pp. 253–258. DOI: 10.1109/TNANO.2017.2658688.

[69] Asif Khan et al. “Negative Capacitance in a Ferroelectric Capacitor”. In: *Nature materials* 14 (Sept. 2014). DOI: 10.1038/nmat4148.

[70] Gustau Catalan, David Jiménez, and Alexei Gruverman. “Ferroelectrics: Negative capacitance detected”. In: *Nature materials* 14 (Jan. 2015), pp. 137–9. DOI: 10.1038/nmat4195.

[71] Daniel J. R. Appleby et al. “Experimental Observation of Negative Capacitance in Ferroelectrics at Room Temperature”. In: *Nano Letters* 14.7 (2014), pp. 3864–3868. DOI: 10.1021/nl5017255.

[72] Pavlo Zubko et al. “Negative capacitance in multidomain ferroelectric superlattices”. In: *Nature* 534 (June 2016). DOI: 10.1038/nature17659.

[73] Sayeef Salahuddin and Supriyo Datta. “Use of Negative Capacitance to Provide Voltage Amplification for Low Power Nanoscale Devices”. In: *Nano Letters* 8.2 (2008), pp. 405–410. DOI: 10.1021/nl071804g.

[74] L. D. Landau and I. M. Khalatnikov. “On the anomalous absorption of sound near a second order phase transition point”. In: 96 (1954), pp. 469–472.

[75] U. Schroeder, C.S. Hwang, and H. Funakubo. *Ferroelectricity in Doped Hafnium Oxide: Materials, Properties and Devices*. Woodhead Publishing Series in Electronic and Optical Materials. Elsevier Science, 2019. ISBN: 9780081024317. URL: https://books.google.com.tw/books?id=4xuPDwAAQBAJ.

[76] T. Schenk. *Formation of Ferroelectricity in Hafnium Oxide Based Thin Films*. Books on Demand, 2017. ISBN: 9783743127296. URL: https://books.google.com.tw/books?id=AQheDgAAQBAJ.

[77] A. I. Khan et al. “Negative Capacitance Behavior in a Leaky Ferroelectric”. In: *IEEE Transactions on Electron Devices* 63.11 (Nov. 2016), pp. 4416–4422. DOI: 10.1109/TED.2016.2612656.

[78] A. Aziz et al. “Physics-Based Circuit-Compatible SPICE Model for Ferroelectric Transistors”. In: *IEEE Electron Device Letters* 37.6 (July 2016), pp. 805–808. DOI: 10.1109/LED.2016.2558149.

[79] M.E. Lines and A.M. Glass. *Principles and Applications of Ferroelectrics and Related Materials*. Oxford Classic Texts in the Physical Sciences. OUP Oxford, 2001. ISBN: 9780198507789. URL: https://books.google.com.tw/books?id=p6ruJH8C84kC.

[80] G. Pahwa et al. “Analysis and Compact Modeling of Negative Capacitance Transistor with High ON-Current and Negative Output Differential Resistance—Part I: Model Description”. In: *IEEE Transactions on Electron Devices* 63.12 (Dec. 2016), pp. 4981–4985. DOI: 10.1109/TED.2016.2614432.

[81] H. Amrouch et al. “Negative Capacitance Transistor to Address the Fundamental Limitations in Technology Scaling: Processor Performance”. In: *IEEE Access* 6 (2018), pp. 52754–52765. DOI: 10.1109/ACCESS.2018.2870916.

[82] Ujwal Radhakrishna, Sayeef Salahuddin, and D. A. Antoniadis. “Compact model of Negative Capacitance MOSFETs (NCFETs)”. In: 2017.

[83] G. Pahwa et al. “Compact Model for Ferroelectric Negative Capacitance Transistor With MFIS Structure”. In: *IEEE Transactions on Electron Devices* 64.3 (Mar. 2017), pp. 1366–1374. DOI: 10.1109/TED.2017.2654066.

[84] G. Pahwa et al. “Physical Insights on Negative Capacitance Transistors in Nonhysteresis and Hysteresis Regimes: MFMIS Versus MFIS Structures”. In: *IEEE Transactions on Electron Devices* 65.3 (Mar. 2018), pp. 867–873. DOI: 10.1109/TED.2018.2794499.